

PARAMETRIZING FREEFORM OPTICAL SURFACES FOR THE OPTIMIZED DESIGN OF  
IMAGING AND ILLUMINATION SYSTEMS

by

Kaitlyn Williams

---

Copyright © Kaitlyn Williams 2017

A Thesis Submitted to the Faculty of the

COLLEGE OF OPTICAL SCIENCES

In Partial Fulfillment of the Requirements

For the Degree of

MASTER OF SCIENCE

In the Graduate College

THE UNIVERSITY OF ARIZONA

2017

## STATEMENT BY AUTHOR

The thesis titled *Parametrizing Freeform Optical Surfaces For The Optimized Design Of Imaging And Illumination Systems* prepared by Kaitlyn Williams has been submitted in partial fulfillment of requirements for a master's degree at the University of Arizona and is deposited in the University Library to be made available to borrowers under rules of the Library.

Brief quotations from this thesis are allowable without special permission, provided that an accurate acknowledgement of the source is made. Requests for permission for extended quotation from or reproduction of this manuscript in whole or in part may be granted by the head of the major department or the Dean of the Graduate College when in his or her judgment the proposed use of the material is in the interests of scholarship. In all other instances, however, permission must be obtained from the author.

SIGNED: *Kaitlyn Williams*

## APPROVAL BY THESIS DIRECTOR

This thesis has been approved on the date shown below:

---

*Dr. Richard John Koshel*  
*Associate Dean for Academic Programs*

05/05/2017  
Date

## ACKNOWLEDGEMENTS

I would like to acknowledge Synopsys, Inc. for their LightTools and CODE V educational licenses, two optics software programs that were vital to the completion of this project. And, I would also like to acknowledge MathWorks for its educational license of MATLAB.

Thank you to my friends and family. To my mother, who dealt with 4:00 am novel-like emails detailing my awe of the beauty of Maxwell's Equations. To my father, for always engaging in scientific discussion with me and being a springboard for ideas. To my sister, for always encouraging me and for lovingly enduring my ramblings about cool phenomena in science. And, to my close friends, for their splendid company during late library nights. I love them all so dearly.

To the members of my numerous soccer teams, thank you for always making our games fun and providing the best de-stresser for a stressed-out graduate student.

I want to recognize the faculty, staff, and students at the College of Optical Sciences for being such a warm, welcoming community. And, a huge thank you to the members of my undergraduate cohort for the opportunity to collaborate with such intelligent and kind young minds, and for fostering a fun learning environment that made me fall in love with optics.

I'm grateful to work for Raytheon Missile Systems, for its strong support for their employee's pursuit of higher education. Thank you to my boss, Dr. Eric Fest, for his interest in my work and support of my efforts. And, a very special thank you to my mentor, Justan Forsyth, for enduring my complaints, encouraging me through tough times, and being a fantastic learning resource.

Thank you to Rachel Ulanich, Ross Uthoff, Page King, Liliana Ruiz Diaz, Dr. John Koshel, and Nathan Saxton for being invaluable members of the Illumination Design Group. If it weren't for their efforts and their inspiring creativity, my thesis would be incomplete.

I thank the members of my defense committee, Dr. José Sasián and Dr. Dae Wook Kim, for their involvement in this topic and their willingness to help.

I would especially like to thank the individuals and organizations that made it possible for me to pursue this degree: Thank you, Dr. John Koshel, for believing in me and encouraging me to take the next step in my education, and for his unwavering support with advising my thesis. Many thanks to SPIE and Photonics Media for their contribution to the Teddi Laurin Scholarship. And, lastly, I'm incredibly grateful for the amazing opportunity given to me by the Boye Family Foundation. I am honored to be a part of the wonderful community that is the world of optics.

Finally, thank you to the University of Arizona. I am a proud Wildcat for Life. Bear down!

# TABLE OF CONTENTS

<b>LIST OF FIGURES .....</b>	<b>6</b>
<b>LIST OF TABLES .....</b>	<b>10</b>
<b>ABSTRACT .....</b>	<b>11</b>
<b>1. Introduction.....</b>	<b>12</b>
<b>2. Imaging Design Scenario.....</b>	<b>14</b>
<b>2.1. Defining Freeformity for Refractive Imaging Systems.....</b>	<b>14</b>
<b>2.2. Functional Fitting of Imaging Freeforms .....</b>	<b>17</b>
2.2.1. Zernike Polynomials.....	18
2.2.2. XY Polynomials .....	19
<b>2.3. Imaging with Refractive Freeform Surfaces .....</b>	<b>20</b>
2.3.1. System Initialization Parameters .....	21
2.3.2. Test Parameters .....	23
2.3.3. Optimization Approach .....	25
2.3.4. Results Using a Scaled Focus Height Approach .....	27
2.3.5. Results Using the General Freeformity Definition.....	36
<b>2.4. Conclusions.....</b>	<b>39</b>
<b>3. Illumination Design Scenario.....</b>	<b>40</b>
<b>3.1. Case Study Description.....</b>	<b>40</b>
<b>3.2. Generating Illumination Freeform Optics.....</b>	<b>41</b>
<b>3.3. Functional Fitting of Illumination Freeform Surfaces .....</b>	<b>44</b>
3.3.1. Zernike Polynomials.....	45
3.3.2. Legendre Polynomials .....	51
3.3.3. Leveraging Symmetry to Improve Computational Efficiency .....	53
<b>3.4. Illumination with Refractive Freeforms .....</b>	<b>54</b>
3.4.1. Functional Fitting Results.....	56
<b>3.5. Illumination with Reflective Freeforms .....</b>	<b>64</b>
3.5.1. Defining Reflective Illumination Design Constraints .....	64

3.5.2.	A Reflective Illumination System Optimized with a Reverse-Oriented Isotropic Source .....	67
3.5.3.	A Reflective Illumination System Optimized with a Forward-Oriented Isotropic Source.....	72
3.6.	<b>Conclusions.....</b>	<b>76</b>
<b>4.</b>	<b>Summary.....</b>	<b>78</b>
	<b>References .....</b>	<b>79</b>
<b>5.</b>	<b>Appendix.....</b>	<b>81</b>
5.1.	<b>Refractive Imaging.....</b>	<b>81</b>
5.2.	<b>Refractive Illumination .....</b>	<b>85</b>
5.3.	<b>Reflective Illumination, Reverse-Oriented Source .....</b>	<b>88</b>
5.3.1.	Ray-Trace Results .....	88
5.3.2.	Functional Fitting Results.....	90
5.4.	<b>Reflective Illumination, Forward-Oriented Source.....</b>	<b>91</b>
5.4.1.	Ray-Trace Results .....	91
5.4.2.	Functional Fitting Results.....	93

# LIST OF FIGURES

Figure 2.1-1—Preliminary drawing depicting the freeformity parameters of an imaging system	15
Figure 2.1-2—Demonstrating the upper and lower marginal ray projected distances on the tilted freeform plane ( $d_{upper} > d_{lower}$ ).....	16
Figure 2.3-1—System configuration for refractive imaging freeform .....	20
Figure 2.3-2—Lens prescription for on-axis configuration, 10-mm diameter entrance pupil.....	21
Figure 2.3-3—Lens layout for on-axis configuration, 25-mm diameter entrance pupil.....	21
Figure 2.3-4—Procedure for optimizing the freeform surface tilt.....	26
Figure 2.3-5—Procedure for optimizing XY polynomials for coefficients 1 through 65 and Zernike polynomials for coefficients 2 through 66 .....	26
Figure 2.3-6—Lens layout for a single on-axis object with a 25-mm entrance pupil diameter and an focus height of 50 mm (the maximum for the 25-mm EPD) .....	28
Figure 2.3-7—Number of Zernike and XY coefficients required for imaging convergence on a diffraction-limited RMS image size as a function of normalized focus height .....	29
Figure 2.3-8—Examining the effect that adding polynomial orders has on the scaled RMS image size (when normalized to the Airy disk diameter, any value $<1$ is diffraction-limited) .....	30
Figure 2.3-9—Freeform lens with a 25-mm EPD, a 25-mm focus height from the on-axis object, and with the largest object field angle of $1^\circ$ .....	31
Figure 2.3-10—Minimized scaled image size as a function of normalized focus height for the system with a field of view, arranged vertically by increasing FOV (any value $<1$ is diffraction-limited).....	32
Figure 2.3-11—Term that converges on minimized image size as a function of normalized focus height, for the system with a field of view and arranged vertically by increasing FOV .....	33
Figure 2.3-12—MTF at 0.25 of the spatial cutoff frequency as a function of the normalized focus height, for the system with a field of view and arranged vertically by increasing FOV .....	34
Figure 2.3-13—MTF amplitude at 10 line pairs per mm as a function of the normalized focus height, for the system with a field of view and arranged vertically by increasing FOV .....	35
Figure 2.3-14—Image size as a function of freeformity, arranged by increasing field of view...	36

Figure 2.3-15—MTF for 0.25 of the spatial cutoff frequency as a function of freeformity, for the system with a field of view and arranged vertically by increasing FOV .....	38
Figure 3.1-1— <i>Green on Blue</i> on display at the University of Arizona Museum of Art .....	40
Figure 3.2-1—Anticipated design configuration for the illumination freeform .....	42
Figure 3.4-1—Refractive illumination freeform with the source at a $-50^\circ$ Y-tilt and a $70^\circ$ collection cone angle .....	55
Figure 3.4-2—Target illumination map for a refractive freeform with a $-57.5^\circ$ source Y-tilt and $94.9^\circ$ emission cone ( $70^\circ$ cone collected by the freeform). 2 billion rays were traced. ....	56
Figure 3.4-3— <i>X</i> and <i>Y</i> symmetry properties of the refractive freeform .....	56
Figure 3.4-4—Fit behavior of the freeform for a $57.5^\circ$ source Y-tilt and $70^\circ$ cone angle accepted by the freeform.....	57
Figure 3.4-5—RMS error trends, highlighting the effect of adding new polynomial orders .....	58
Figure 3.4-6—PV error trends when new polynomial orders are introduced.....	59
Figure 3.4-7—Demonstrating the effect that source emission cone angle has on the fit error of the refractive illumination freeforms (RMS, PV error results from a fit using 100 terms) .....	60
Figure 3.4-8—Examining the refractive illumination freeform RMS error as a function of the source point angle for the inclusion of different polynomial orders.....	61
Figure 3.4-9—Examining the refractive illumination freeform PV error as a function of the source point angle for different coefficient amounts.....	62
Figure 3.4-10—Freeform for source with $-60^\circ$ y-tilt and $70^\circ$ cone (best Legendre RMS).....	63
Figure 3.4-11—Freeform for source with $-67.5^\circ$ y-tilt and $70^\circ$ cone (best Legendre RMS).....	63
Figure 3.4-12—Freeform for source with $-80^\circ$ y-tilt and $70^\circ$ cone (best Legendre RMS).....	63
Figure 3.5-1—Reflective illumination freeform with a reverse-oriented source, $185^\circ$ Y-tilt.....	66
Figure 3.5-2—Reflective illumination freeform with a forward-oriented source, $42.5^\circ$ Y-tilt ....	66
Figure 3.5-3—Target illuminance map for a reflective freeform optic with a $185^\circ$ Y-tilted source and a $100^\circ$ emission cone angle. There were 2 billion rays traced. ....	67
Figure 3.5-4—RMS error trends, highlighting the effect of adding new polynomial orders .....	68
Figure 3.5-5—PV error trends when new polynomial orders are introduced.....	68
Figure 3.5-6—RMS error convergence trends as a function of source pointing angle for the reverse-oriented reflective illumination freeform optics .....	70

Figure 3.5-7—PV error convergence trends as a function of source pointing angle for the reverse-oriented reflective illumination freeform optics .....	70
Figure 3.5-8—Point cloud for reflective freeform with 180° y-tilt and 100° cone .....	71
Figure 3.5-9—Point cloud for reflective freeform with 187.5° y-tilt and 100° cone .....	71
Figure 3.5-10—Point cloud for reflective freeform with 195° y-tilt and 100° cone .....	71
Figure 3.5-11—Target illuminance map for a reflective illumination freeform optic with a 42.5° Y-tilted source and a 120° emission cone angle .....	72
Figure 3.5-12—Fit convergence trends as a function of source emission cone angle for the forward-oriented reflective illumination freeform optics .....	73
Figure 3.5-13—RMS error convergence trends as a function of source pointing angle for the forward-oriented reflective illumination freeform optics .....	73
Figure 3.5-14—PV error convergence trends as a function of source pointing angle for the forward-oriented reflective illumination freeform optics .....	74
Figure 3.5-15—Point cloud for reflective freeform with 37.5° y-tilt and 90° cone .....	74
Figure 3.5-16—Point cloud for reflective freeform with 50° y-tilt and 90° cone .....	75
Figure 3.5-17—Point cloud for reflective freeform with 60° y-tilt and 90° cone .....	75
Figure 3.6-1—Number of terms required to converge on sub-5 $\mu\text{m}$ RMS error.....	76
Figure 3.6-2—Number of terms required to converge on sub-1 $\mu\text{m}$ RMS error.....	76
Figure 3.6-3—Number of terms required to converge on sub-5 $\mu\text{m}$ RMS error for the illumination freeform surfaces, representing only the used coefficients (due to the removal of all odd- $x$ coefficients).....	77
Figure 3.6-4—Number of terms required to converge on sub-1 $\mu\text{m}$ RMS error for the illumination freeform surfaces, representing only the used coefficients (due to the removal of all odd- $x$ coefficients).....	77
Figure 5.1-1—Term that converges on maximum MTF for 0.25 of the spatial cutoff frequency as a function of normalized focus height, for the system with a field of view and arranged vertically by increasing FOV .....	81
Figure 5.1-2— Term that converges on maximum MTF amplitude at 10 line pairs per mm, for the system with a field of view and arranged vertically by increasing FOV .....	82
Figure 5.1-3— Term that converges on minimum image size as a function of freeformity, for the system with a field of view and arranged vertically by increasing FOV .....	83

Figure 5.1-4—Term that converges on maximum MTF amplitude for 0.25 of the spatial cutoff frequency as a function of freeformity, for the system with a field of view and arranged vertically by increasing FOV .....	84
Figure 5.2-1—Illumination characteristics for the refractive freeform optics.....	85
Figure 5.2-2—Effective illumination levels of the target for the refractive freeform optics .....	86
Figure 5.2-3—Normalized illumination efficiency for the refractive freeform optics.....	87
Figure 5.3-1—Illumination characteristics, reflective freeform, reverse-oriented source.....	88
Figure 5.3-2—Effective target illuminance, reflective freeform, reverse-oriented source.....	88
Figure 5.3-3—Normalized illumination efficiency for the reflective freeform with the reverse-oriented source .....	89
Figure 5.3-4—Fit behavior of the 185° (reverse-oriented) source Y-tilt, 100° emission cone .....	90
Figure 5.4-1—Illumination characteristics, reflective freeform, forward-oriented source .....	91
Figure 5.4-2—Effective target illuminance, reflective freeform, forward-oriented source .....	91
Figure 5.4-3—Normalized illumination efficiency for the reflective freeform with the forward-oriented source .....	92
Figure 5.4-4—Fit behavior of the 42.5° (forward-oriented) source Y-tilt, 120° emission cone ...	93
Figure 5.4-5—Legendre fit trends for varying point angle.....	94
Figure 5.4-6—Zernike fit trends for varying point angle .....	95

# LIST OF TABLES

Table 2-1—First term of each two-dimensional polynomial order for XY and Zernike.....	17
Table 2-2—Refractive imaging system requirements .....	22
Table 2-3—Test parameters for on-axis refractive imaging.....	23
Table 2-4—Test parameters for freeform refractive imaging with a field of view .....	24
Table 2-5—Freeform initializations, used as variables for optimizing surface tilt .....	25
Table 2-6—Number of coefficients needed for refractive imaging convergence .....	29
Table 3-1—Cartesian symmetry of first 16 Zernike polynomials [12] .....	50
Table 3-2—Cartesian symmetry of first 10 Legendre polynomials [12].....	52
Table 3-3—Design constraints for refractive illumination scenario.....	54
Table 3-4—Effect of including Cartesian oval in the refractive illumination design.....	54
Table 3-5—Specifics of refractive illumination varied parameters.....	55
Table 3-6—Terms that significantly reduce the RMS error in the computed fit surface .....	58
Table 3-7—Design constraints for reflective illumination scenario.....	65
Table 3-8—Specifics of reflective illumination varied parameters .....	65
Table 3-9—Terms that significantly reduce the RMS error in the computed fit surface .....	69

# ABSTRACT

Two optical design scenarios—imaging and illumination—were investigated for their use of Cartesian- and polar-based functions to generate freeform optical surfaces.

The imaging scenario investigated a single-element, refracting freeform surface that converts an on-axis object field to an off-axis image point. XY polynomials (Cartesian but not orthogonal) and Zernike polynomials (Polar and orthogonal) were the two different function sets used to manipulate the surfaces to achieve the freeform imaging scenarios. The investigation discovered that the results between both function sets did not differ enough to single out a more effective surface type. However, the results did indicate that the Zernike function set typically required fewer coefficients to converge on an optimal imaging solution.

The illumination scenario utilized an architectural lighting situation surrounding the Rothko exhibit for *Green on Blue* at the University of Arizona Museum of Art. The source location was fixed to the light track in the exhibit space and pointed in many different orientations towards the painting. For each orientation, a point cloud of a freeform optical surface was generated such that the painting surface was illuminated with uniform and low-level light. For each of these generated point clouds, a Legendre (Cartesian and orthogonal) and a Zernike (polar and orthogonal) fitting function was applied, and the convergence results were compared. In general, it was found that, after the 20th included fit term, the Legendre function resulted in a smaller RMS fit error than the Zernike function. However, if the light source was pointed near the center of the painting, the Zernike function converged on a solution with fewer fit terms than Legendre.

Amidst the imaging scenario, a definition for the extent to which a surface was freeform, or the “freeformity”, was given. This definition proved to be an effective solution when the image size was compared for an F/3.33, F/4, F/5, and F/6.67 system for a range of different image focusing heights: the image size trends for each F-number overlapped, indicating a universal freeform term.

In addition, a recursive formula for Cartesian Zernike polynomials was defined, which was used to generate an infinite number of Zernike terms using one single recursive expression.

# 1. Introduction

It is strategic for an optical engineer to understand the mathematical representation of optical surfaces. The two-dimensional, axially symmetric function for a conic surface is a widely-used definition for such surfaces, provided in Equation (1-1) and (1-2) [11].

Radially-defined:

$$z_{conic}(\rho) = \frac{\rho^2}{R + \sqrt{R^2 - (1 + \kappa)\rho^2}} \quad (1-1)$$

Cartesian-defined:

$$z_{conic}(x, y) = \frac{x^2 + y^2}{R + \sqrt{R^2 - (1 + \kappa)(x^2 + y^2)}} \quad (1-2)$$

$$\kappa = -e^2$$

$e$  = surface eccentricity

$R$  = surface radius of curvature

$\rho = \sqrt{x^2 + y^2}$  = normalized radial distance lateral from the optical axis

$z$  = surface height in the direction of the optical axis

These equations can be used to define a wide variety of optical surfaces, from reflectors to refractors alike. However, they cannot represent freeform surfaces, which are defined by being deviated from axial or line symmetry [13]. For these surfaces, a function that can introduce asymmetry must be used.

In optics, a commonly used parametrization function is one defined by Frits Zernike [26]. It involves two-dimensional orthogonal polynomials defined in polar coordinates that are separable in radial and azimuthal component, where the azimuthal component allows for the function to become rotationally asymmetric.

Other available functions include those defined in Cartesian coordinates, such as Legendre, XY, Bernstein, or Chebyshev polynomials.

To properly approach the parametrization of freeform surfaces with the previously mentioned functions, it is beneficial to understand the number of polynomials required to provide an accurate representation of the original surface. The following discussion will explore this, and will also delve into understanding the extent to which more asymmetric freeforms will change the number of polynomials required for parametrizing.

Freeform surfaces were generated for imaging and illumination scenarios. The imaging freeform generation involved adding polynomials to an initial conic surface, while the illumination freeform surfaces were defined exclusively by the aforementioned polynomial functions.

## **2. Imaging Design Scenario**

When applied to imaging scenarios, freeform surfaces map object rays to an image that differs from what would be produced by a traditional axially symmetric optical system.

This analysis was done for a refractive imaging system, but it could also be explored with reflective freeform surfaces [15]. Reflective imaging systems do not encounter the dispersion effects that refractive imaging systems do. But, the freeform generation follows the same principles.

The optical design software, CODE V 11.0 from Synopsys, Inc. was used to optimize the freeform system to generate freeform scenarios.

### **2.1. Defining Freeformity for Refractive Imaging Systems**

Lens design is governed by two rays: the marginal ray and the chief ray. There exists an infinite number of each of these rays, as they are defined by any ray that passes through the margin of the stop aperture and any ray that passes from the center of the stop to the maximum field of view image. Due to axial symmetry, traditional lens design only traces one of each ray.

However, freeform systems no longer have that axial symmetry, which requires the selection of new marginal and chief rays.

In the following discussion, the tilted optical axis ray is referred to as the image ray and the original optical axis is referred to as the parent optical axis. For the functionality of the given equations, the image ray slope must be positive. See Figure 2.1-1 for a schematic describing the important parameters that drive the following discussion.

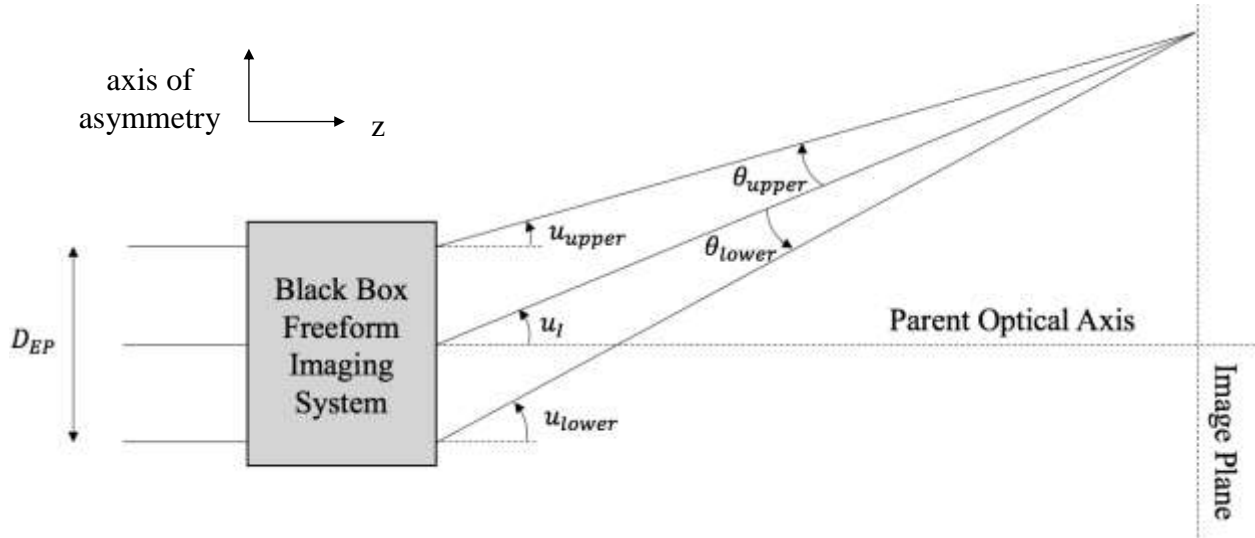


**Figure 2.1-1—Preliminary drawing depicting the freeformity parameters of an imaging system**

$u_I$  = image ray slope

$u_{upper}$  = upper marginal ray slope

$u_{lower}$  = lower marginal ray slope

For freeform optics, the two marginal rays differ because of the introduced asymmetry. One way to quantify this introduced asymmetry is to define the difference between the two rays. This can be done by defining the angular separation from the image ray to each marginal ray, as seen in Equations (2-1) and (2-2).

$$\theta_{upper} = \tan^{-1}(u_I) - \tan^{-1}(u_{upper}) \quad (2-1)$$

$$\theta_{lower} = \tan^{-1}(u_{lower}) - \tan^{-1}(u_I) \quad (2-2)$$

An expression for the asymmetry cannot simply be determined by taking the ratio between the two angular separations because they both exist in angular space. Thus, another metric must be explored.

These angular extents can be extended back to the freeform surface to form a tilted “freeform plane” that intersects the parent optical axis and the freeform surface aperture. See Figure 2.1-2.

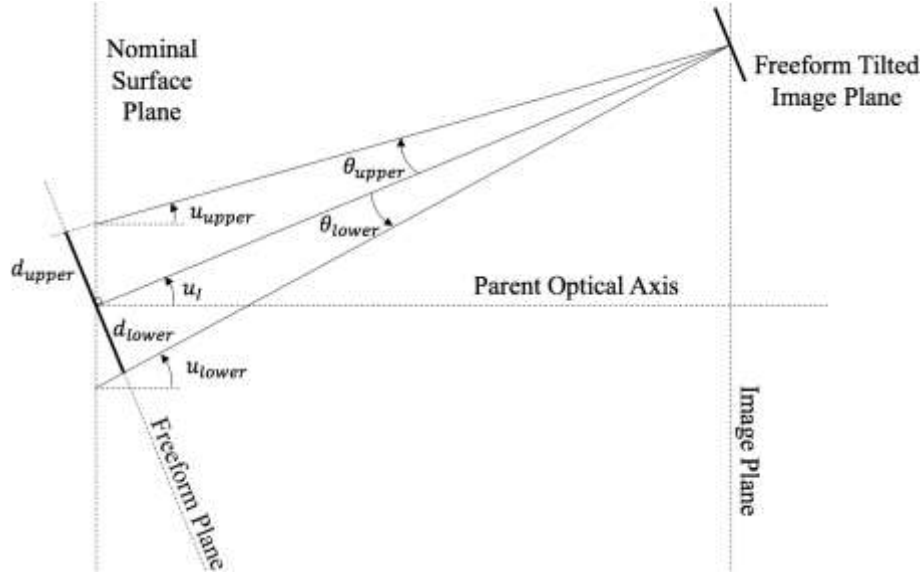


**Figure 2.1-2—Demonstrating the upper and lower marginal ray projected distances on the tilted freeform plane ( $d_{upper} > d_{lower}$ )**

This plane allows for a distance magnitude-based ratio to define the asymmetry, which results in a variation of the desired angular ratios. See Equations (2-3) through (2-5).

$$d_{upper} = \bar{R} \tan(\theta_{upper}) \quad (2-3)$$

$$d_{lower} = \bar{R} \tan(\theta_{lower}) \quad (2-4)$$

$\bar{R}$  = distance from freeform aperture center to the image point

$$F = \frac{d_{upper}}{d_{lower}} = \frac{\bar{R} \tan(\theta_{upper})}{\bar{R} \tan(\theta_{lower})} = \frac{\tan(\theta_{upper})}{\tan(\theta_{lower})} \quad (2-5)$$

With Equation (2-5), an initial freeformity parameter is defined. However, it is imaging to a tilted plane at the image plane. To correct this, Lambert's cosine law is applied, seen in Equation (2-6).

$$F_{imaging} = F \cdot \cos(\tan^{-1}(u_l)) \quad (2-6)$$

If a system is axially symmetric and focuses to an on-axis image, the freeformity is 1. As the image is moved further off-axis, the freeformity becomes greater than 1.

## 2.2. Functional Fitting of Imaging Freeforms

The options for fitting and making freeform imaging surfaces are confined to what is available in CODE V. Starting with a baseline definition of a conic surface, which has axial symmetry about the optical axis, extra polynomial coefficients must be added on top of this surface to allow for the optimization to mitigate off-axis aberration effects.

Of all the provided surface types in CODE V, Zernike and XY polynomials were selected such that a polar and a Cartesian basis space would be represented in the analysis. CODE V provides a maximum of 66 Zernike and 65 XY polynomial coefficients.

**Table 2-1—First term of each two-dimensional polynomial order for XY and Zernike**

2-D Polynomial Order	XY	Zernike
0	none	1
1	1	2
2	3	4
3	6	7
4	10	11
5	15	16
6	21	22
7	28	29
8	36	37
9	45	46
10	55	56

The Zernike surface requires a normalization radius to maintain orthonormality, while the XY polynomial function can be optimized without it because its polynomials are not orthogonal.

### 2.2.1. Zernike Polynomials

The definition for the Zernike polynomials is given in Equation (2-7) and (2-8) [26].

$$Z_n^m(\rho, \varphi) = R_n^m(\rho) \cos(m\varphi) \quad (2-7)$$

$$Z_n^{-m}(\rho, \varphi) = R_n^m(\rho) \sin(m\varphi) \quad (2-8)$$

$\rho$  = normalized aperture radius, transverse from optical axis

$\varphi$  = azimuthal angle, where  $\varphi = 0^\circ$  is along the  $x$ -axis

$R_n^m(\rho)$  = Zernike radial polynomials

The Zernike radial polynomials,  $R_n^m(\rho)$ , are expressed in Equation (2-9) [26].

$$R_n^m(\rho) = \sum_{k=0}^{n-m} \frac{(-1)^k (2n-m-k)!}{k! (n-k)! (n-m-k)!} \rho^{2(n-k)-m} \quad (2-9)$$

CODE V defines Zernike polynomial surfaces with Equation (2-10), which is a combination of Equation (1-1) and the Zernike polynomials defined above.

$$f_{\text{Zernike}}(a_j; \rho, \varphi) = z_{\text{conic}}(\rho) + \left[ \sum_{n=0}^{10} \sum_{k=0}^n a_{n,2k-n} Z_n^{2k-n}(\rho, \varphi) \right] \quad (2-10)$$

$a$  = Zernike coefficient

### 2.2.2. XY Polynomials

CODE V defines XY polynomial surfaces with Equation (2-11), which involves Equation (1-2). The complete XY polynomial surface type is defined by Equation (2-12).

$$f_{XY}(a_{m,n}; x, y) = z_{conic}(x, y) + \sum_{j=2}^{66} a_j x^m y^n \quad (2-11)$$

$$j = \frac{(m+n)^2 + m + 3n}{2} + 1 \quad (2-12)$$

$$a_j = j^{th} \text{ XY coefficient}$$

## 2.3. Imaging with Refractive Freeform Surfaces

Freeform surfaces can be used with refractive imaging to focus on-axis collimated object rays to an off-axis image point (see Figure 2.3-1).

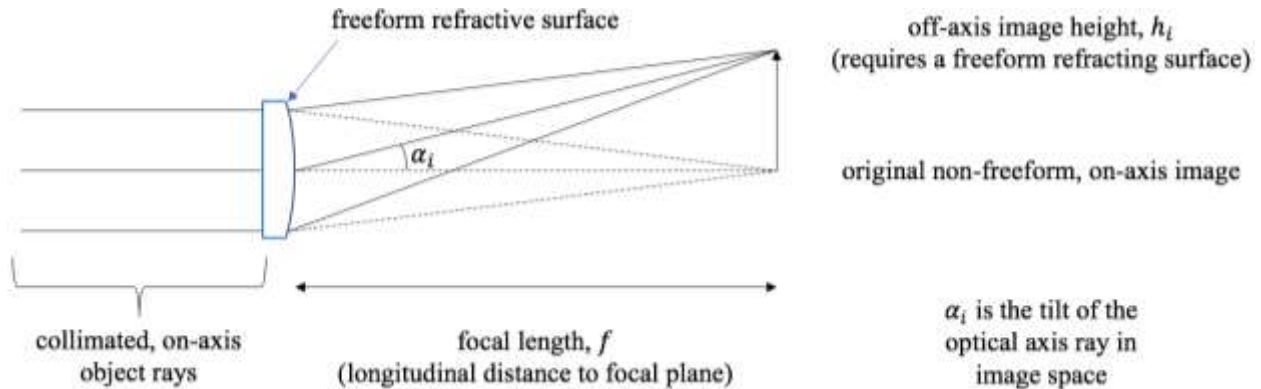


**Figure 2.3-1—System configuration for refractive imaging freeform**

To approach this concept, the freeform system was initialized with parameters that define a traditional, axially-symmetric optical system, called parent parameters. Then, it was optimized such that the same longitudinal focal distance was maintained while forcing the rays to focus at the desired transverse focus height at a point off-axis. The process of forcing the rays off axis involved adding tilt to the surface and deviating from a typical aspheric surface definition.

For insight into which basis space, polar or Cartesian, better-modeled freeform refractive imaging systems, two optimizations were performed on this system. One added Zernike polynomials to the baseline conic surface (defined in polar coordinates) while the other added XY polynomials (defined in Cartesian coordinates). Refer to Section 2.2 for their mathematical descriptions.

### 2.3.1. System Initialization Parameters

The axially-symmetric optical system used for this case study was a 100-mm focal length BK7 plano-convex positive lens with a conic convex surface. The lens was designed for a wavelength of 587.6 nm and had its aperture stop at the planar surface.

Given these specifications, the radius of curvature of the second surface was -51.68 mm [5]. And, the eccentricity of the conic was selected such that it was equivalent to the refractive index preceding the surface, which produced a conic constant of -2.33 [6].

The lens prescription and lens layout for the parameters defined above is shown in Figure 2.3-2 and Figure 2.3-3, respectively.

Surface #	Surface Name	Surface Type	Y Radius	Thickness	Glass	Refract Mode	Y Semi-Aperture	Non-Centered Data
Object		Sphere	Infinity	Infinity		Refract		
Stop		Sphere	Infinity	15.0000	BK7_SCH	Refract	5.0000	
2		XY Polyn	-51.6800	100.0000		Refract	5.0000	Reverse Decenter
Image		Sphere	Infinity	0.0000		Refract	0.0007	Decenter & Return
End of Data								

Figure 2.3-2—Lens prescription for on-axis configuration, 10-mm diameter entrance pupil

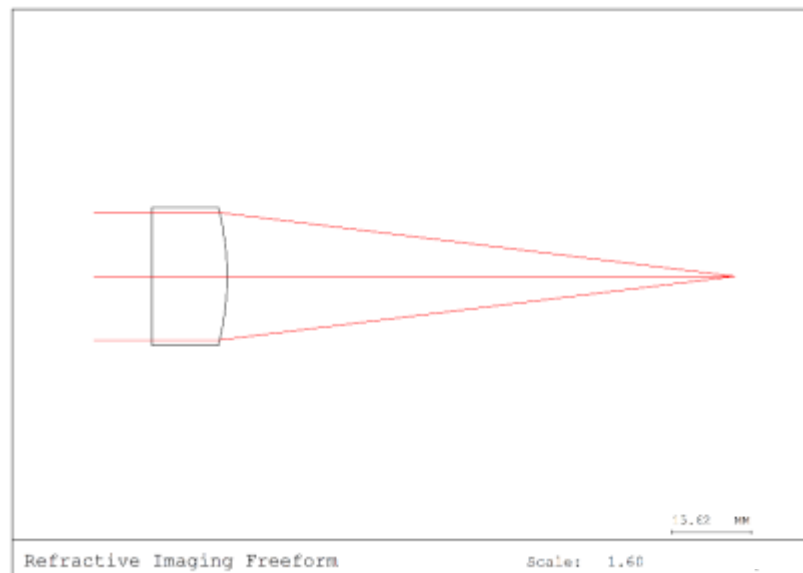


Figure 2.3-3—Lens layout for on-axis configuration, 25-mm diameter entrance pupil

Since the first surface of the lens was planar, the element thickness did not impact the effective focal length. It did, however, constrain the amount of tilt that could be introduced to the freeform surface. If the lens is too thin and the tilt is too large, a negative edge thickness could result, effectively creating an unrealistic manufacturing scenario. Therefore, a lens thickness of 15 mm was selected, which allowed for a possible 50° tilt if the entrance pupil diameter was the maximum of 25 mm.

The requirements used to confine the parameters for each generated imaging system are given in Table 2-2.

**Table 2-2—Refractive imaging system requirements**

Design Wavelength	587.6 nm
Lens Element Material	N-BK7
Lens Element Thickness	15 mm
Longitudinal Distance to Focal Plane (NOTE—This is not the system focal length, which changes as the optical axis ray tilts. This is the axial back focal distance.)	100 mm
Object Distance	Infinity
Maximum Allowed Y-Tilt of the Freeform Surface	$-50^\circ < \alpha_s < 50^\circ$
Minimum Allowed Conic Constant of the Freeform Surface	$> -10$
<i>Entrance Pupil Diameter</i>	<i>Varied, description provided in Table 2-3</i>
<i>Object Field Angle</i>	
<i>Focus Height (Global Y Coordinate in the Image Plane)</i>	

## 2.3.2. Test Parameters

The focus height drives the asymmetry, which increases the freeformity. To maintain similar freeformity results for systems with different F-numbers, the maximum focus height was selected to be dependent upon the entrance pupil size.

The performed tests assessed the effect that the parent F-number and focus height have on the image quality for both polynomial surface types of the element specified in Section 2.3.1.

### 2.3.2.1. On-Axis Object Field

Table 2-3 describes the specific test parameters for a system with one on-axis object field.

**Table 2-3—Test parameters for on-axis refractive imaging**

Parameter	Minimum Value	Increment	Maximum Value
Entrance Pupil Diameter	10 <i>mm</i>	5 <i>mm</i>	30 <i>mm</i>
Focus Height	0	1 <i>mm</i>	$2D_{EP}$

The maximum focus height was twice the entrance pupil diameter to select an extreme off-axis case. With this pre-allocation, the focus height was normalized to the radius of the entrance pupil to compare the image quality results to the normalized focus heights for the different F-numbers.

### 2.3.2.2. System with a Field of View

The system was also tested for its ability to converge on solutions that have multiple object field angles, which results in a field of view. It must be specified that this nomenclature for field of view is not the same as the axially-symmetric-defined field of view. Rather, it refers to the maximum object angle deviation from the on-axis object field, or, in other words, the maximum object field angle.

For this scenario, there were three traced object fields: the on-axis field, a field at the full extent, and a field angle that was 70% of the field of view angle.

Object field details and other important parameters for this test case can be seen in Table 2-4.

**Table 2-4—Test parameters for freeform refractive imaging with a field of view**

Parameter	Minimum Value	Increment	Maximum Value
Entrance Pupil Diameter	15 <i>mm</i>	5 <i>mm</i>	30 <i>mm</i>
Object Ray at Full Extent	1°	1°	4°
Object Ray at 70% Extent	0.7°	0.7°	2.8°
Focus Height	0	1 <i>mm</i>	$D_{EP}$

A focus height of the entrance pupil diameter was selected to force the rays to extend beyond the height of the entrance pupil radius. This maximum value was indeed smaller than that of the on-axis object field case, which was due to this imaging scenario's severe degradation in performance when attempting to converge on solutions beyond  $D_{EP}$ .

### 2.3.3. Optimization Approach

To understand the abilities that Zernike and XY polynomials have with creating freeform lenses, the behavior of certain coefficients must be understood. The approach discussed in this section involves incrementally adding coefficients as optimization variables when computing the freeform surface, effectively producing image quality data as a function of coefficients added.

Ultimately, this analysis aims to contribute to a rule of thumb suggesting the minimum number of coefficients required of each surface type to design a diffraction-limited freeform imaging system for various imaging scenarios.

The optimization variables are listed in Table 2-5.

**Table 2-5—Freeform initializations, used as variables for optimizing surface tilt**

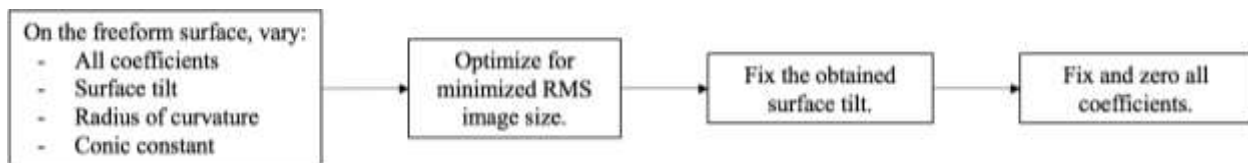
Parameter	Initial Value
Radius of Curvature	-51.68 <i>mm</i>
Conic Constant	-2.33
Surface Y-Tilt	0°
All Polynomial Coefficients	0

When performing a design for a specific test parameter, the CODE V automatic design tool was allowed to cycle up to 25 times until it reached its “converged solution”.

For the design that consisted of only the on-axis object field, the automatic design tool was run once. If the system consisted of multiple object field angles, the automatic design tool was run three times to ensure a converged and representative solution.

Convergence is based upon changing input variables to “improve [system] performance according to a ray-based error function while controlling [the optimization] process according to user-specific constraints” [17]. The user-specific constraints were defined by the requirements provided in Table 2-2.

To enforce consistency in the tilt of the freeform surface with each imaging scenario, the design was split into two steps. The first step is illustrated in Figure 2.3-4. It calculated the optimal tilt for the given imaging scenario by running an optimization with every polynomial coefficient varied. This tilt was likely not the optimal tilt for the given scenario, but it provided a sufficient initialization, which was more stably corrected with the  $y$  polynomial term that are available in both the Zernike and the XY polynomial surface types.



NOTE—See Table 2-5 for the variable initializations.

**Figure 2.3-4—Procedure for optimizing the freeform surface tilt**

With a stable tilt appropriated, the second design step is articulated in Figure 2.3-5, which demonstrate how the Zernike and XY polynomials were optimized, respectively.

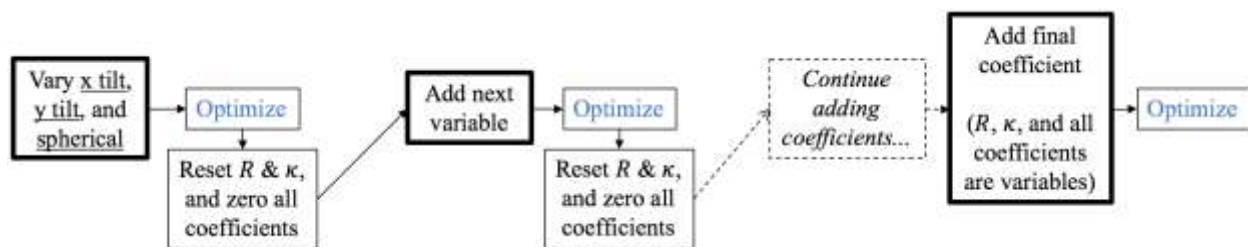


**Figure 2.3-5—Procedure for optimizing XY polynomials for coefficients 1 through 65 and Zernike polynomials for coefficients 2 through 66**

For both XY and Zernike polynomials, the normalization radius was set as the entrance pupil aperture radius.

One design process produced the image quality metrics for all generated freeforms, including the optimizations that used as little as three coefficients to as many as all 65 coefficients. This exact design process was then repeated for each of the test parameters discussed in Section 2.3.2.

#### 2.3.4. Results Using a Scaled Focus Height Approach

The image quality metrics assessed in this section consist of the RMS spot size, the modulation transfer function (MTF) amplitude at 25% of the spatial cutoff frequency, and the MTF amplitude at 10 line pairs per mm. The RMS spot size, referred to as image size in this section, indicates the ability for the design to converge on a solution. The MTF amplitudes indicate the image sharpness.

The spatial cutoff frequency used to represent MTF results was computed for each parent F-number with Equation (2-13) [4].

$$\xi_c = \frac{1}{\lambda(F/\#)} \quad (2-13)$$

The diffraction limited image size was computed with the Rayleigh criterion, giving the Airy disk diameter, seen in Equation (2-14) [5].

$$D_{Airy} = 2.44\lambda(F/\#) \quad (2-14)$$

Before delving into the results using freeformity, the refractive imaging scenario was assessed for the results as a function of the focus height normalized to the entrance pupil aperture radius, according to Equation (2-15).

$$H_{scaled} = \frac{2h_i}{D_{EP}} \quad (2-15)$$

This allows for systems with different parent F-numbers to be compared equivalently because each test scenario designs for a maximum focus height dependent on the entrance pupil aperture radius.

### 2.3.4.1. On-Axis Object Field

The lens layout for one of the most extreme on-axis object scenarios can be seen in Figure 2.3-6.

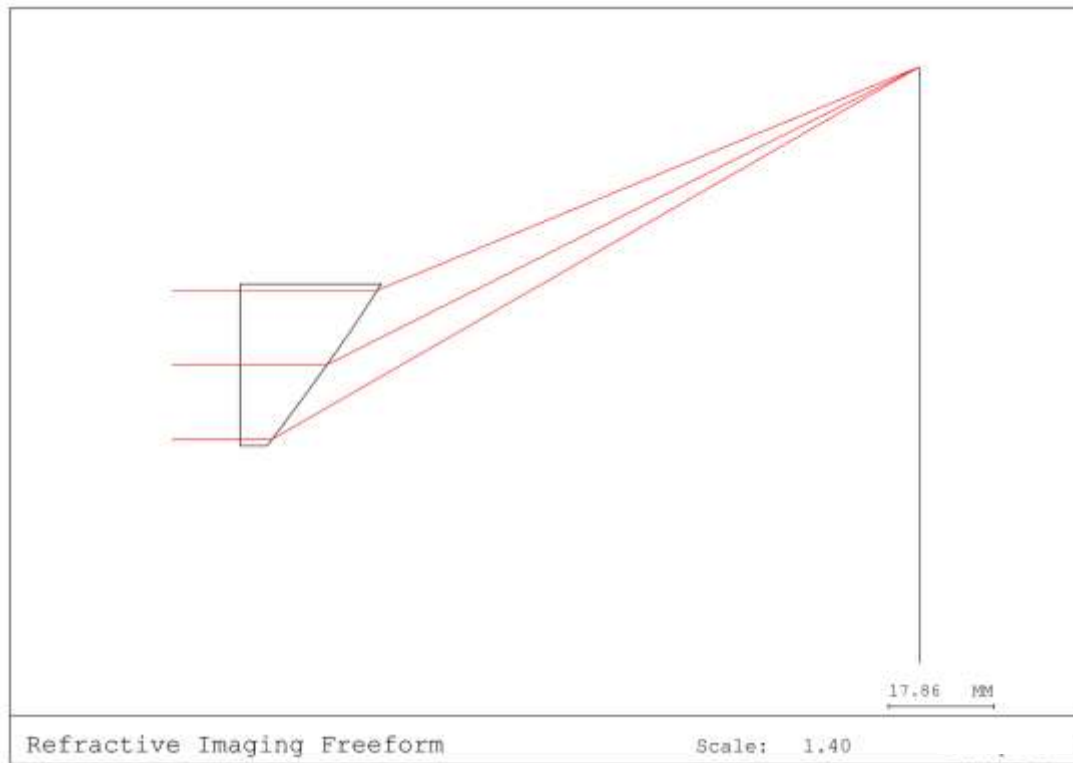


**Figure 2.3-6—Lens layout for a single on-axis object with a 25-mm entrance pupil diameter and an focus height of 50 mm (the maximum for the 25-mm EPD)**

Figure 2.1-1 demonstrates the number of terms that it took for each polynomial type in this analysis to converge on a diffraction-limited image size. In general, the results between XY and Zernike polynomials were similar with regard to the number of coefficients required. The fitting functions utilized similar polynomials for the first few polynomial orders, which likely contributed to these similarities.

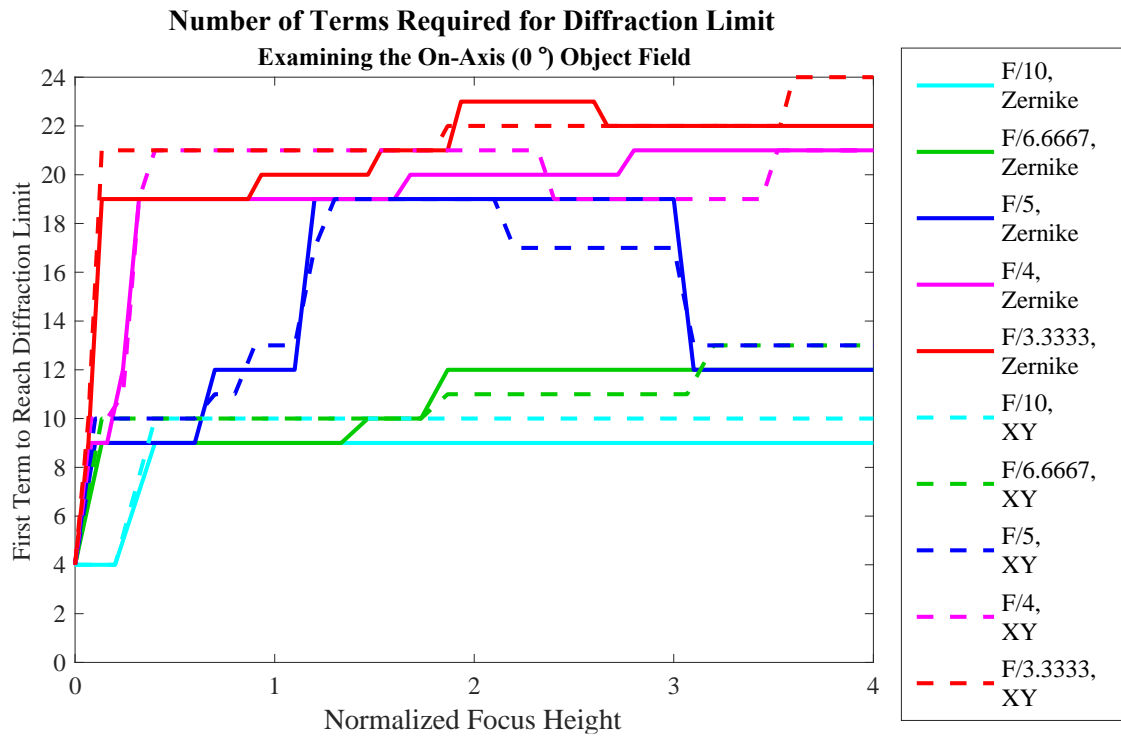


**Figure 2.3-7—Number of Zernike and XY coefficients required for imaging convergence on a diffraction-limited RMS image size as a function of normalized focus height**

The similarities might also be attributable to an effective aspheric surface that can still focus the image despite surface tilt. If this was the case, the impact of the XY and Zernike polynomials is reduced.

See Table 2-6 for a continued description of the results seen in Figure 2.3-7.

**Table 2-6—Number of coefficients needed for refractive imaging convergence**

Parent F-number	Required XY	Corresponding Polynomial Order	Required Zernike (withholding piston)	Corresponding Polynomial Order
3.33	24	6	23 [24]	6
4	21	6	21 [22]	6
5	19	5	19 [20]	5
6.67	13	4	12 [13]	4
10	10	4	9 [10]	3

Figure 2.3-8 details the impact of fourth, fifth, sixth, and eighth order polynomials on image size. It demonstrates that sixth order polynomials were able to converge on a diffraction-limited solution for both surface types. It also highlights the Zernike polynomials' superior ability to converge on smaller image sizes than the XY polynomials once fifth order polynomials were utilized.

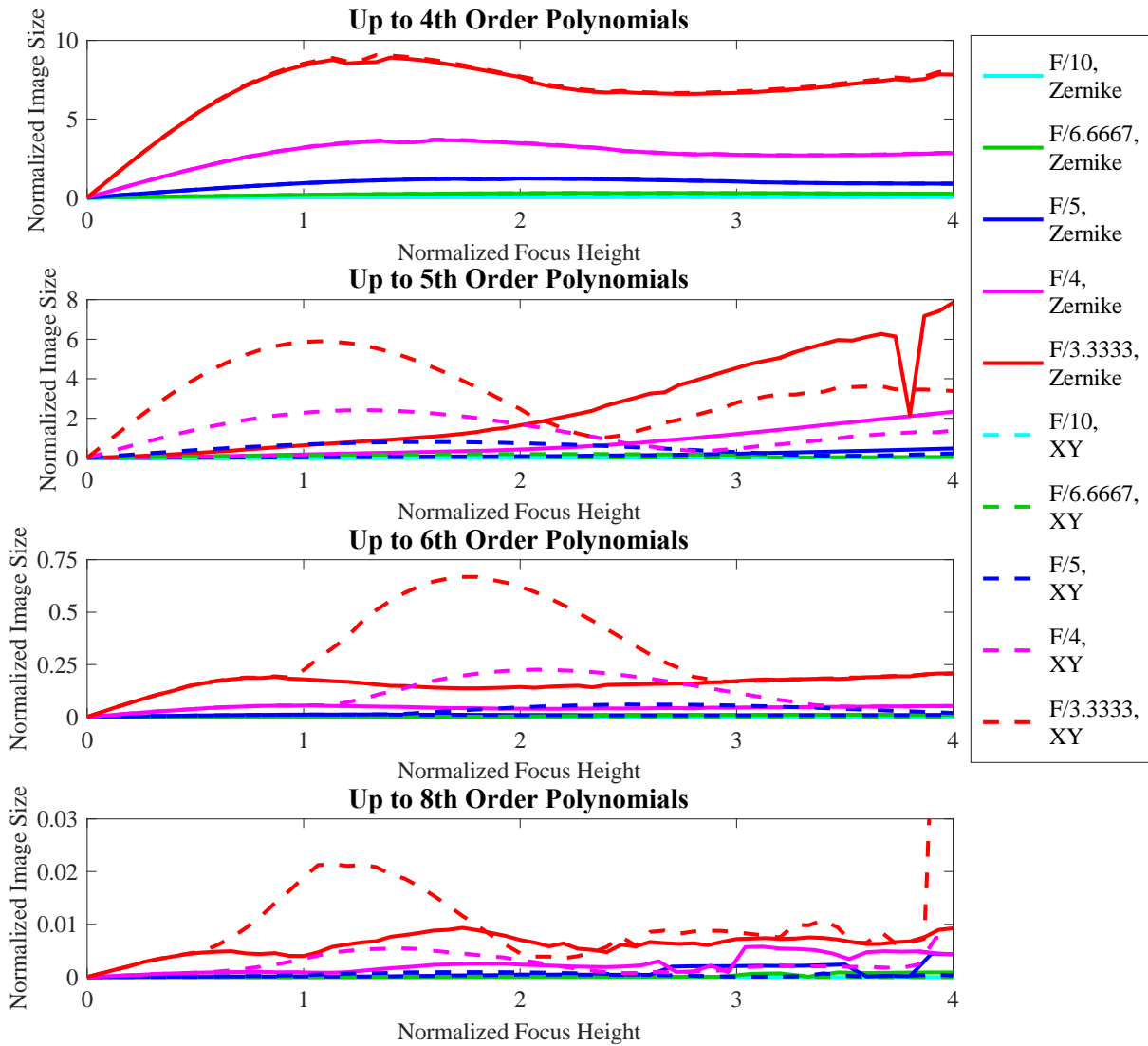


**Figure 2.3-8—Examining the effect that adding polynomial orders has on the scaled RMS image size (when normalized to the Airy disk diameter, any value <1 is diffraction-limited)**

### 2.3.4.2. System with a Field of View

The lens layout for one of the field of view scenarios is shown in Figure 2.3-9.

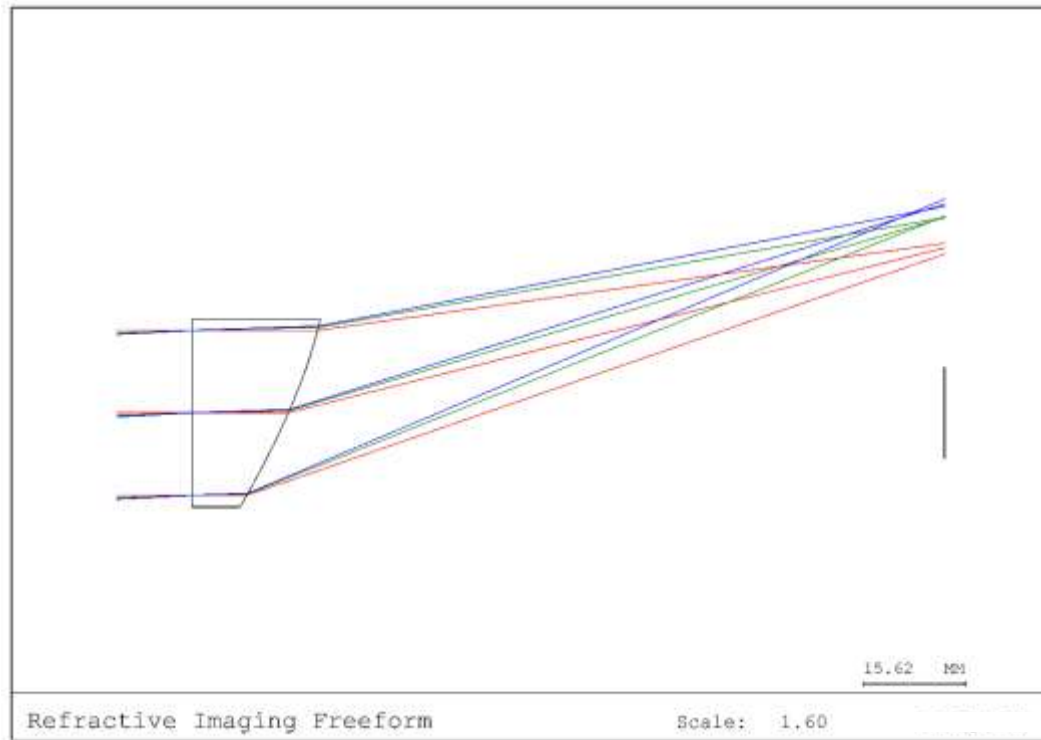


**Figure 2.3-9—Freeform lens with a 25-mm EPD, a 25-mm focus height from the on-axis object, and with the largest object field angle of 1°**

Figure 2.3-10 shows the image size for each different object field (on-axis, 70% field, full field) involved in each field of view scenario (1° FOV, 2° FOV, 3° FOV, and 4° FOV). As expected when going off-axis, the image size increased as the focus height increased.

While the image sizes for the 70% object field was comparable to the Airy disk diameter, the image sizes for the other two object fields made these lens systems impractical for any system that desires a focused image. However, this freeform setup was effective in redirecting on-axis object rays to an off-axis location.

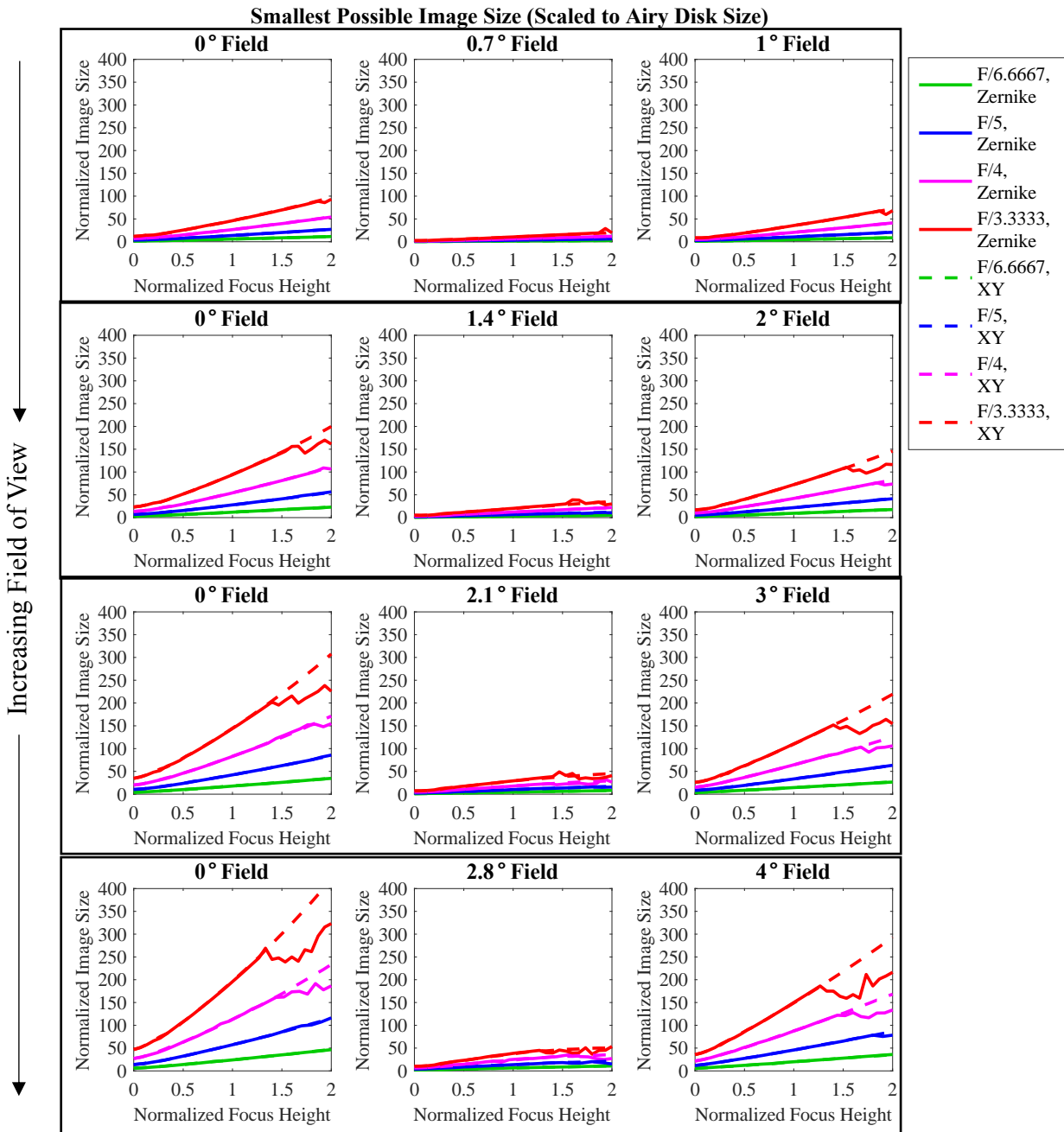


**Figure 2.3-10—Minimized scaled image size as a function of normalized focus height for the system with a field of view, arranged vertically by increasing FOV (any value <1 is diffraction-limited)**

Figure 2.3-11 represents the number of XY and Zernike terms it took to achieve the image size obtained in Figure 2.3-10. In general, the number of required terms was between 30 and 40, which corresponded to seventh to eighth order polynomials.

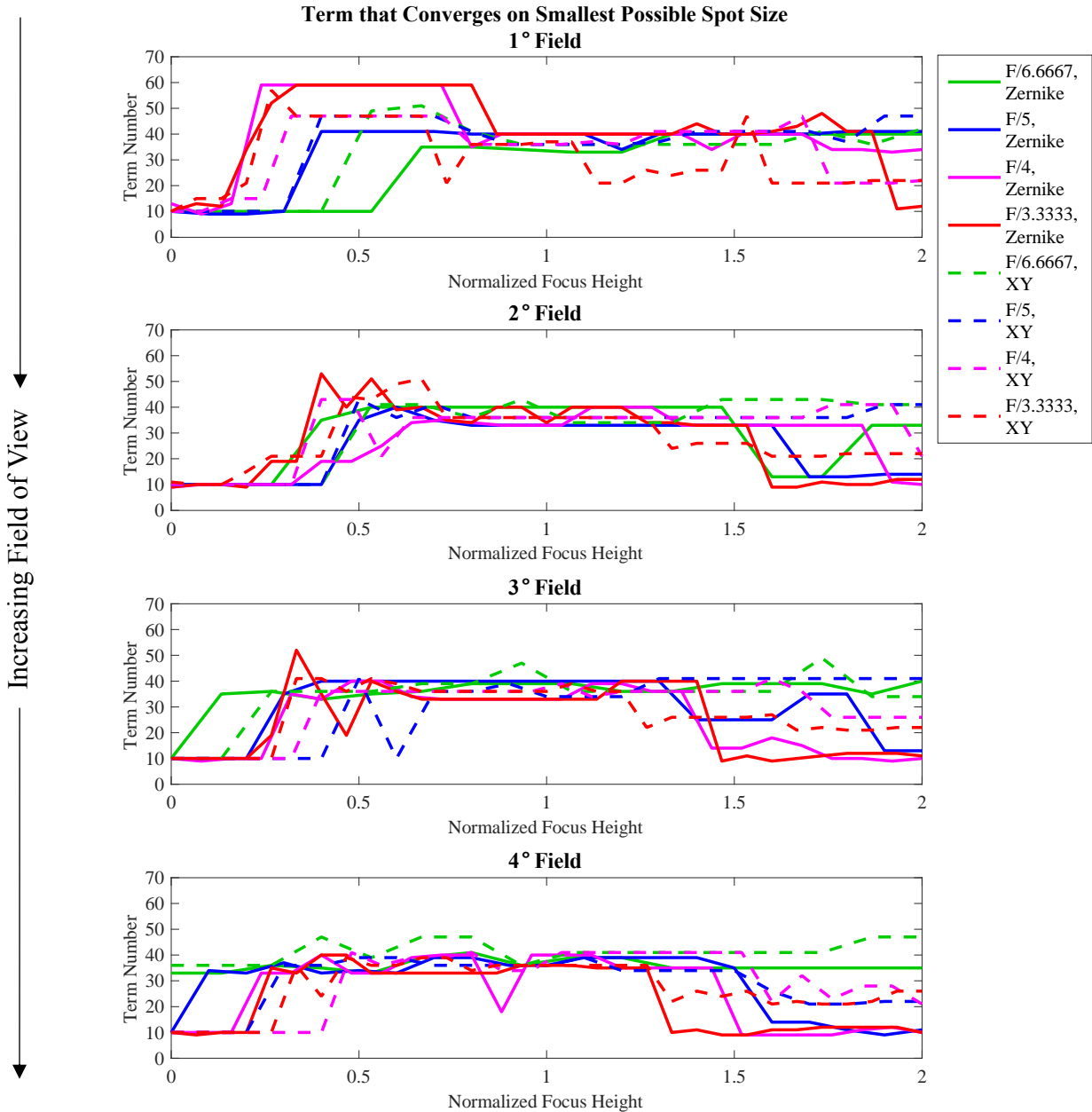


**Figure 2.3-11—Term that converges on minimized image size as a function of normalized focus height, for the system with a field of view and arranged vertically by increasing FOV**

Figure 2.3-12 demonstrates the MTF amplitudes for a selected spatial frequency of 25% of the cutoff frequency. The MTF degraded to an unusable contrast as the focus height increased. Like

the image size trends, the 70% extent object field was likely usable, but the other two fields (on-axis and full extent) had significantly lower contrast, which reduced the system's overall ability. It should be noted that the MTF remained stable for a range of 0 to 1  $H_{scaled}$ , which was where the focus height had yet to depart the boundary on the image plane defined by the entrance pupil.

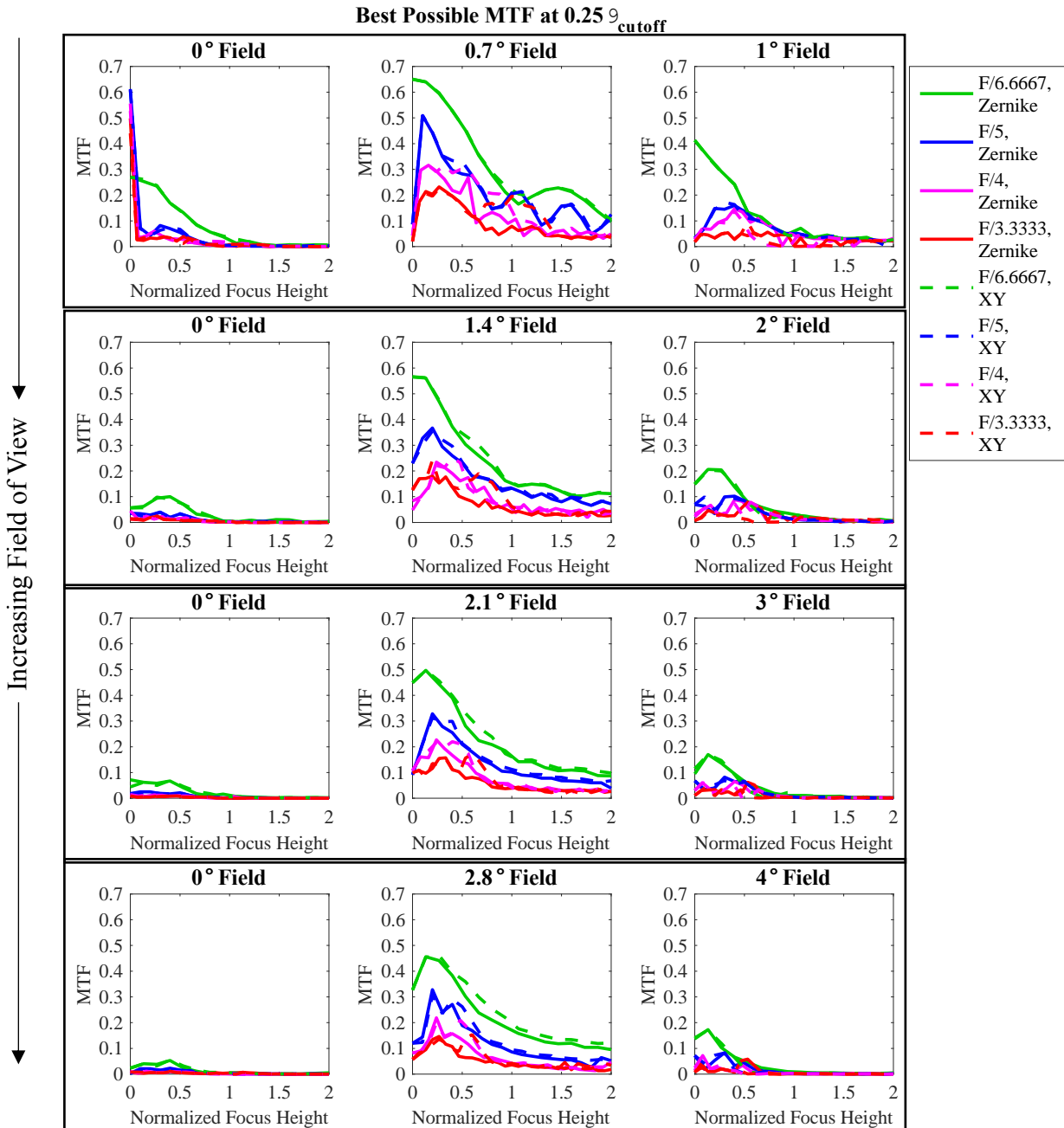


**Figure 2.3-12—MTF at 0.25 of the spatial cutoff frequency as a function of the normalized focus height, for the system with a field of view and arranged vertically by increasing FOV**

For plots describing the terms that converged on these MTF values, see Appendix, Figure 5.1-1.

Lastly, the MTF amplitudes for a spatial frequency of 10 line pairs per mm is demonstrated in Figure 2.3-13. As the F/# increased and as the focus height neared its extreme value, the MTF degraded much like it did in Figure 2.3-12.

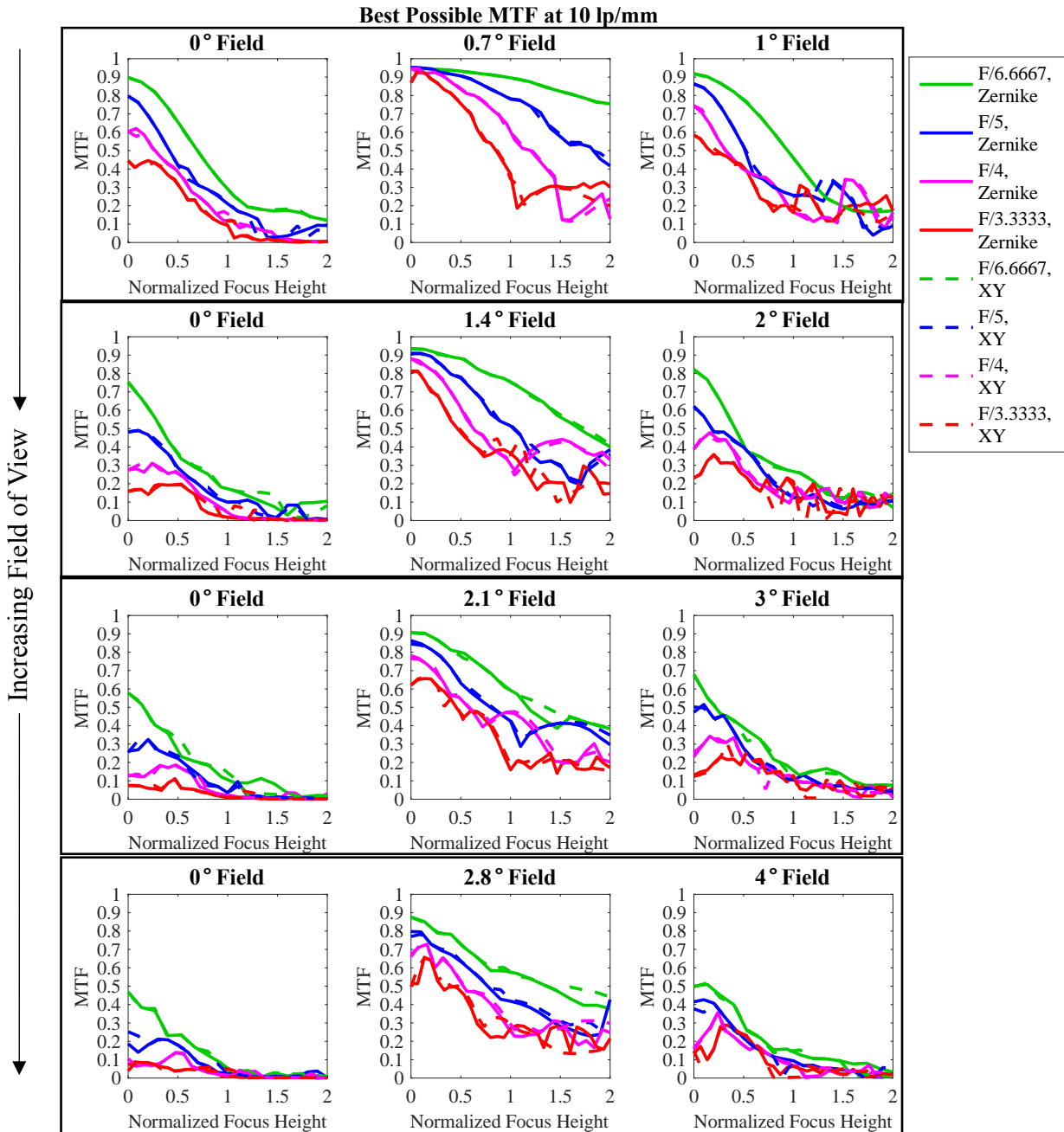


**Figure 2.3-13—MTF amplitude at 10 line pairs per mm as a function of the normalized focus height, for the system with a field of view and arranged vertically by increasing FOV**

For plots describing the terms that converge on these MTF values, see Appendix, Figure 5.1-2.



The results seen in Figure 2.3-14 aim to verify the discussion in Section 2.1. With the overlapping image size plots for the various F-numbers, the plot does just that. The overlapping plots indicate a successful freeformity definition independent of the parent F/# and solely dependent on focus height.

The MTF trends with the 10 lp/mm spatial frequency was not included in this section because it is a fixed spatial frequency and does not scale with a change to the system F-number, which would show no significance as the freeformity changes.

Finally, Figure 2.3-15 shows the MTF trend for the 25% of the cutoff spatial frequency plotted as a function of the freeformity. Although these results do not overlap like those in Figure 2.3-14, the trend of general similarity further indicates that the freeformity definition is valid.

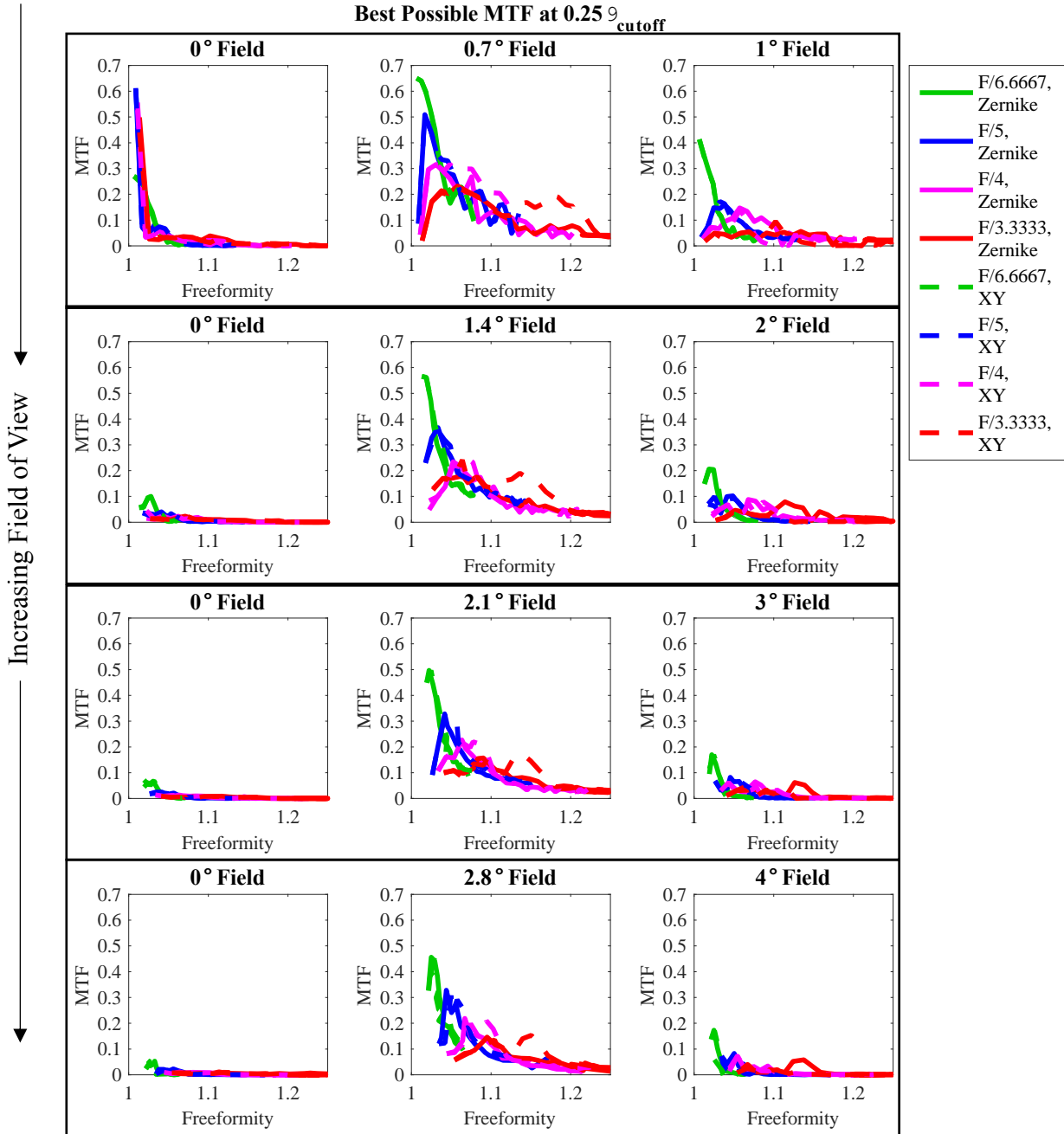


**Figure 2.3-15—MTF for 0.25 of the spatial cutoff frequency as a function of freeformity, for the system with a field of view and arranged vertically by increasing FOV**

## 2.4. Conclusions

Because the test runs were performed with an automated process, the automatic designs used to optimize the imaging scenarios may not represent the best possible results, so there is error associated with the image quality metrics. However, the trends are exceedingly important.

The overall results of the study indicate that neither XY nor Zernike polynomials are capable of being used to design a robust single-element freeform focusing lens. While the Zernike polynomials often resulted in utilizing fewer terms to converge on a solution, the solution was still not effective.

This could, of course be an artifact of the design goal, which was rather aggressively trying to perform near diffraction limits for a single-element lens system that has no other means of compensating for aberrations.

Concerning the dispute about which basis space better defines freeform surfaces, Cartesian or Zernike, there have certainly been many academic investigations into the subject of lens design with freeform surfaces. Milena Nikolic and her fellow authors studied an optical design for a head-worn displays in which she optimized with Legendre, Zernike, Q-Legendre, and Forbes polynomials [15]. She convincingly found that the Cartesian basis spaces converged on a better MTF and RMS spot size when compared to the polar basis space of the Zernike polynomials. With that said, the XY polynomials are not orthogonal polynomials, and therefore are not representative of a polynomial surface type that could compete with the Zernike polynomials. Should this analysis be repeated, an investigation into another polynomial type should be considered a high priority.

### 3. Illumination Design Scenario

The museum community utilizes freeform optical surfaces to better control the illumination of their exhibits [27]. Architectural lighting designs optimize for brightness uniformity to enhance observer experience and for reduced flux levels to prevent damage to the illuminated surfaces.

#### 3.1. Case Study Description

*Green on Blue* by Mark Rothko resides at The University of Arizona Museum of Art, pictured in Figure 3.1-1. The exhibit is enclosed in a walled feature to draw the observer into an intimate viewing experience (see Figure 3.2-1). To effectively illuminate the full enclosure, the museum is collaborating with the College of Optical Sciences to reduce the light levels in the viewing space while maximizing the uniformity across the painting and onto the wall surrounding it.



NOTE—Photo courtesy of Nathan Saxton/University of Arizona Museum of Art. Picture provided by UANews at <https://uanews.arizona.edu/story/a-light-touch-for-museum-artwork>.

**Figure 3.1-1—*Green on Blue* on display at the University of Arizona Museum of Art**

## 3.2. Generating Illumination Freeform Optics

The LightTools 8.4 software package, from Synopsys, Inc., was used to generate these freeform illumination surfaces. This software takes input system requirements for the source and the target as well as a desired optical surface type (refractive or reflective) and tailors the surface accordingly. The tailoring creates a map along the freeform with surface normal vectors that extend to the target to achieve the desired target distribution. It then creates a three-dimensional surface using B-spline surface interpolation.

In this design space, the source is defined as the origin. As for the coordinate system, the vector in the opposite direction of the surface normal is the  $z$  axis, and, the horizontal and vertical axes are  $x$  and  $y$ , respectively.

Here, the source is hung from the already-existing light track in the ceiling. It is longitudinally displaced by 1.25 meters and vertically displaced from the painting center by 3.175 meters.

The painting itself is 2.286 meters tall and is placed 0.254 meters above the floor, as demonstrated in Figure 3.2-1. The target's vertical dimension is the summation of the two: 2.794 meters.

The target's horizontal dimension is the combination of the 1.626-meter painting width and the 0.419-meter wall space to its left and right (not labelled in the schematic). This amounts to a target horizontal dimension of 2.464 meters.

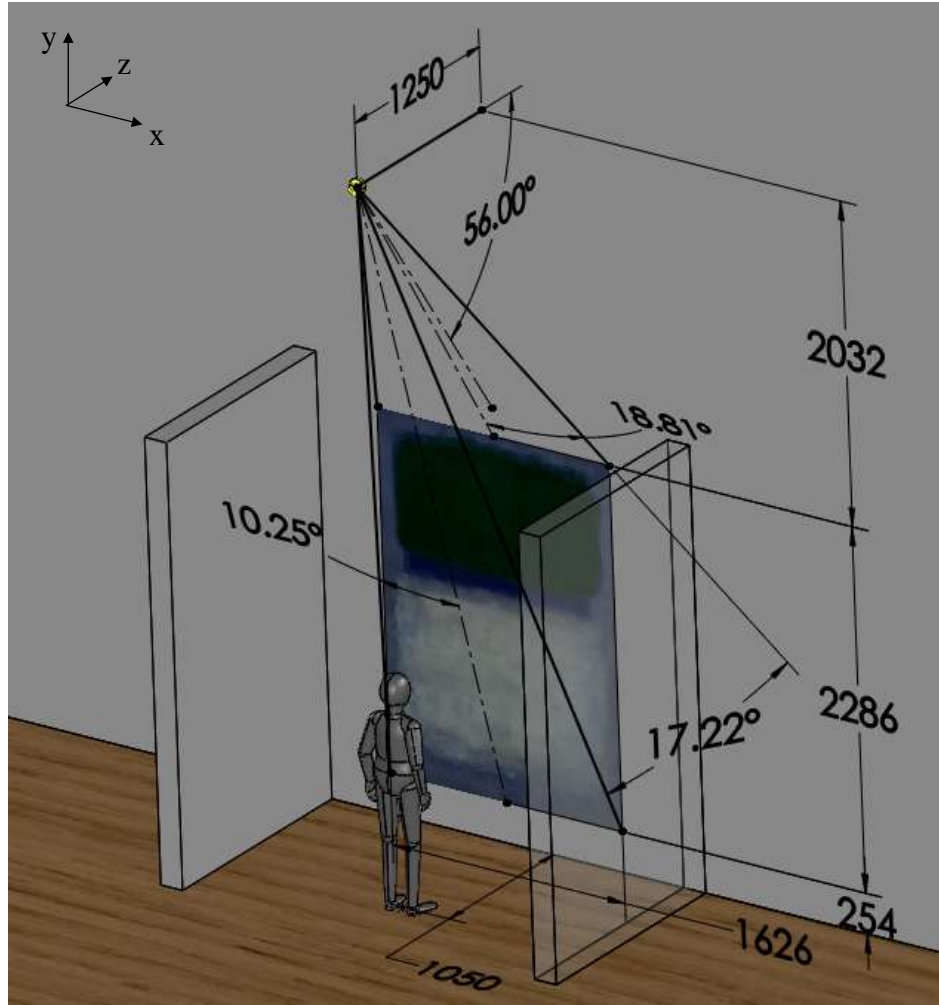


**Figure 3.2-1—Anticipated design configuration for the illumination freeform**

In general, a significant influence on the freeform surface shape is the vector defining the pointing angle of the source, as well as the emission cone angle defining the angular extent. Equation (3-1) depicts the nominal pointing vector  $y$ -angle arising from the source's locational displacement from the center of the painting.

$$\theta_{nominal} = \tan^{-1} \left( \frac{\Delta y_{T,center}}{\Delta z_{T,center}} \right) = \tan^{-1} \left( \frac{-3175 \text{ mm}}{1250 \text{ mm}} \right) = -68.51^\circ \quad (3-1)$$

Additionally, the spacing between the source and the freeform must be initialized, effectively defining the preliminary width and height of the freeform. And, finally, the source type must be defined. Typically, the design module utilizes a Lambertian isotropic source. However, the

optimization results reached in the following sections replaced it with a  $0.25 \text{ mm}^2$  extended source with the same emission cone angle. As a result, the freeform surface calculation was generated with a more realistic light source.

From these input parameters, the design module prepared a preliminary optical surface that resulted in a target lacking brightness in the outer corners of its spatial distribution [18]. To counter this low uniformity, the freeform surface was calculated such that the rays in the central angular distribution of the source were displaced toward the edges of the target spatial map [7]. This effectively reduced the target intensity in the center while increasing it on the outer edges.

The actual freeform calculation involved manipulating the optical surface until a uniform map of target rays was reverse-ray-traced to a single point at the source location [3]; [10].

The output of this freeform optical surface was merely a shape defined by an  $x$ - $y$ - $z$  point cloud. This shape is not optimized for a real illumination system in which the source was extended to a realistically sized LED. To perform this realistic source optimization, the shape must be fitted to some differentiable function, which is discussed in the following section.

### 3.3. Functional Fitting of Illumination Freeform Surfaces

Contrary to the polynomials used in Section 2, the fitting of the point clouds designed for this illumination scenario did not utilize a baseline aspheric surface. Instead, they were fit with Legendre and Zernike polynomials, which are both orthogonal functions. The property of orthogonality is crucial for fitting because it involves the combination of linearly independent polynomials, and it ensures a resulting continuous function that is infinitely differentiable [14].

Two-dimensional Legendre polynomials are separable in their  $x$  and  $y$  components, while two-dimensional Zernike polynomials are separable in their radial and azimuthal components. Since the point cloud is given in  $x$ - $y$ - $z$  coordinates, it is easiest to remain in the same Cartesian coordinate system when generating the fit function. Therefore, the Zernike polynomials were converted to a Cartesian coordinate system, which is discussed in detail in Section 3.3.1.

The fitting was performed in MATLAB by inputting the  $x$  and  $y$  matrices of the freeform point cloud as independent variables, and the  $z$  matrix as the dependent variable. Since the desire was to understand the number of polynomials it takes to fit certain freeform surfaces, each freeform point cloud was fit starting with six polynomials, then the number of used polynomials is incremented by one until 100 polynomials were involved in the fit. It was done incrementally to observe the ability for the function to converge on a minimum RMS error solution for every single added term.

For each converged surface solution, the RMS and peak-to-valley (PV) error in the fit was collected. Low RMS error is an indication of proper fit convergence. However, fitting functions tend to oscillate or “ring” at the surface’s edges, which is described by Runge phenomenon [9]. This ringing is not captured well with RMS error, but it is well-described by peak-to-valley error. The ringing effect is mitigated as higher order polynomial terms are added, but evidence of it could be lost without assessing the PV error of the fit.

Despite converting the Zernike function to a Cartesian formula, it still resides within a polar-based basis space. As a result, the function may not be able to efficiently converge on a result for surfaces that are significantly asymmetric.

### 3.3.1. Zernike Polynomials

The conventional definition for Zernike polynomials was defined in Equations (2-7) through (2-9). These equations are orthogonal over the unit circle, but separable in a polar coordinate system, which relies on an origin point [19]. For optics that are rotationally symmetric about the optical axis, the origin point is straightforward. But, when a surface is freeform, the origin point becomes more difficult to isolate, which degrades the convergence ability of the fitting function. This assertion implies that the polar-based fitting functions will not converge as well as Cartesian-based when fitting more-freeform surfaces.

The method by which Zernike polynomials are converted to a Cartesian coordinate system is defined throughout the duration of this section.

The conventional polar-to-Cartesian conversion is shown in Equation (3-2) through (3-4) [19].

$$\rho^2 = x^2 + y^2 \quad (3-2)$$

$$x = \rho \cos(\varphi) \quad (3-3)$$

$$y = \rho \sin(\varphi) \quad (3-4)$$

To start, a re-written recursive solution for the radial polynomials is given in Equation (3-5) [25].

$$R_n^m(\rho) = \left[ \sum_{k=0}^{n-m} \frac{(-1)^k (2n-m-k)!}{k! (n-k)! (n-m-k)!} \rho^{2(n-m-k)} \right] \cdot \rho^m \quad (3-5)$$

This expression allows for the separation of the  $m^{th}$  order radial component ( $\rho^m$ ), which can directly pair with the  $m^{th}$  order azimuthal component ( $\cos(m\varphi)$  or  $\sin(m\varphi)$ ) when the radial polynomial is included with the full Zernike polynomial equation,  $Z_n^m$  and  $Z_n^{-m}$ . This combination can be seen in Equations (3-9) (positive  $m$ ) and (3-11) (negative  $m$ ).

For notational ease, a separate radial polynomial,  $\mathcal{R}$ , is used to define a new recursive relationship.

$$R_n^m(\rho) = \mathcal{R}_n^m(\rho) \cdot \rho^m \quad (3-6)$$

$$\mathcal{R}_n^m(\rho) = \sum_{k=0}^{n-m} \frac{(-1)^k (2n-m-k)!}{k! (n-k)! (n-m-k)!} (\rho^2)^{(n-m-k)} \quad (3-7)$$

The new radial polynomial contains only even exponents of  $\rho$ , so it can be easily converted to Cartesian coordinates, demonstrated in Equation (3-8).

$$\mathcal{R}_n^m(x, y) = \sum_{k=0}^{n-m} \frac{(-1)^k (2n-m-k)!}{k! (n-k)! (n-m-k)!} (x^2 + y^2)^{(n-m-k)} \quad (3-8)$$

The Zernike polynomials can now be rewritten as Equations (3-9) through (3-12).

$$Z_n^m(\rho, \varphi) = \mathcal{R}_n^m(\rho) \cdot \theta_m \quad (3-9)$$

$$\theta_m = \rho^m \cos(m\varphi) \quad (3-10)$$

$$Z_n^{-m}(\rho, \varphi) = \mathcal{R}_n^m(\rho) \cdot \theta_{-m} \quad (3-11)$$

$$\theta_{-m} = \rho^m \sin(m\varphi) \quad (3-12)$$

The multiple angle formula, shown in Equations (3-13) and (3-14), provides a straightforward recursive relationship for  $\theta_m$  and  $\theta_{-m}$  [21].

$$\cos(m\varphi) = \sum_{k=0}^{\frac{m}{2}} (-1)^k \binom{m}{2k} \cos^{m-2k}(\varphi) \sin^{2k}(\varphi) \quad (3-13)$$

$$\sin(m\varphi) = \sum_{k=0}^{\frac{m-1}{2}} (-1)^k \binom{m}{2k+1} \cos^{m-2k-1}(\varphi) \sin^{2k+1}(\varphi) \quad (3-14)$$

Using the multiple angle formula, the recursive Cartesian solution for  $\theta_m$  is represented in Equation (3-18).

$$\theta_m(\rho, \varphi) = \rho^m \cos(m\varphi) \quad (3-15)$$

$$\theta_m(\rho, \varphi) = \rho^m \sum_{k=0}^{\frac{m}{2}} (-1)^k \binom{m}{2k} \cos^{m-2k}(\varphi) \sin^{2k}(\varphi) \quad (3-16)$$

$$\theta_m(\rho, \varphi) = \sum_{k=0}^{\frac{m}{2}} (-1)^k \binom{m}{2k} \rho^{m-2k} \cos^{m-2k}(\varphi) \rho^{2k} \sin^{2k}(\varphi) \quad (3-17)$$

$$\theta_m(x, y) = \sum_{k=0}^{\frac{m}{2}} (-1)^k \binom{m}{2k} x^{m-2k} y^{2k} \quad (3-18)$$

And, the recursive Cartesian solution for  $\theta_{-m}$  is represented in Equation (3-22).

$$\theta_{-m}(\rho, \varphi) = \rho^m \sin(m\varphi) \quad (3-19)$$

$$\theta_{-m}(\rho, \varphi) = \rho^m \sum_{k=0}^{\frac{m-1}{2}} (-1)^k \binom{m}{2k+1} \cos^{m-2k-1}(\varphi) \sin^{2k+1}(\varphi) \quad (3-20)$$

$$\theta_{-m}(\rho, \varphi) = \sum_{k=0}^{\frac{m-1}{2}} (-1)^k \binom{m}{2k+1} \rho^{m-2k-1} \cos^{m-2k-1}(\varphi) \rho^{2k+1} \sin^{2k+1}(\varphi) \quad (3-21)$$

$$\theta_{-m}(x, y) = \sum_{k=0}^{\frac{m-1}{2}} (-1)^k \binom{m}{2k+1} x^{m-2k-1} y^{2k+1} \quad (3-22)$$

Finally, the recursive Cartesian Zernike polynomial formulas have been deduced, seen in Equations (3-23) and (3-24). Refer to Equations (3-8), (3-18), and (3-22) for the definitions of  $\mathcal{R}_n^m(x, y)$ ,  $\theta_m(x, y)$ , and  $\theta_{-m}(x, y)$ , respectively.

$$Z_n^m(x, y) = \mathcal{R}_n^m(x, y) \cdot \theta_m(x, y) \quad (3-23)$$

$$Z_n^{-m}(x, y) = \mathcal{R}_n^m(x, y) \cdot \theta_{-m}(x, y) \quad (3-24)$$

To utilize Zernike polynomials for fitting surfaces in an orthonormal basis space, the input Cartesian coordinates must be normalized by the dimensions of the freeform surface, seen in Equations (3-25) and (3-26), where  $w_x$  and  $w_y$  are the maximum width dimensions in  $x$  and  $y$ , respectively.

$$Z_n^m(x, y) = \mathcal{R}_n^m\left(\frac{x}{w_x}, \frac{y}{w_y}\right) \cdot \theta_m\left(\frac{x}{w_x}, \frac{y}{w_y}\right) \quad (3-25)$$

$$Z_n^{-m}(x, y) = \mathcal{R}_n^m\left(\frac{x}{w_x}, \frac{y}{w_y}\right) \cdot \theta_{-m}\left(\frac{x}{w_x}, \frac{y}{w_y}\right) \quad (3-26)$$

Finally, the generating function that can replace polar Zernike polynomials with Cartesian Zernike polynomials is demonstrated in Equation (3-27).

$$f(x, y) = \sum_{n=0}^{\infty} \left[ \left( \sum_{m=1}^n \sum_{k=0}^1 a_j Z_n^{(-1)^k m}(x, y) \right) + a_{(n+1)^2} Z_n^0(x, y) \right] \quad (3-27)$$

The  $j^{th}$  coefficient is given by Equation (3-30).

$$j = (n + 1)^2 - 2m + k \quad (3-28)$$

**Table 3-1—Cartesian symmetry of first 16 Zernike polynomials [12]**

<b>Term #</b>	<b>Polynomial Order, <math>n</math></b>	<b>Zernike Polynomial <math>Z_j = \mathcal{R}_r \cdot \theta_p</math></b>	<b>Symmetry in <math>x</math></b>	<b>Symmetry in <math>y</math></b>
1	0	$Z_1 = \mathcal{R}_0^0 \cdot \theta_0$	even	even
2	1	$Z_2 = \mathcal{R}_1^1 \cdot \theta_1$	odd	even
3	1	$Z_3 = \mathcal{R}_1^1 \cdot \theta_{-1}$	even	odd
4	1	$Z_4 = \mathcal{R}_1^0 \cdot \theta_0$	even	even
5	2	$Z_5 = \mathcal{R}_2^2 \cdot \theta_2$	even	even
6	2	$Z_6 = \mathcal{R}_2^2 \cdot \theta_{-2}$	odd	odd
7	2	$Z_7 = \mathcal{R}_2^1 \cdot \theta_1$	odd	even
8	2	$Z_8 = \mathcal{R}_2^1 \cdot \theta_{-1}$	even	odd
9	2	$Z_9 = \mathcal{R}_2^0 \cdot \theta_0$	even	even
10	3	$Z_{10} = \mathcal{R}_3^3 \cdot \theta_3$	odd	even
11	3	$Z_{11} = \mathcal{R}_3^3 \cdot \theta_{-3}$	even	odd
12	3	$Z_{12} = \mathcal{R}_3^2 \cdot \theta_2$	even	even
13	3	$Z_{13} = \mathcal{R}_3^2 \cdot \theta_{-2}$	odd	odd
14	3	$Z_{14} = \mathcal{R}_3^1 \cdot \theta_1$	odd	even
15	3	$Z_{15} = \mathcal{R}_3^1 \cdot \theta_{-1}$	even	odd
16	3	$Z_{16} = \mathcal{R}_3^0 \cdot \theta_0$	even	even

### 3.3.2. Legendre Polynomials

To form higher order polynomials, Legendre polynomials satisfy the recurrence relationship described in Equation (3-29), while the first two Legendre polynomials are defined in Equation (3-30) [1].

$$(n + 1)L_{n+1}(x) = x(2n + 1)L_n(x) - nL_{n-1}(x) \quad (3-29)$$

$$L_0(x) = 1, L_1(x) = x \quad (3-30)$$

Legendre polynomials in two-dimensions can be written as the combination of two polynomials separable in Cartesian coordinates, seen in Equation (3-31) [12]. The first 10 two-dimensional Legendre polynomials are found in Table 3-2.

$$Q_j(x, y) = L_l(x) \cdot L_m(y) \quad (3-31)$$

The  $j^{th}$  coefficient is given by Equation (3-32).

$$j = \frac{(l + m)^2 + l + 3m}{2} + 1 \quad (3-32)$$

**Table 3-2—Cartesian symmetry of first 10 Legendre polynomials [12]**

<b>Term #</b>	<b>Polynomial Order <math>n = l + m</math></b>	<b>Legendre Polynomial <math>Q_j(x, y) = L_l(x) \cdot L_m(y)</math></b>	<b>Symmetry in <math>x</math></b>	<b>Symmetry in <math>y</math></b>
1	0	$Q_1(x, y) = L_0(x) \cdot L_0(y)$	even	even
2	1	$Q_2(x, y) = L_1(x) \cdot L_0(y)$	odd	even
3	1	$Q_3(x, y) = L_0(x) \cdot L_1(y)$	even	odd
4	2	$Q_4(x, y) = L_2(x) \cdot L_0(y)$	even	even
5	2	$Q_5(x, y) = L_1(x) \cdot L_1(y)$	odd	odd
6	2	$Q_6(x, y) = L_0(x) \cdot L_2(y)$	even	even
7	3	$Q_7(x, y) = L_3(x) \cdot L_0(y)$	odd	even
8	3	$Q_8(x, y) = L_2(x) \cdot L_1(y)$	even	odd
9	3	$Q_9(x, y) = L_1(x) \cdot L_2(y)$	odd	even
10	3	$Q_{10}(x, y) = L_0(x) \cdot L_3(y)$	even	odd

To properly use these polynomials in the intended orthonormal basis space, the input  $x$  and  $y$  variables are normalized by the  $x$ - and  $y$ -dimensions of the freeform, seen in Equation (3-33).

$$Q_j(x, y) = L_l\left(\frac{x}{w_x}\right) \cdot L_m\left(\frac{y}{w_y}\right) \quad (3-33)$$

Finally, the Legendre expansion for the freeform surface is found in Equation ...

$$f(x, y) = \sum_{j=1}^{\infty} a_j Q_j(x, y) \quad (3-34)$$

### 3.3.3. Leveraging Symmetry to Improve Computational Efficiency

If even-symmetry is present in a system, odd-symmetric polynomials are not needed. Unfortunately, the symmetry of a curve is not immediately recognized by a fitting algorithm, so it will utilize every given polynomial to converge on a solution, including those that are odd-symmetric. This means that any fitting polynomial with odd-symmetry about the axis under consideration will be competing with the much-needed even polynomials during optimization, which is computationally expensive because the fit is wasting effort by utilizing terms that will not contribute to convergence.

To reduce computation efforts for this case study, it was recognized that these freeform surfaces have plane symmetry about the  $x$ -axis. Therefore, each surface's odd polynomial terms are zeroed in the fit function to cancel their contributions.

It is straightforward to apply this to Legendre functions since these two-dimensional polynomials are structured from the multiplication of an  $x$ -polynomial and a  $y$ -polynomial. With this math, the fitting algorithm simply includes two-dimensional terms that have odd exponents for the  $x$ -polynomial.

For Zernike functions, the odd- $x$  polynomials arise from the odd- $m$  azimuthal polynomials for the  $\theta_m$  term and from the even- $m$  azimuthal polynomials for the  $\theta_{-m}$  term.

### 3.4. Illumination with Refractive Freeforms

The refractive illumination system requirements, guided by the discussion in Section 3.2, are provided in Table 3-3. Additionally, this refractive optical element will include a Cartesian oval at the first refracting surface to increase the source collection angle without affecting the refraction of the freeform surface [13]; [18]. See the effect it has on the collection cone angle in Table 3-4.

**Table 3-3—Design constraints for refractive illumination scenario**

The source shall be placed at the horizontal center of the painting.	
Utilize a Cartesian oval for the first surface of the optic. The surface vertex shall be displaced by 6mm and have a virtual source $z$ offset of 2mm.	
Design wavelength	550 nm
Refractive index of freeform material	1.5896
Source vertical ( $y$ ) displacement (from painting center)	3175 mm
Source longitudinal ( $z$ ) distance from the face of the painting	1250 mm
Distance from source to freeform surface	15 mm
Minimum target uniformity	10%
Horizontal source pointing direction ( $x$ angle)	0°
Vertical source pointing direction ( $y$ angle)	<i>Varies, specifics provided in Table 3-5</i>
Source full emission cone angle	

**Table 3-4—Effect of including Cartesian oval in the refractive illumination design**

Cone Angle Accepted by Freeform	New Cone Angle with Cartesian Oval
70°	94.94°
75°	100.66°
80°	106.256°
85°	111.738°
90°	117.116°

To understand the asymmetry properties of the freeform shape as the source is pointed at different vertical locations along the target, the freeform surfaces were designed with the parameters listed in Table 3-5.

**Table 3-5—Specifics of refractive illumination varied parameters**

Parameter	Minimum Value	Increment	Maximum Value
Vertical Source Pointing Direction (y angle)	42.5 degrees	2.5 degrees	80 degrees
Source Full Emission Cone Angle Accepted by the Freeform	70 degrees	5 degrees	90 degrees

A ray trace of a generated freeform refracting optic is shown in Figure 3.4-1. The resulting target distribution is shown in Figure 3.4-2.

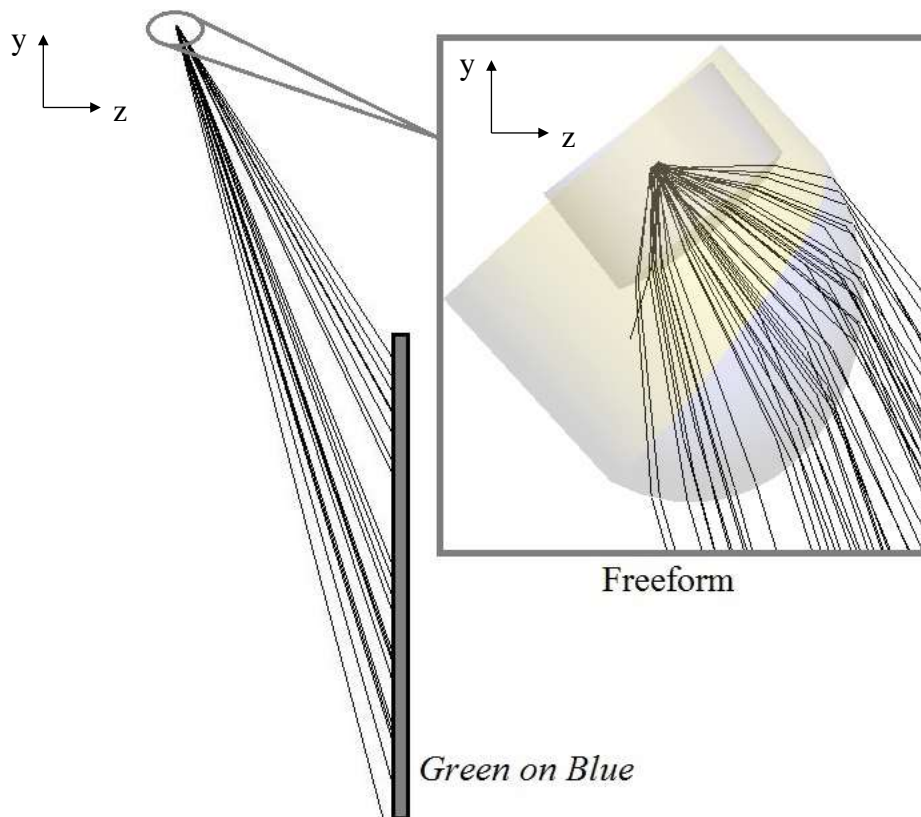


**Figure 3.4-1—Refractive illumination freeform with the source at a -50° Y-tilt and a 70° collection cone angle**

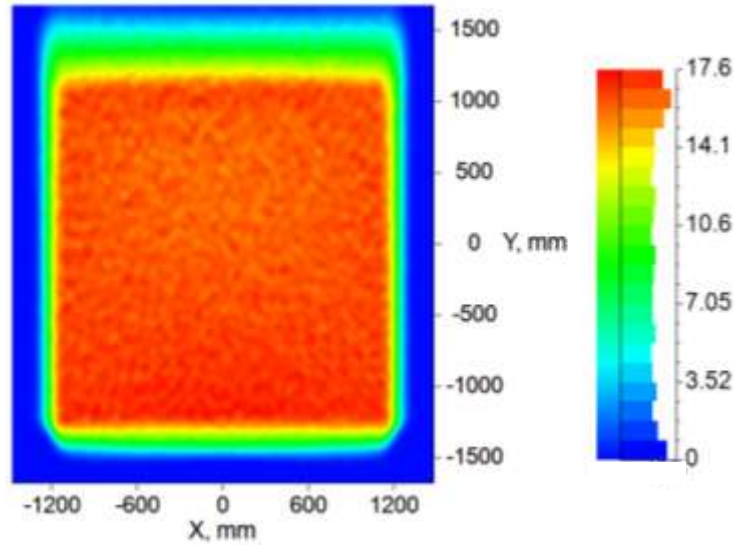


**Figure 3.4-2—Target illumination map for a refractive freeform with a  $-57.5^\circ$  source Y-tilt and  $94.9^\circ$  emission cone ( $70^\circ$  cone collected by the freeform). 2 billion rays were traced.**

A closer look at the symmetry properties of the freeform can be observed in Figure 3.4-3.

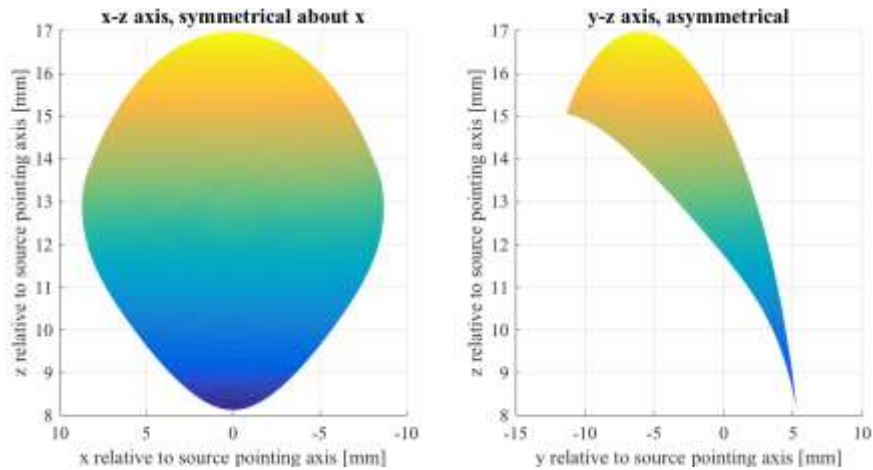
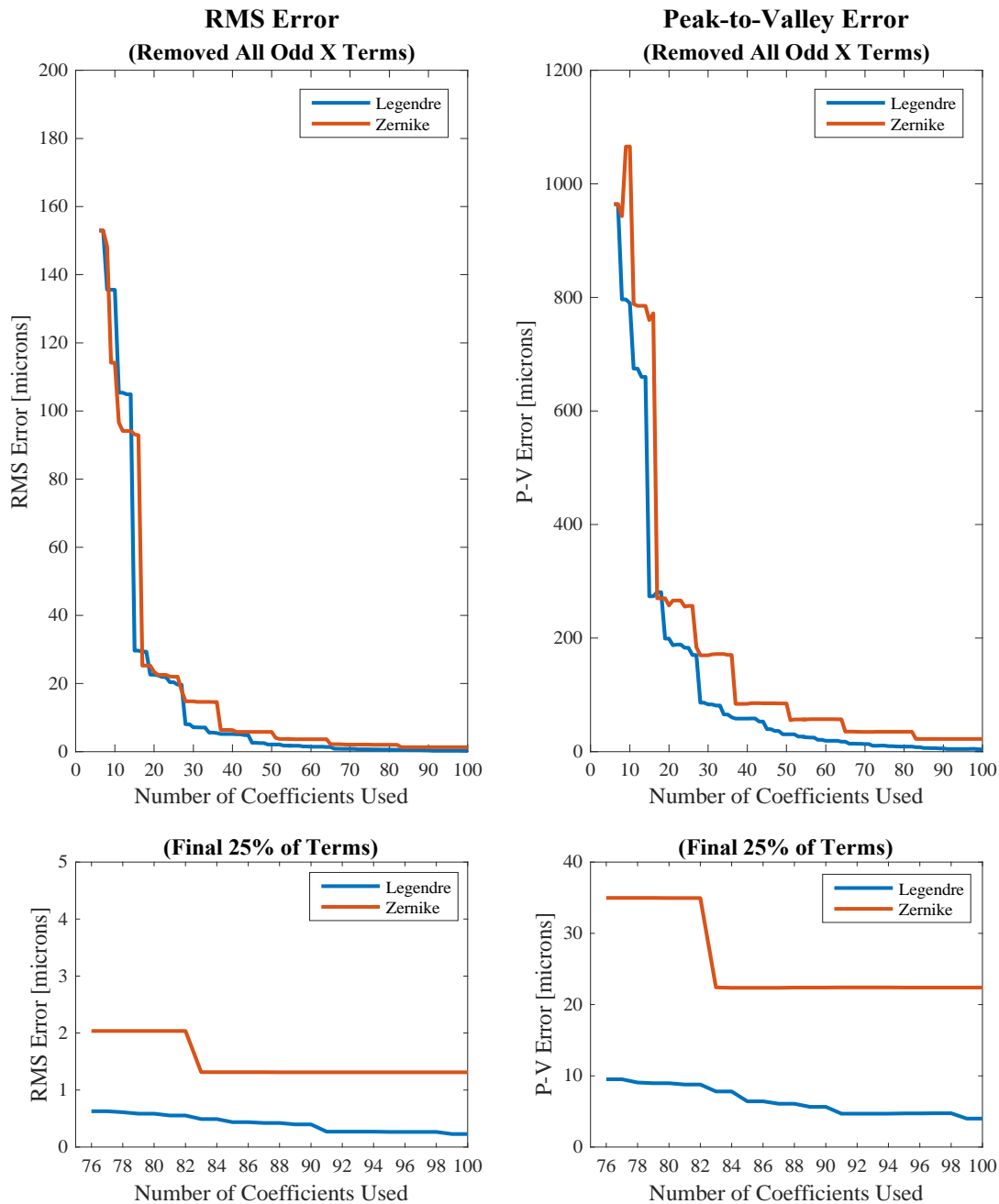


**Figure 3.4-3—X and Y symmetry properties of the refractive freeform**

### 3.4.1. Functional Fitting Results

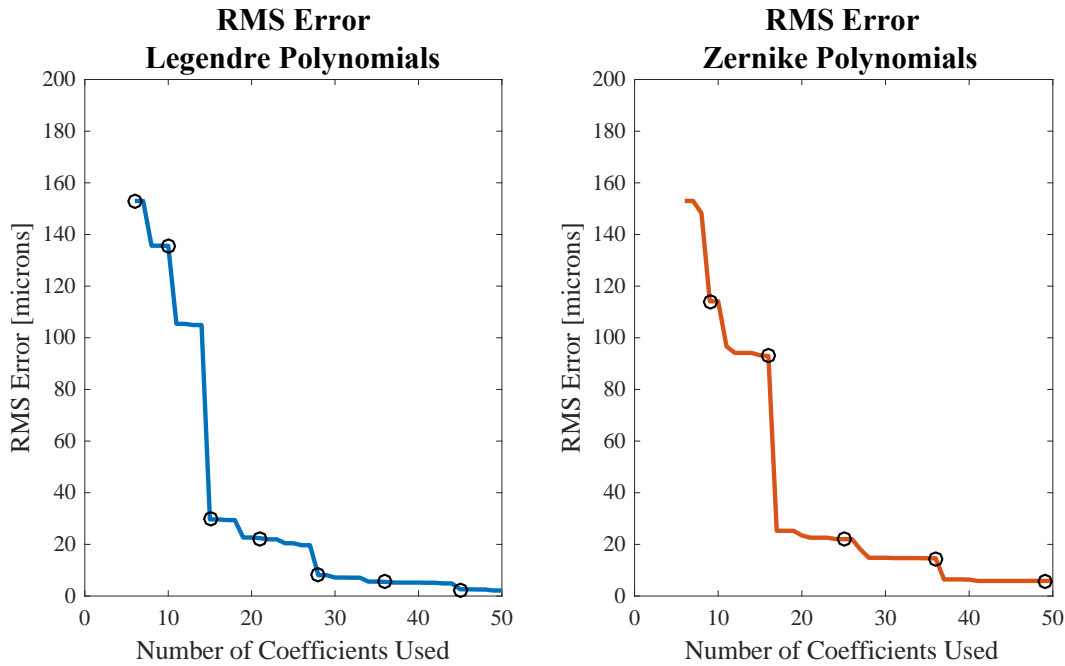
Each generated freeform surface was then fit according to the process described in Section 3.3, which removed odd-x polynomial terms and fits for an incrementing number of included coefficients.

Figure 3.4-4 demonstrates the typical RMS and PV error trends for a fit surface as a function of the number polynomial terms added. These trends demonstrate that the Legendre fitting function is more capable of converging on a smaller RMS and PV error beyond the first 20 coefficients. This figure represents the freeform optic that demonstrated the most optimal illumination efficiency (see the calculation for this in Appendix, Section 5.2.1.1).



**Figure 3.4-4—Fit behavior of the freeform for a 57.5° source Y-tilt and 70° cone angle accepted by the freeform**

Upon further examination of these trends, the freeform shape becomes more apparent. Figure 3.4-5 isolates the RMS error of the two fit functions and highlights what occurs when introducing new polynomial orders. Table 3-6 describes terms causing a significant reduction in the RMS error.



NOTE—Black circles represent terms that introduce a larger y-exponent.

**Figure 3.4-5—RMS error trends, highlighting the effect of adding new polynomial orders**

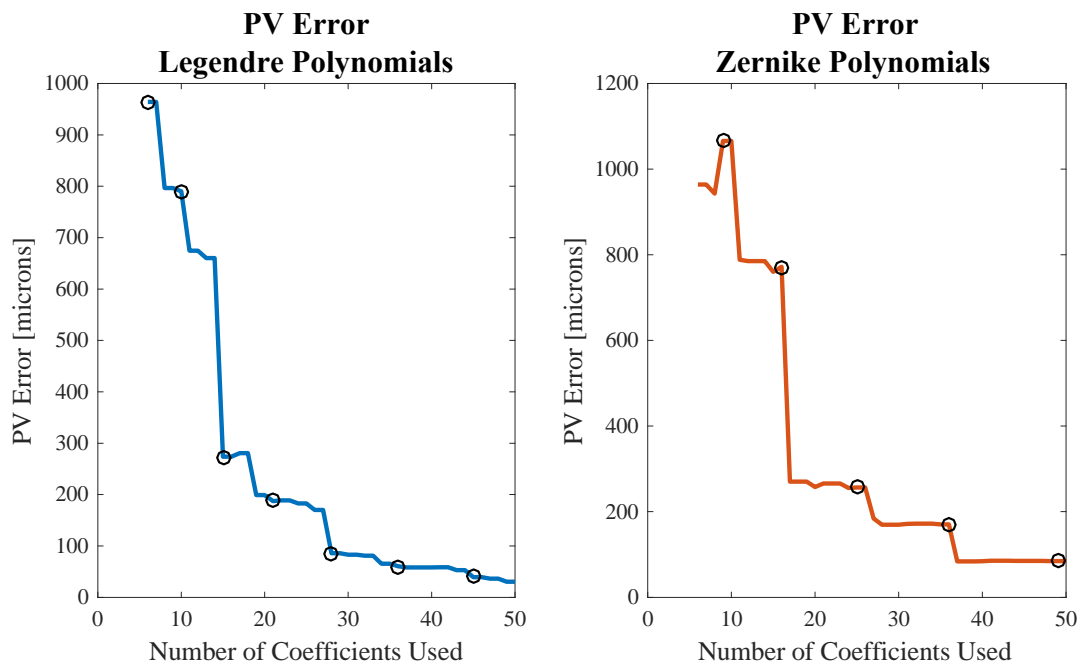
**Table 3-6—Terms that significantly reduce the RMS error in the computed fit surface**

Legendre			Zernike		
Term	Polynomial	Significance	Term	Polynomial	Significance
8	$L_2(x) \cdot L_1(y)$	1 <sup>st</sup> order $y$ terms, 2 <sup>nd</sup> order $x$ terms	9	$6\rho^4 - 6\rho^2 + 1$	quartic surface
11	$L_4(x) \cdot L_0(y)$	4 <sup>th</sup> order $x$ terms	11	$\rho^3 \sin(3\varphi)$	3 <sup>rd</sup> order $y$ term
15	$L_0(x) \cdot L_4(y)$	4 <sup>th</sup> order $y$ terms	17	$\rho^4 \cos(4\varphi)$	4 <sup>th</sup> order $y$ term, 4 <sup>th</sup> order $x$ term
19	$L_2(x) \cdot L_3(y)$	3 <sup>rd</sup> order $y$ terms, 2 <sup>nd</sup> order $x$ terms	27	$\rho^5 \sin(5\varphi)$	5 <sup>th</sup> order $y$ term
28	$L_0(x) \cdot L_6(y)$	6 <sup>th</sup> order $y$ terms	37	$\rho^6 \cos(6\varphi)$	6 <sup>th</sup> order $y$ term, 6 <sup>th</sup> order $x$ term

The results in Table 3-6 indicate that the freeform is quartic in  $x$  and  $y$  because the most significant RMS reduction is at the 11th and 15th Legendre polynomial (quartic  $x$  and quartic  $y$ , respectively), and at the 17th Zernike polynomials (quartic  $x$  and  $y$ ). The  $y$  shape is also heavily impacted by the inclusion of other even-exponent terms, which indicates that there is some level of symmetry along the surface's tilted axis introduced by the first order  $y$  polynomial.

Another artifact of Figure 3.4-4 and Figure 3.4-5 is that the Zernike trend flat-lines after a significant RMS error decline, while the Legendre trend uses the intermediary fitting terms to converge on a smaller RMS solution. This means that the intermediary Zernike fit terms are not needed for RMS convergence, while the Legendre fit requires a significant number of its other polynomials to minimize the RMS error.

The PV error trends follow a similar behavior to the RMS error trends, particularly when introducing a new polynomial order. See this effect in Figure 3.4-6.



NOTE—Black circles represent the last term of a polynomial order.

**Figure 3.4-6—PV error trends when new polynomial orders are introduced**

For all other generated refractive freeform point clouds, the same type of analysis in Figure 3.4-4 was performed to observe the effect of adding new polynomial orders. To keep the remaining discussion brief, a specific source emission cone angle was selected.

For each source emission cone angle, the RMS and PV errors of a full 100-coefficient fit were compared amongst all source pointing angles ( $42.5^\circ$ ,  $50^\circ$ ,  $\dots$ ,  $80^\circ$ ) — the pointing angle with the smallest error was selected from each. These results are presented in Figure 3.4-7. The plots on the left demonstrate the pointing angle that produces the minimized RMS and PV error for each emission cone angle, and the plots on the right demonstrate the smallest achievable RMS and PV errors for each emission cone angle.

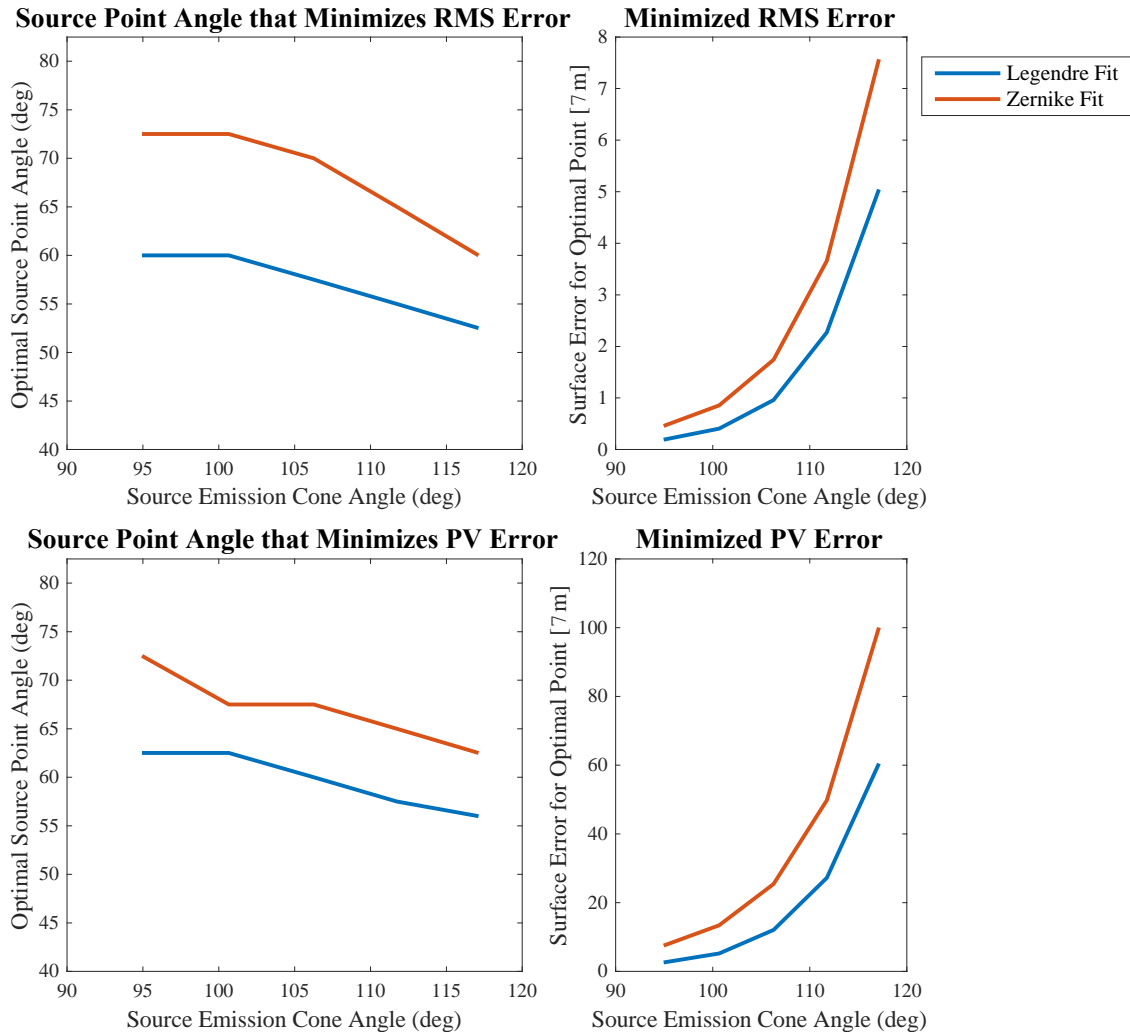


**Figure 3.4-7—Demonstrating the effect that source emission cone angle has on the fit error of the refractive illumination freeforms (RMS, PV error results from a fit using 100 terms)**

As indicated in Figure 3.4-7, a smaller cone angle provides better convergence. Therefore, all freeform point clouds with a  $94.9^\circ$  cone angle drive the remaining discussions.

The desire was to observe the effect that the pointing angle has on the fit. Figure 3.4-8 shows the RMS error results for freeform fits done with 17, 37, 66, and 100 used coefficients for point clouds made for a  $94.9^\circ$  source emission cone angle. The used coefficient amounts other than 100 were selected because both Zernike and Legendre have up to fourth order polynomials for 17 used terms, sixth order polynomials for 37 used terms, and eighth order polynomials for 66 used terms.

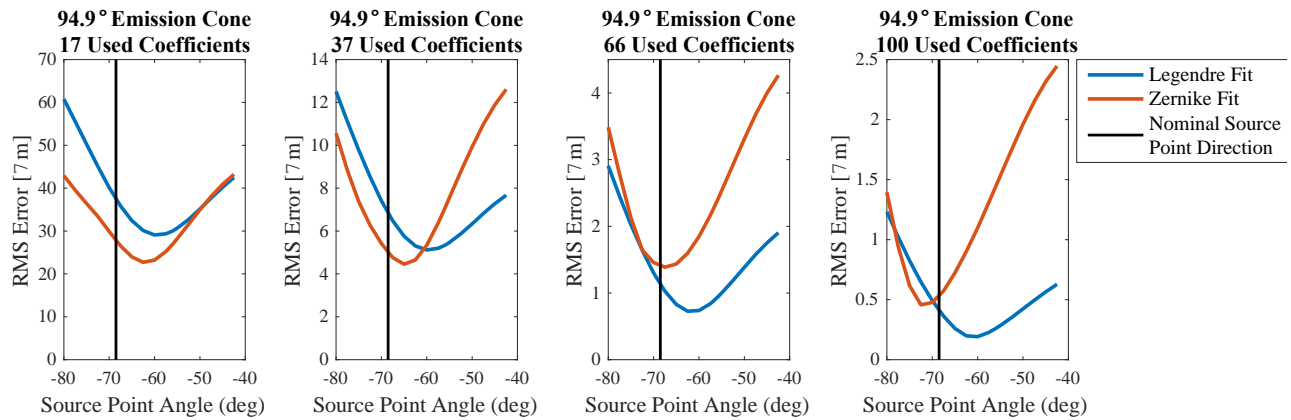


**Figure 3.4-8—Examining the refractive illumination freeform RMS error as a function of the source point angle for the inclusion of different polynomial orders**

The RMS error trends demonstrate that the Zernike fit has better convergence when the source pointing angle is near that of the nominal source point direction, as defined in Equation (3-1) (if the source were to be pointed at the center of the painting). This indicates that the freeform surfaces generated for near-nominal source point directions may be more rotationally or elliptically defined due to its high level of convergence with Zernike polynomials, a polar-based function.

However, the Legendre convergence is overall more effective once the fits reach 8th order polynomials. And, the Legendre fit optimal pointing angle is positively-deviated from the nominal point direction. Considering this illumination scenario, the freeform optic must direct more light to the bottom of the target. Therefore, this optic's point cloud must be shaped such that it re-directs light below the pointing angle (see Figure 3.4-10). This freeform shape is significantly less rotationally symmetric, which results in a better Cartesian-based fitting convergence.

Figure 3.4-9 demonstrates the PV error results for the same scenario. Like the trend for RMS error, the Legendre fit converges on a smaller PV error once 8th order polynomials are used. However, the PV error for Legendre does not differ much from the Zernike when the fit solely consists of lower-order polynomial terms.

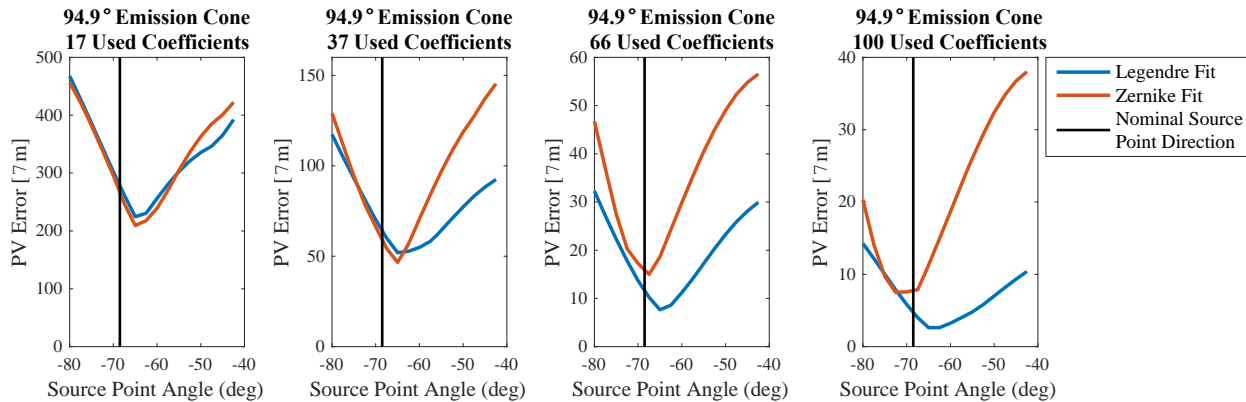


**Figure 3.4-9—Examining the refractive illumination freeform PV error as a function of the source point angle for different coefficient amounts**

To investigate the reason why both PV and RMS error are different when deviating from the nominal source point direction, the  $x$  and  $y$  cross-sections are investigated in Figure 3.4-10, and Figure 3.4-11, and Figure 3.4-12.

The figures clearly demonstrate the extent to which the surfaces deviate from axial symmetry. For the  $-67.5^\circ$   $y$ -tilt, the closest to the nominal point direction, the freeform is the most line-symmetric about  $y$ , which likely indicates why it works well for Zernike polynomials. Because of the  $y$ -symmetry, it can define a base origin location somewhere near its polar axis frame.

However, as the pointing direction deviates from the optimal point angle, the freeform shape also deviates greatly from line symmetry and the Zernike fit cannot compensate as well as Legendre can due to the complexity of the new origin location.

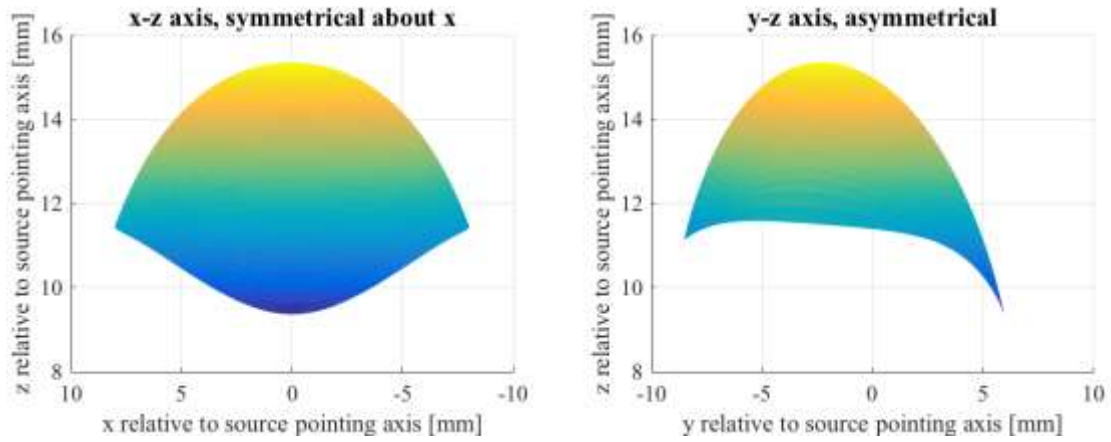


**Figure 3.4-10—Freeform for source with  $-60^\circ$  y-tilt and  $70^\circ$  cone (best Legendre RMS)**

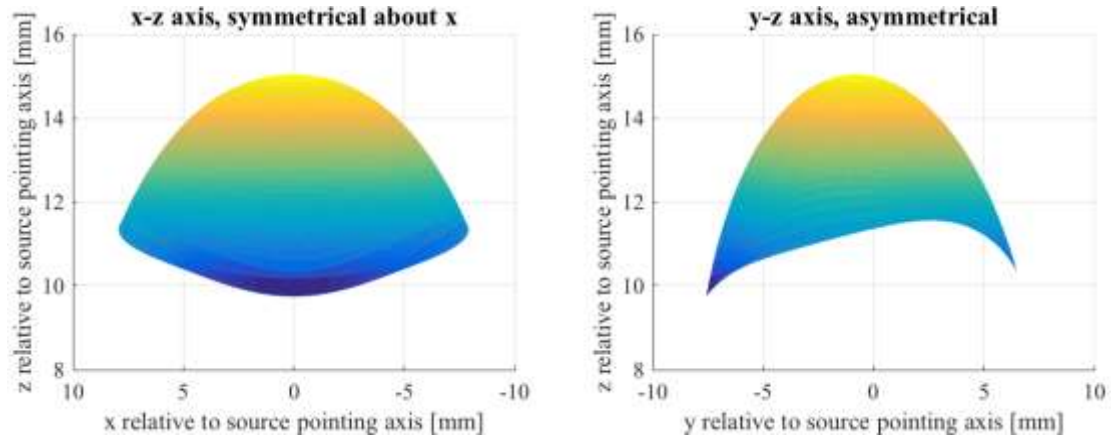


**Figure 3.4-11—Freeform for source with  $-67.5^\circ$  y-tilt and  $70^\circ$  cone (best Legendre RMS)**

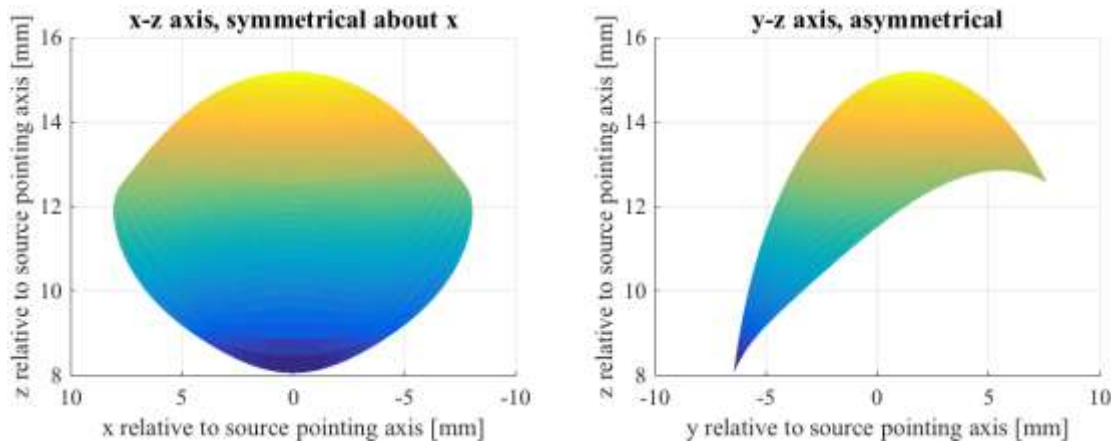


**Figure 3.4-12—Freeform for source with  $-80^\circ$  y-tilt and  $70^\circ$  cone (best Legendre RMS)**

## **3.5. Illumination with Reflective Freeforms**

There are several options for illuminating with reflective freeforms if the systems are well-defined by edge rays. Koshel offers two classes of conic systems that employ edge-ray designs: elliptical and hyperbolic [8]. Elliptical conic surfaces have a real exit-ray bundle caustic, while hyperbolic have a virtual caustic [23].

While it is possible to pursue these efforts with an elliptical conic, this case study selected a hyperbolic design to prevent the source rays from crossing over at a real caustic.

Winston, Miñano, and Benítez explore a rigorous hyperbolic surface solution using a spherically symmetric point source to illuminate a target plane with a predetermined intensity distribution [23]. However, this approach is defined for an axially symmetric concentrator, which cannot uniformly illuminate the tilted target plane that is present in the Rothko illumination case study.

Instead, a tailored edge-ray design must tailor the hyperbolic surface to project the exiting illumination wavefront onto the target plane [8]. This involves diverging from classical reflector designs and entering the world of freeform surfaces. LightTools goes through this process in its freeform design algorithm.

### **3.5.1. Defining Reflective Illumination Design Constraints**

The reflective illumination design is similar to the refractive design, but the source must be pointed in different directions such that a reflection may occur. The specific requirements are listed in Table 3-7.

**Table 3-7—Design constraints for reflective illumination scenario**

The source shall be positioned such that it does not block any rays reflected toward the target.	
The exit ray bundle shall not crossover, or the exit ray bundle shall be virtual.	
The source shall be positioned at the horizontal center of the painting.	
Design Wavelength	550 nm
Source Height Position (Y)	3175 mm
Source Distance from the Face of the Painting (Z)	1250 mm
Spacing from Source to Freeform Surface	25 mm
Minimum Target Uniformity	10%
Horizontal Source Pointing Direction (X or horizontal angle)	0 degrees
Vertical Source Pointing Direction (Y or vertical angle)	<i>Varies, specifics provided in Table 3-8</i>
Source Full Emission Cone Angle	

As in the refractive scenario, the parameters were varied to observe the effect that this has on the freeform shape. These varied parameters are described in Table 3-8.

**Table 3-8—Specifics of reflective illumination varied parameters**

Source Position Relative to Freeform	Parameter	Minimum Value	Increment	Maximum Value
Reverse-Oriented Source (see Figure 3.5-1)	Vertical Source Pointing Direction (Y angle)	180 degrees	2.5 degrees	195 degrees
	Source Full Emission Cone Angle	70 degrees	10 degrees	120 degrees
Forward-Oriented Source (see Figure 3.5-2)	Vertical Source Pointing Direction (Y angle)	37.5 degrees	2.5 degrees	60 degrees
	Source Full Emission Cone Angle	70 degrees	10 degrees	120 degrees

The ray trace for the reverse-oriented and forward-oriented reflective illumination designs can be found in Figure 3.5-1 and Figure 3.5-2, respectively.

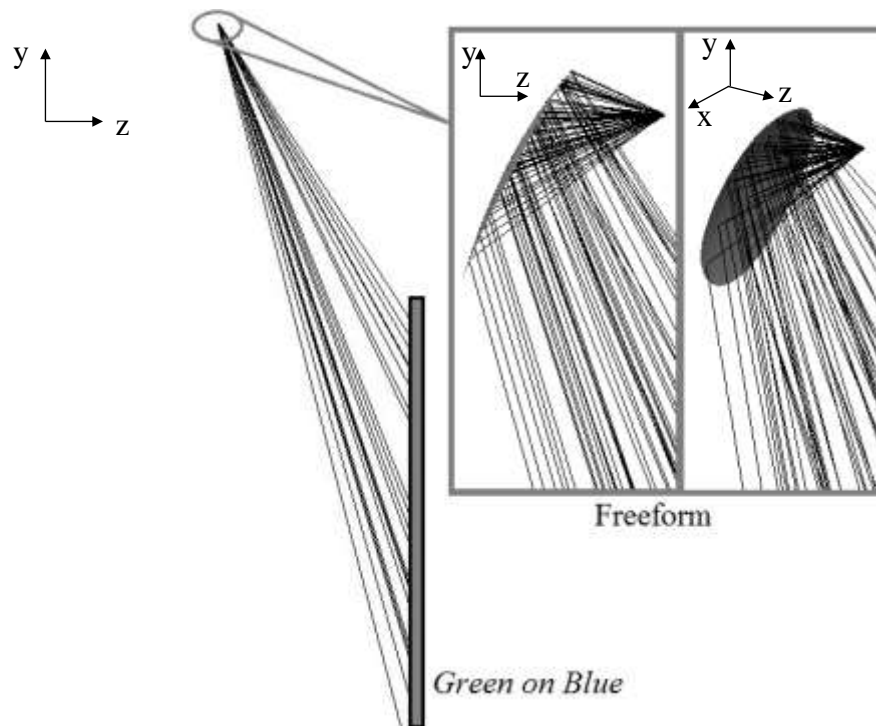


**Figure 3.5-1—Reflective illumination freeform with a reverse-oriented source, 185° Y-tilt**

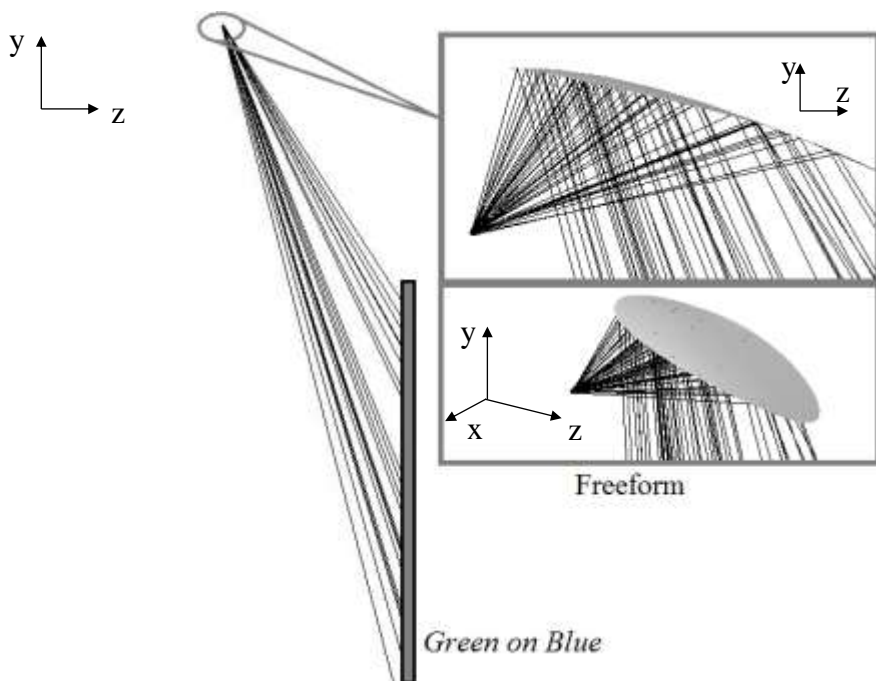


**Figure 3.5-2—Reflective illumination freeform with a forward-oriented source, 42.5° Y-tilt**

### 3.5.2. A Reflective Illumination System Optimized with a Reverse-Oriented Isotropic Source

The illumination efficiency analysis (discussed in the Appendix, Section 5.3.1) for this scenario indicates that the best point angle to use is  $185^\circ$  with a  $100^\circ$  emission cone angle. The resulting target map can be seen in Figure 3.5-3.

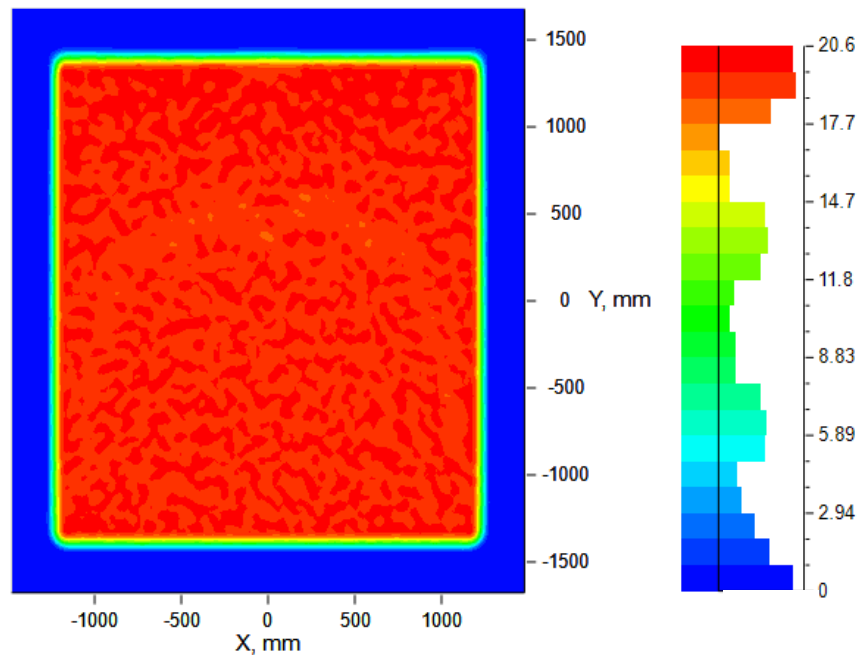
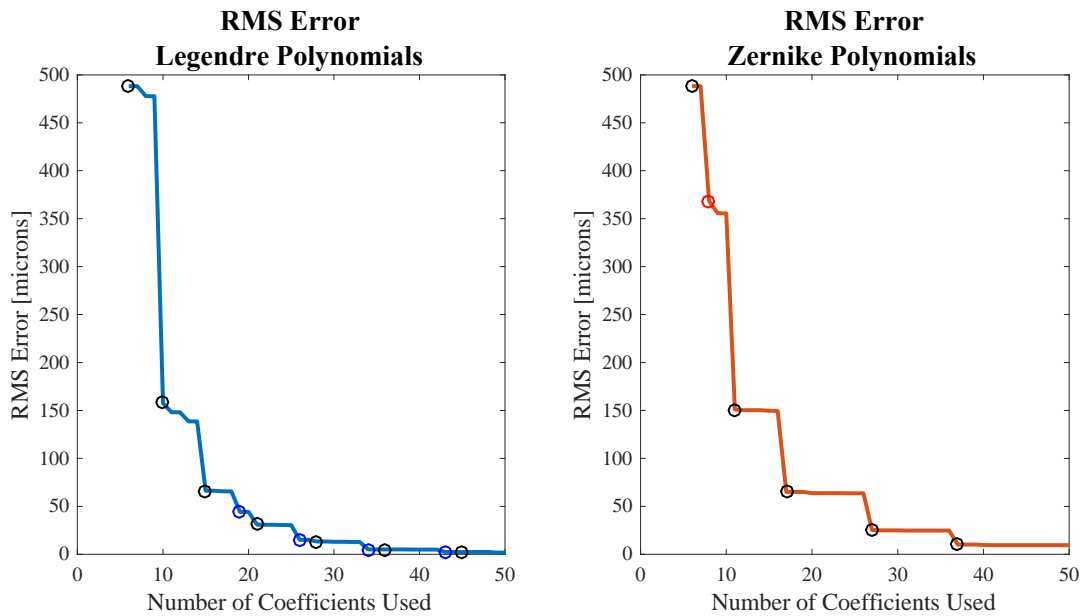


**Figure 3.5-3—Target illuminance map for a reflective freeform optic with a  $185^\circ$  Y-tilted source and a  $100^\circ$  emission cone angle. There were 2 billion rays traced.**

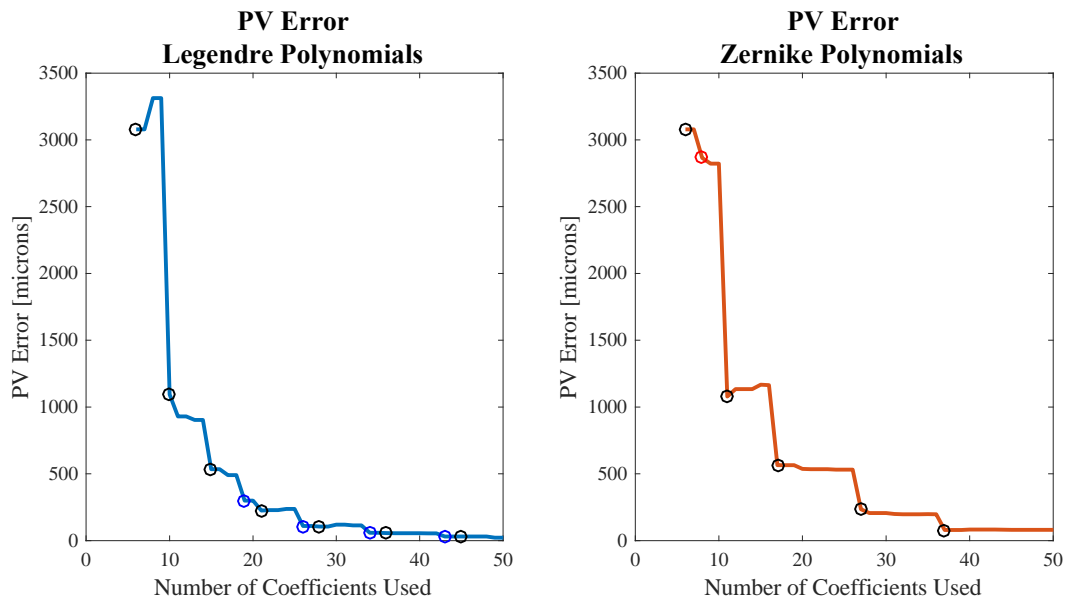
#### 3.5.2.1. Functional Fitting Results

As in the refractive case, the RMS and PV error was impacted by the addition of new polynomial terms. Looking at the Zernike fit behavior, the RMS error significantly decreased when the next higher order y-polynomial was added, as seen in the right-side plot of Figure 3.5-4. Conversely, the Legendre fit did not depend solely on the addition of new y-polynomials to reduce the RMS error. Instead, the RMS error decreased when other intermediate polynomial terms are introduced. The intermediate polynomial terms of the Zernike function were still significant because they corrected for PV error, as seen in Figure 3.5-5.



NOTE 1—Black circles represent terms that introduce a larger y-exponent.  
 NOTE 2—Other circles represent terms that reduce RMS error. See Table 3-9.

**Figure 3.5-4—RMS error trends, highlighting the effect of adding new polynomial orders**



NOTE 1—Black circles represent terms that introduce a larger y-exponent.  
 NOTE 2—Other circles represent terms that reduce RMS error. See Table 3-9.

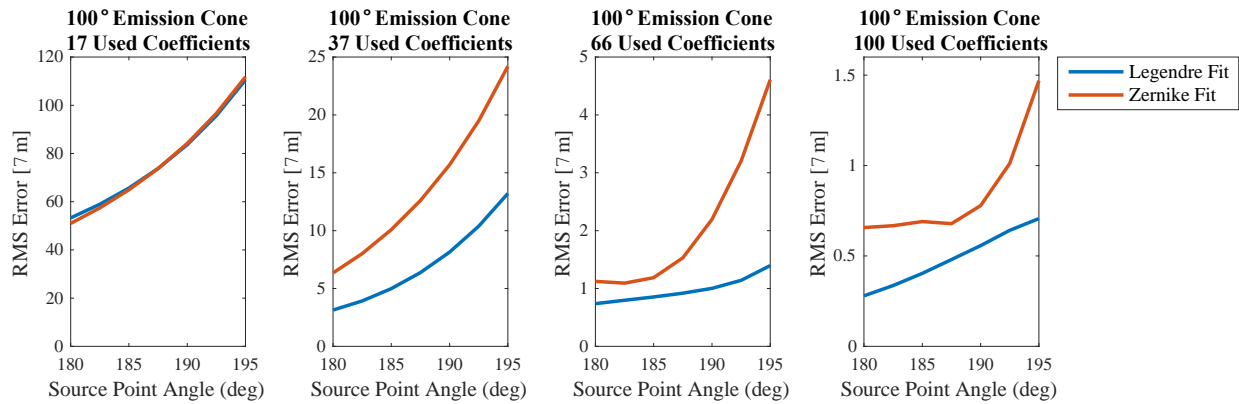
**Figure 3.5-5—PV error trends when new polynomial orders are introduced**

Table 3-9 highlights the polynomial types that caused significant change in the RMS and PV error. In general, a significant change in the Legendre trend occurs when the next large-exponent  $y$  polynomial is added. Significant changes in the Zernike trend occurs for the addition of each new azimuthal polynomial, which constitutes the addition of new  $y$ -polynomial orders.

**Table 3-9—Terms that significantly reduce the RMS error in the computed fit surface**

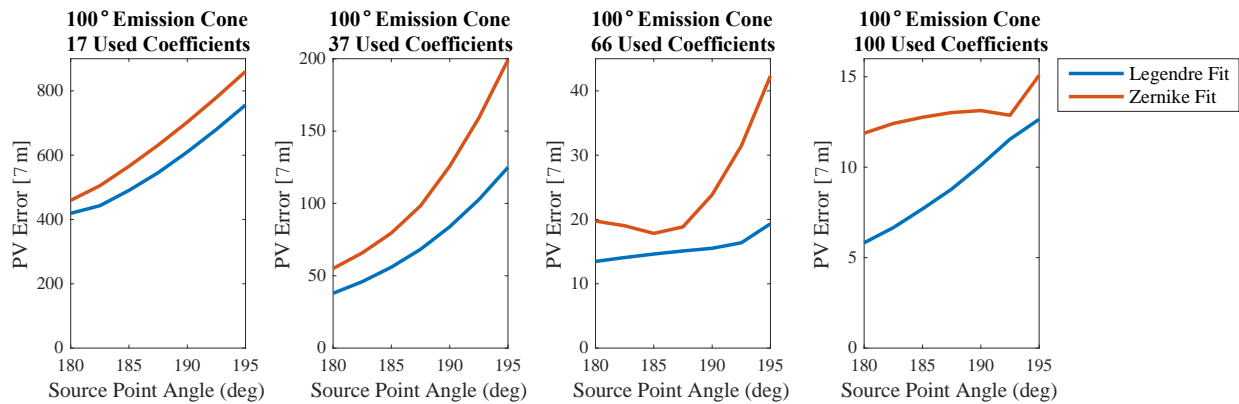
Legendre			Zernike		
Term	Polynomial	Significance	Term	Polynomial	Significance
10	$L_0(x) \cdot L_3(y)$	3 <sup>rd</sup> order $y$ terms	8	$(3\rho^2 - 2)\rho \sin(\varphi)$	circular parabola multiplied by $y$
15	$L_0(x) \cdot L_4(y)$	4 <sup>th</sup> order $y$ terms	11	$\rho^3 \sin(3\varphi)$	3 <sup>rd</sup> order $y$ term
19	$L_2(x) \cdot L_3(y)$	3 <sup>rd</sup> order $y$ terms, 2 <sup>nd</sup> order $x$ terms	17	$\rho^4 \cos(4\varphi)$	4 <sup>th</sup> order $y$ term, 4 <sup>th</sup> order $x$ term
21	$L_0(x) \cdot L_5(y)$	5 <sup>th</sup> order $y$ terms	27	$\rho^5 \sin(5\varphi)$	5 <sup>th</sup> order $y$ term
26	$L_2(x) \cdot L_4(y)$	4 <sup>th</sup> order $y$ terms, 2 <sup>nd</sup> order $x$ terms	37	$\rho^6 \cos(6\varphi)$	6 <sup>th</sup> order $y$ term, 6 <sup>th</sup> order $x$ term
34	$L_2(x) \cdot L_5(y)$	5 <sup>th</sup> order $y$ terms, 2 <sup>nd</sup> order $x$ terms	51	$\rho^7 \sin(7\varphi)$	7 <sup>th</sup> order $y$ term
43	$L_2(x) \cdot L_6(y)$	6 <sup>th</sup> order $y$ terms, 2 <sup>nd</sup> order $x$ terms	65	$\rho^8 \cos(8\varphi)$	8 <sup>th</sup> order $y$ term, 8 <sup>th</sup> order $x$ term
			83	$\rho^9 \sin(9\varphi)$	9 <sup>th</sup> order $y$ term

Figure 3.5-6 demonstrates the RMS error convergence as a function of the pointing angle for the freeforms designed for a 100° emission cone, which, per the Appendix Section 5.3.1, had the highest illumination efficiency. The trends indicate that the smaller the point angle, or the closer it is to horizontal, the better the RMS error convergence. And, yet again, the Legendre polynomials converged upon a better fit than the Zernike polynomials, indicating an inability for the rotational basis space to isolate an effective origin point.



**Figure 3.5-6—RMS error convergence trends as a function of source pointing angle for the reverse-oriented reflective illumination freeform optics**

The PV error trends, presented in Figure 3.5-7 followed the same behavior as the RMS error trends.



**Figure 3.5-7—PV error convergence trends as a function of source pointing angle for the reverse-oriented reflective illumination freeform optics**

To assess the asymmetry in these optics, the point clouds are displayed in Figure 3.5-8, Figure 3.5-9, and Figure 3.5-10, arranged in the order of increasing tilt. As clearly shown in Figure 3.5-10, the size of the freeform drastically increase to accommodate for the necessity to bend lower edge rays back towards the lower portion of the target, which results in a more asymmetric shape. The variation in the y dimension is minimal, which prevents many of the lower order even polynomials from making an impact.

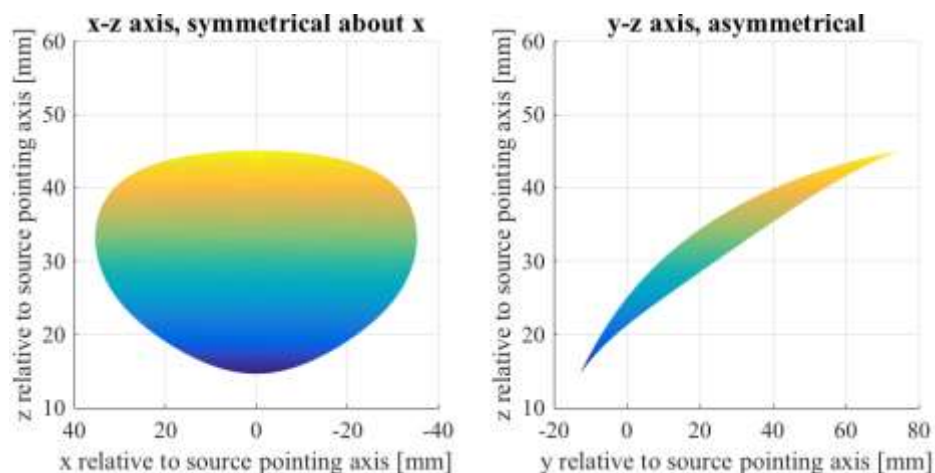


**Figure 3.5-8—Point cloud for reflective freeform with 180° y-tilt and 100° cone**

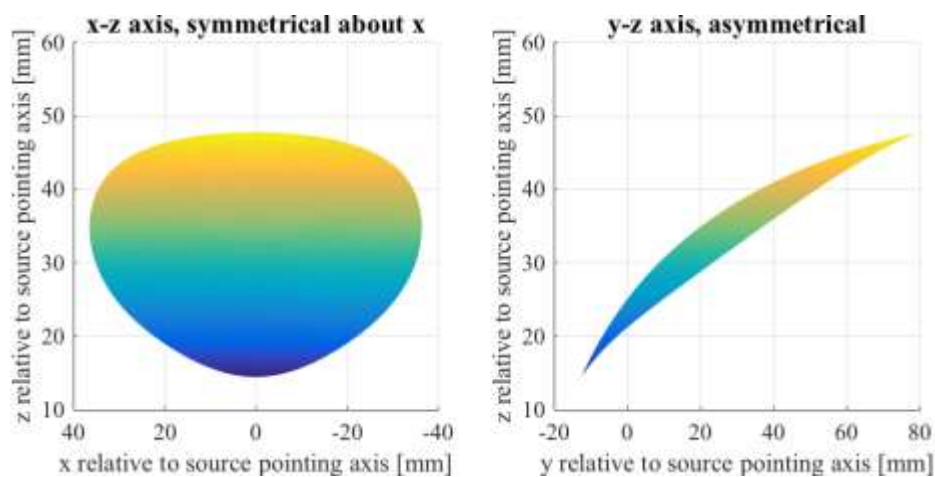


**Figure 3.5-9—Point cloud for reflective freeform with 187.5° y-tilt and 100° cone**

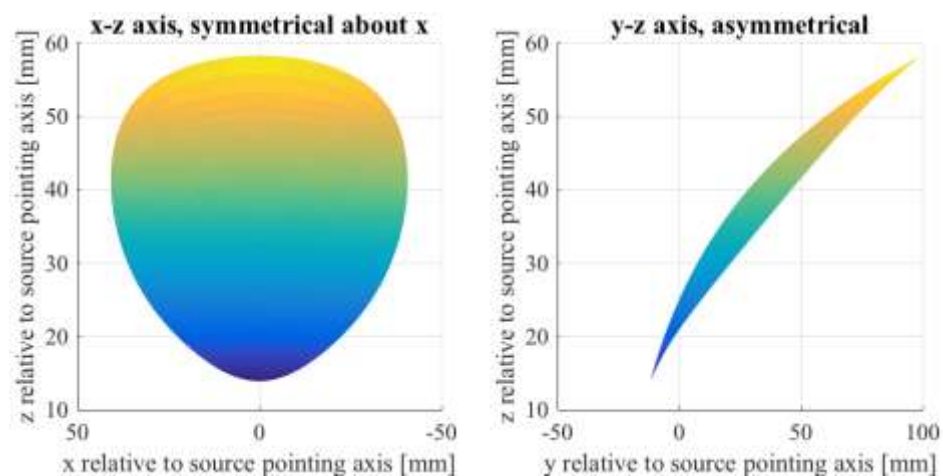


**Figure 3.5-10—Point cloud for reflective freeform with 195° y-tilt and 100° cone**

### 3.5.3. A Reflective Illumination System Optimized with a Forward-Oriented Isotropic Source

The computation for the best illumination efficiency (see Appendix, 5.4.1) finds that the freeform with a  $42.5^\circ$  pointing angle and  $120^\circ$  emission cone is the most efficient. See the target plane distribution in Figure 3.5-11. However, LightTools could not compute this freeform for all point angles due to its large emission cone, so the following analysis discusses a freeform designed for a  $90^\circ$  emission cone.

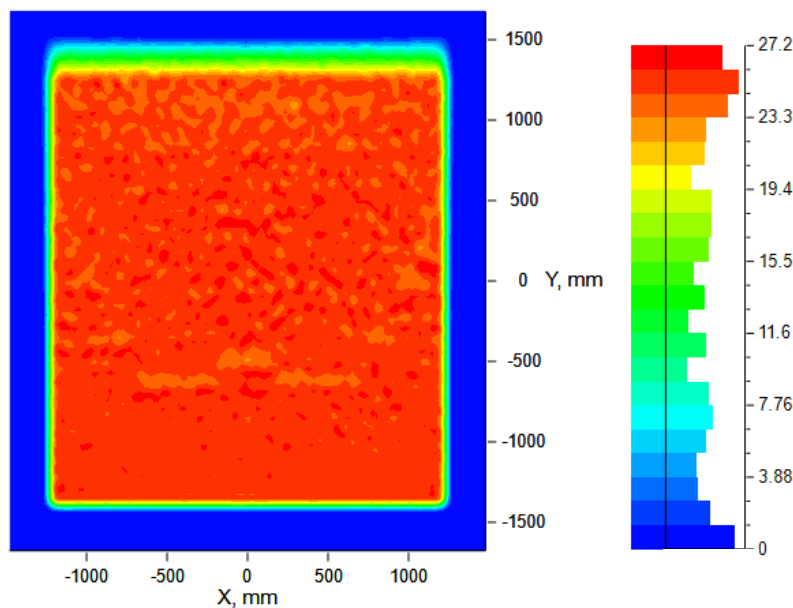
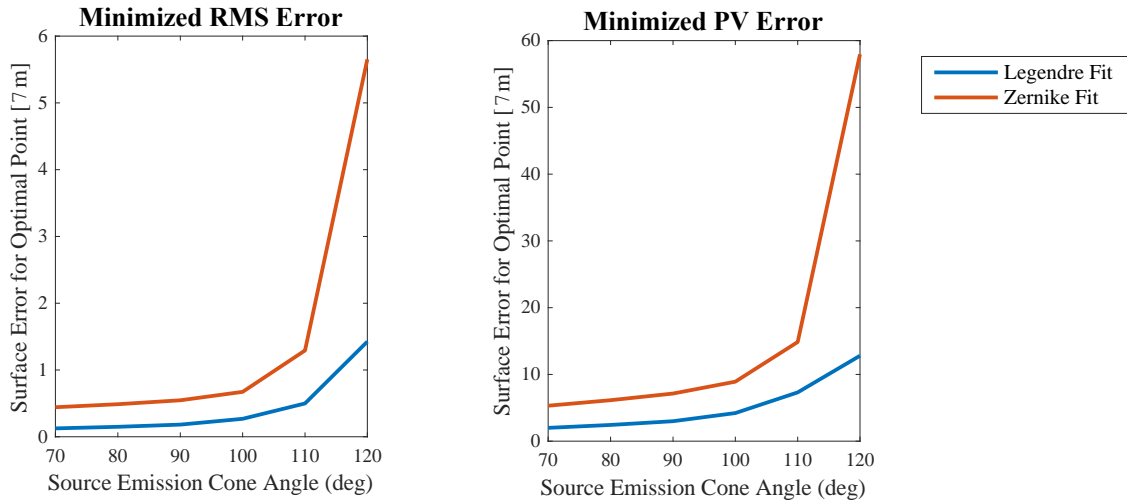


**Figure 3.5-11—Target illuminance map for a reflective illumination freeform optic with a  $42.5^\circ$  Y-tilted source and a  $120^\circ$  emission cone angle**

#### 3.5.3.1. Functional Fitting Results

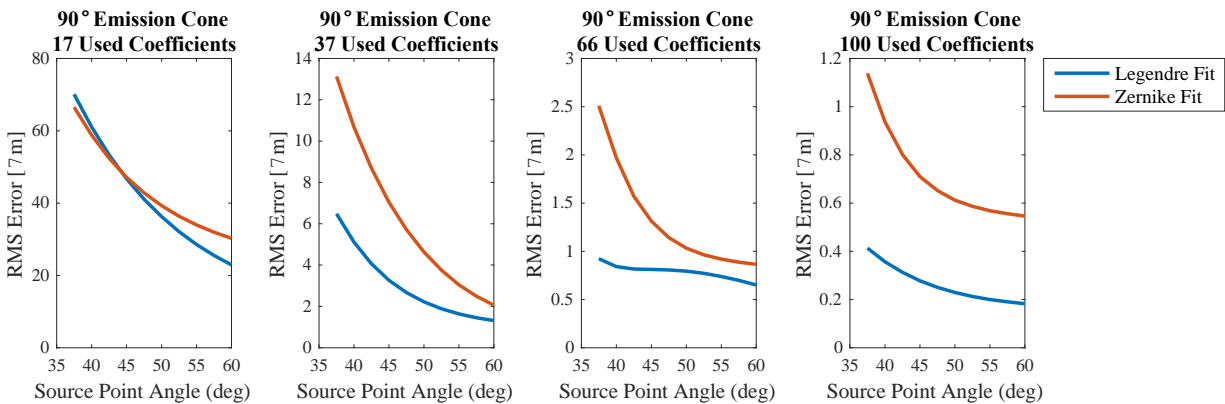
Refer to the Appendix, Section 5.4.2 to see the RMS and PV error trends as a function of the 100 coefficients used.

Figure 3.5-12 demonstrates the RMS and PV error convergence as a function of the emission cone angle. As the other freeform types demonstrated, and as does this freeform type, the fits converge on a smaller RMS and PV error as the cone angle increases.



**Figure 3.5-12—Fit convergence trends as a function of source emission cone angle for the forward-oriented reflective illumination freeform optics**

Figure 3.5-13 and Figure 3.5-14 demonstrate the ability for fits to converge on the RMS and PV error, respectively, when the source point angle is varied and the emission cone angle is fixed to 90°. The Legendre behavior, like the other freeforms, converges on a better RMS solution. For this case, the fit behavior improved when the source pointed further upward. From an illumination perspective, this is logical because it requires less surface tailoring to get the rays to reflect towards the target plane if the pointing direction is exactly 180° rotated from the nominal pointing direction.



**Figure 3.5-13—RMS error convergence trends as a function of source pointing angle for the forward-oriented reflective illumination freeform optics**

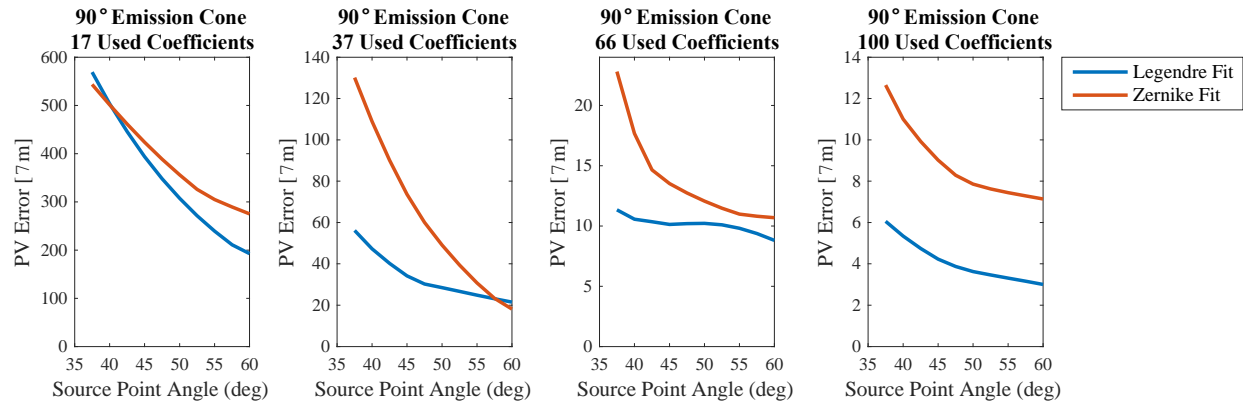


**Figure 3.5-14—PV error convergence trends as a function of source pointing angle for the forward-oriented reflective illumination freeform optics**

Finally, Figure 3.5-15, Figure 3.5-16, and Figure 3.5-17 display the freeform surfaces in order of increasing pointing angle. The point clouds look very similar, but change in their z-height, which follows the idea that the surface requires more tailoring when the pointing angle is far away from the nominal pointing direction.

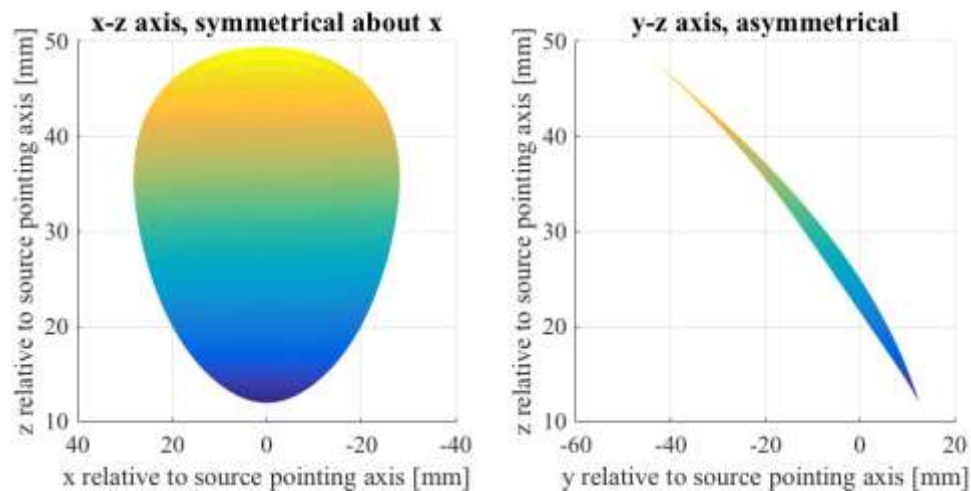


**Figure 3.5-15—Point cloud for reflective freeform with 37.5° y-tilt and 90° cone**

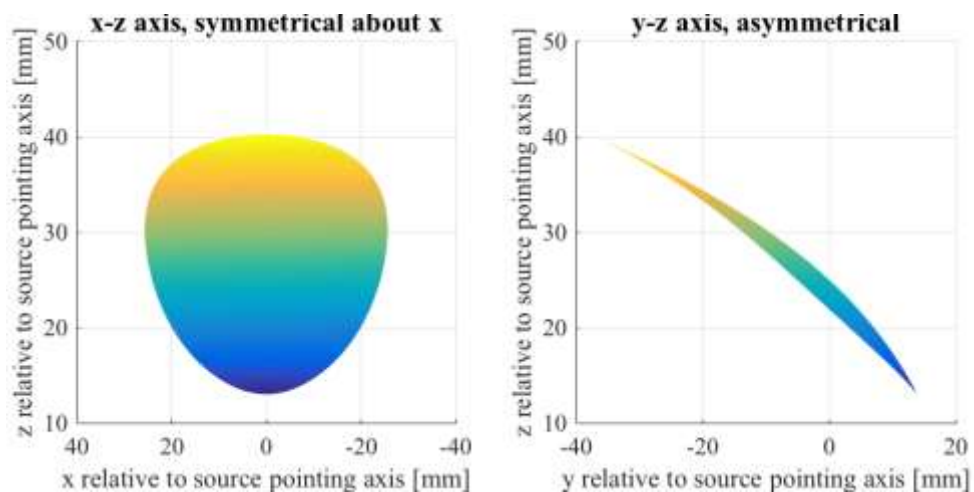


**Figure 3.5-16—Point cloud for reflective freeform with 50° y-tilt and 90° cone**

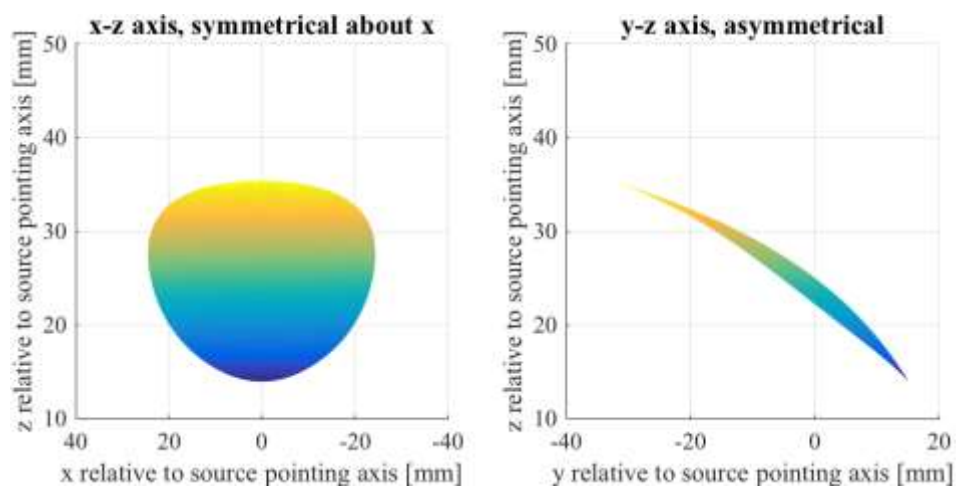


**Figure 3.5-17—Point cloud for reflective freeform with 60° y-tilt and 90° cone**

## 3.6. Conclusions

To assess the convergence ability for each illumination scenario, Figure 3.6-1 demonstrates the number of terms it takes to converge on an RMS error of 5  $\mu\text{m}$ , while Figure 3.6-2 demonstrates the same trend for an RMS error convergence of 1  $\mu\text{m}$ . As it turns out, there are not many terms required to converge on a 5  $\mu\text{m}$  RMS error.

For the refractive freeform, there are several design options in which fewer Zernike terms are required for 5  $\mu\text{m}$  RMS convergence as opposed to the Legendre fit, which centralized around the nominal point direction for the source.

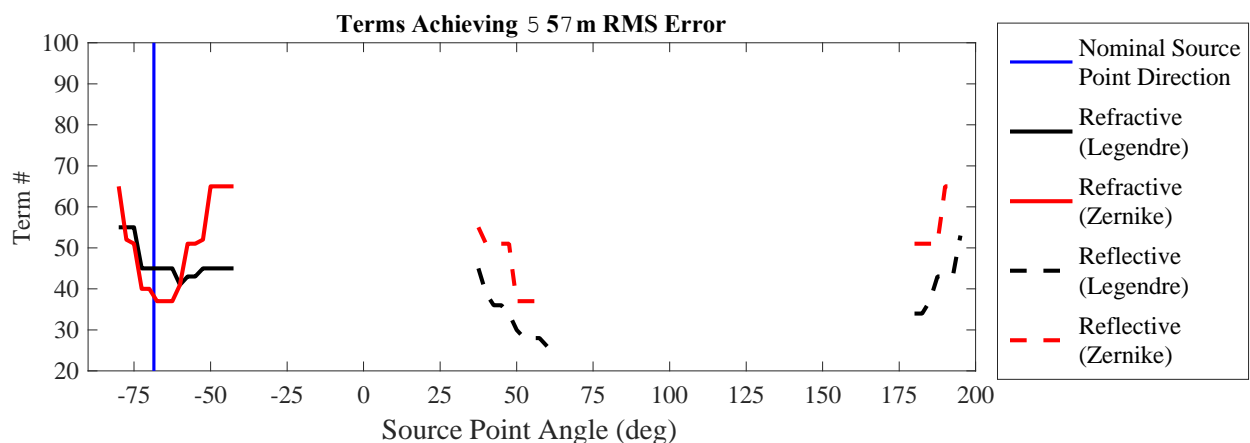


**Figure 3.6-1—Number of terms required to converge on sub-5  $\mu\text{m}$  RMS error**

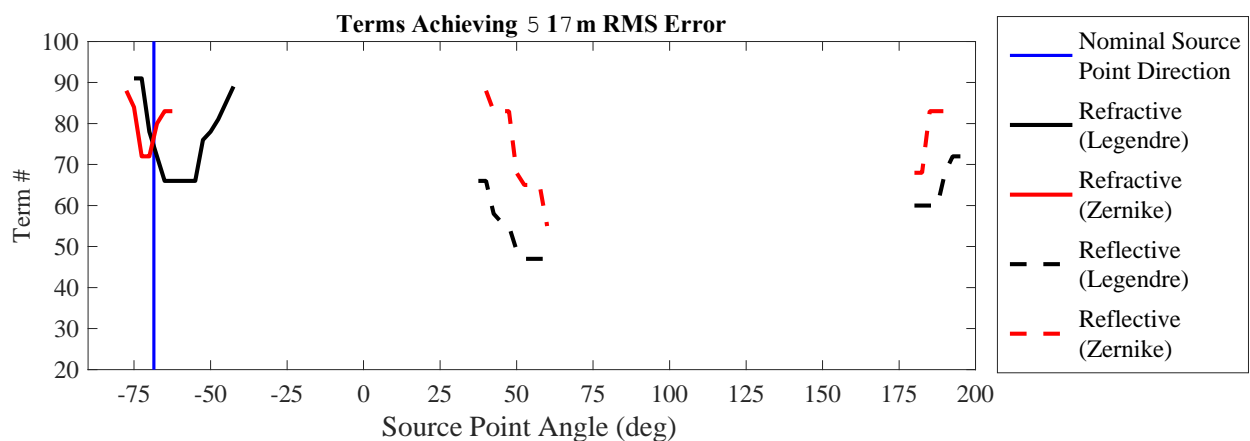


**Figure 3.6-2—Number of terms required to converge on sub-1  $\mu\text{m}$  RMS error**

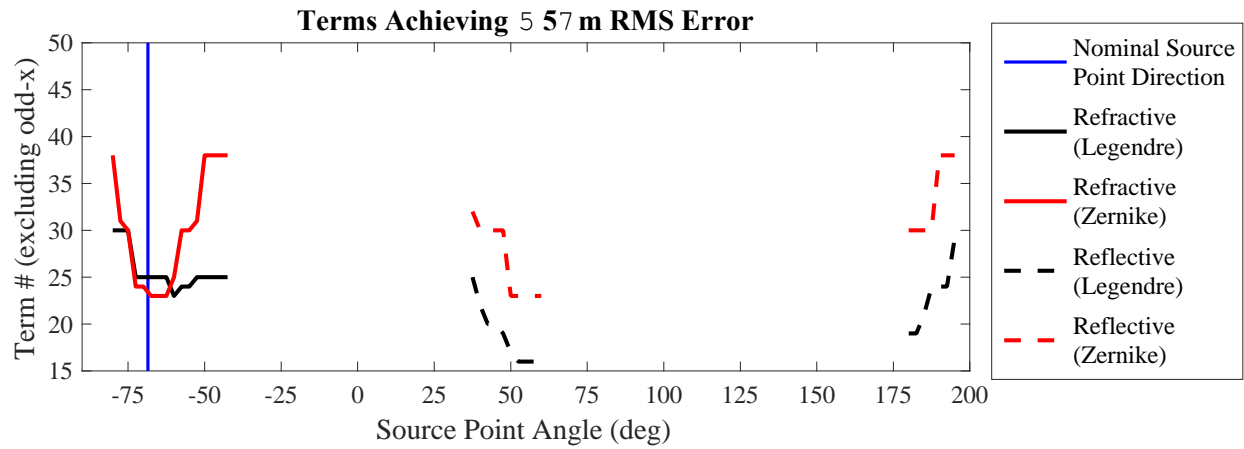


**Figure 3.6-3—Number of terms required to converge on sub-5 $\mu$ m RMS error for the illumination freeform surfaces, representing only the used coefficients (due to the removal of all odd-x coefficients)**

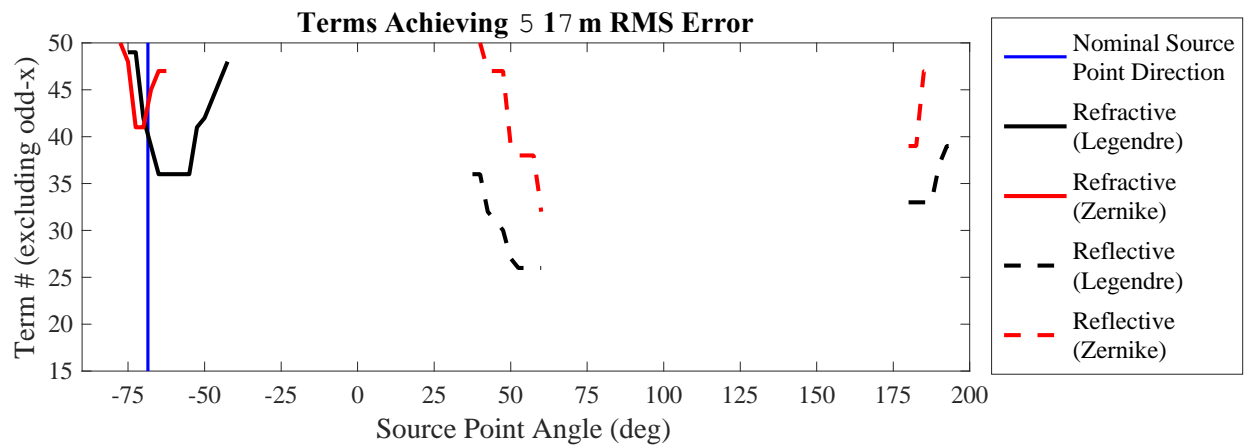


**Figure 3.6-4—Number of terms required to converge on sub-1 $\mu$ m RMS error for the illumination freeform surfaces, representing only the used coefficients (due to the removal of all odd-x coefficients)**

## 4. Summary

This analysis brings to light several new ideas: A complete definition for recursive Cartesian Zernike polynomials is introduced, and a brief definition for imaging freeformity that utilizes differences between the upper and lower marginal rays was defended.

Unfortunately, the findings of the imaging investigation were inconclusive, as the difference between the XY and Zernike polynomials were not noticeable. The next steps for this investigation should be to apply this freeform imaging system to an actual application, and add necessary lens elements to correct for the numerous off-axis aberrations occurring. Any future investigations of this freeform scenario should also exclusively involve orthogonal polynomials to ensure that the fitting function is a combination of linearly independent polynomials. Lastly, it could prove useful to remove the underlying conic surface to allow for the freeform shape to emerge on its own.

As for the illumination investigation, the results were useful. The Legendre fit was found to be more effective than the Zernike fit after 20 used coefficients. But, the Zernike fit still proves effective if the source pointing direction of the fitted freeform is close to that of the nominal source point direction (when the source points directly at the center of the painting). To improve this analysis, a fit should be done in which non-contributing terms (other than odd-x terms) are removed. Also, a surface optimization for an extended, real source should be performed to determine whether the real ray trace is more effective with a Legendre fit or with a Zernike fit.

Overall, more work is needed to argue whether Cartesian or polar coordinates more effectively fit to freeform surfaces, but the illumination results presented here begin a good discussion.

# References

- [1] Arfken, G. "Legendre Functions." Ch. 12 in *Mathematical Methods for Physicists*, 3rd ed. Orlando: Academic Press, pp. 637-711, 1985.
- [2] Chaves, Julio. *Introduction to Nonimaging Optics*. Boca Raton: CRC Press, 2015.
- [3] Fournier, Florian R., William J. Cassarly, and Jannick P. Rolland. "Fast freeform reflector generation using source-target maps." *Optics Express* 18, no. 5 (2010): 5295-5304.
- [4] Goodman, Joseph W. *Introduction to Fourier Optics*. 2nd ed. New York: McGraw-Hill, 1996.
- [5] Greivenkamp, John E. *Field Guide to Geometrical Optics*. Bellingham: SPIE, 2004.
- [6] Hecht, Eugene and A. R. Ganesan. *Optics*, 4th ed. Chennai: Pearson, 2012, 145.
- [7] Jacobsen, Jake, and William Cassarly. "Optical Design: Software tools design freeform optics for illumination." *Laser Focus World*, February 01, 2016. Accessed April 20, 2017. <http://www.laserfocusworld.com/articles/print/volume-52/issue-01/features/optical-design-software-tools-design-freeform-optics-for-illumination.html>.
- [8] Koshel, R. John. "Standard Optics Used in Illumination Engineering." Ch. 1.8 in *Illumination Engineering: Design with Nonimaging Optics*. Hoboken: John Wiley & Sons, Inc., 2013.
- [9] Lanczos, C. *Applied Analysis*. Englewood Cliffs: Prentice-Hall, 1956, 348.
- [10] Ma, Donglin, Shaun Pacheco, Chengliang Wang, and Rongguang Liang. "Freeform optics construction with nonuniformly sampled grids in modified double-pole coordinate system." *Optical Engineering* 54, no. 12 (2015): 125102.
- [11] Mahajan, Virendra. *Optical Imaging and Aberrations, Part I: Ray Geometrical Optics*. Bellingham: SPIE, 1998, 275.
- [12] Mahajan, Virendra. "Anamorphic Systems." Ch. 13 in *Optical Imaging and Aberrations, Part III: Wavefront Analysis*. Bellingham: SPIE, 2013, 356-360.
- [13] Miñano, Juan C., Pablo Benitez, and Asunción Santamaría. "Free-form optics for illumination." *Optical Review* 16, no. 2 (2009): 99-102.
- [14] Nikiforov, Arnold F., Vasili B. Uvarov, and Sergei K. Suslov. Ch. 1 in *Classical Orthogonal Polynomials of a Discrete Variable*. New York: Springer-Verlag, 1992, 7.
- [15] Nikolic, Milena, Pablo Benítez, Bharathwaj Narasimhan, Dejan Grabovickic, Jayao Liu, and Juan C. Miñano. "Optical design through optimization for rectangular apertures using freeform orthogonal polynomials: a case study." *Optical Engineering* 55, no. 7 (2016): 071204.
- [16] Ong, P., J. Gordon, and A. Rabl, "Tailored edge-ray designs for illumination with tubular sources," *Applied Optics* 35, no. 22 (1996): 4361-4371.

- [17] Synopsys, Inc. "Automatic Design (Optimization Menu)." In CODE V 11.0 Reference Manual, 2017.
- [18] Synopsys, Inc. "Creating Freeform Designer Features." Ch. 2 in LightTools 8.4 Advanced Design Module User's Guide, 2016.
- [19] The Editors of Encyclopædia Britannica. "Polar coordinates." Encyclopædia Britannica. July 20, 1998. Accessed April 09, 2017. <https://www.britannica.com/topic/polar-coordinates>.
- [20] Ulanich, Rachel, Kaitlyn Williams, Page King, Ross D. Uthoff, Liliana Ruiz, and R. John Koschel. "Designing a freeform optic for oblique illumination." In process for the International Optical Design Conference (2017).
- [21] [Weisstein, Eric W.](http://mathworld.wolfram.com/Multiple-AngleFormulas.html) "Multiple-Angle Formulas." From [MathWorld](http://mathworld.wolfram.com)--A Wolfram Web Resource. <http://mathworld.wolfram.com/Multiple-AngleFormulas.html>.
- [22] Williams, Kaitlyn E., Rachel N. Ulanich, Page King, Ross D. Uthoff, Liliana Ruiz Diaz, Jessica Steidle, and R. John Koschel. "Functional fitting of freeform optics." In process for The International Optical Design Conference (2017).
- [23] Winston, R., J.C. Miñano, and P. Benítez. "Concentrators for Prescribed Irradiance." Ch. 7 in *Nonimaging Optics*. Burlington: Elsevier Academic Press, 2005.
- [24] Winston, R., J.C. Miñano, and P. Benítez. "The Edge-Ray Principle or 'String' Method." Ch. 4.4 in *Nonimaging Optics*. Burlington: Elsevier Academic Press, 2005.
- [25] Wyant, James C., and Katherine Creath. "Basic Wavefront Aberration Theory for Optical Metrology." Ch. 1 in *Applied Optics and Optical Engineering, Vol. XI*, Edited by Robert R. Shannon and James C. Wyant. New York: Academic Press, 1992, 30.
- [26] Zernike, von Frits. "Beugungstheorie des Schneidensverfahrens und Seiner Verbesserten Form, der Phasenkontrastmethode". *Physica* 1, no. 8 (1934): 689–704.
- [27] Zhu, Ruidong, Qi Hong, Hongxia Zhang, and Shin-Tson Wu. "Freeform reflectors for architectural lighting." *Optics Express* 23, no. 25 (2015): 31828-31837.

## 5. Appendix

### 5.1. Refractive Imaging

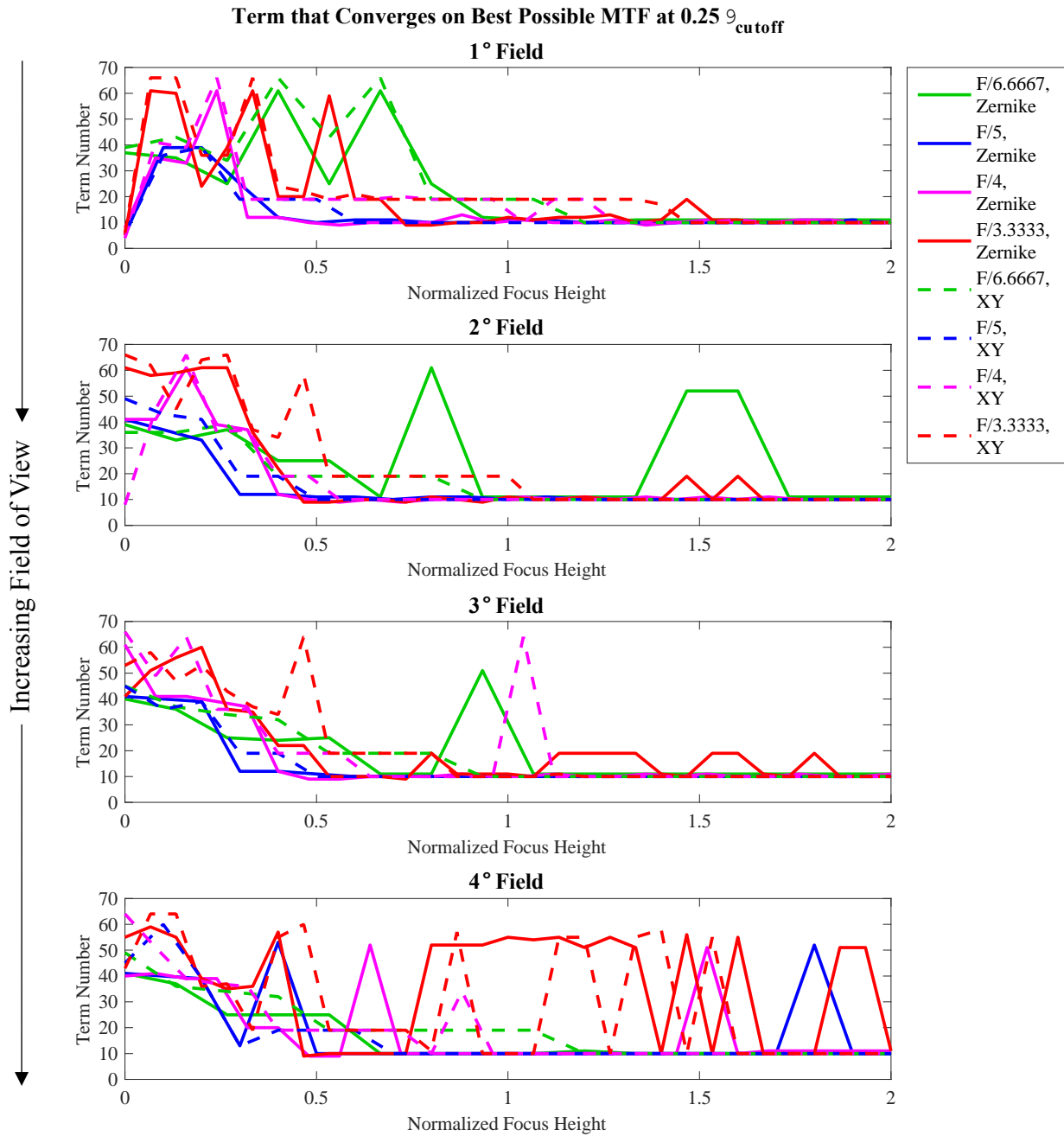


**Figure 5.1-1—Term that converges on maximum MTF for 0.25 of the spatial cutoff frequency as a function of normalized focus height, for the system with a field of view and arranged vertically by increasing FOV**

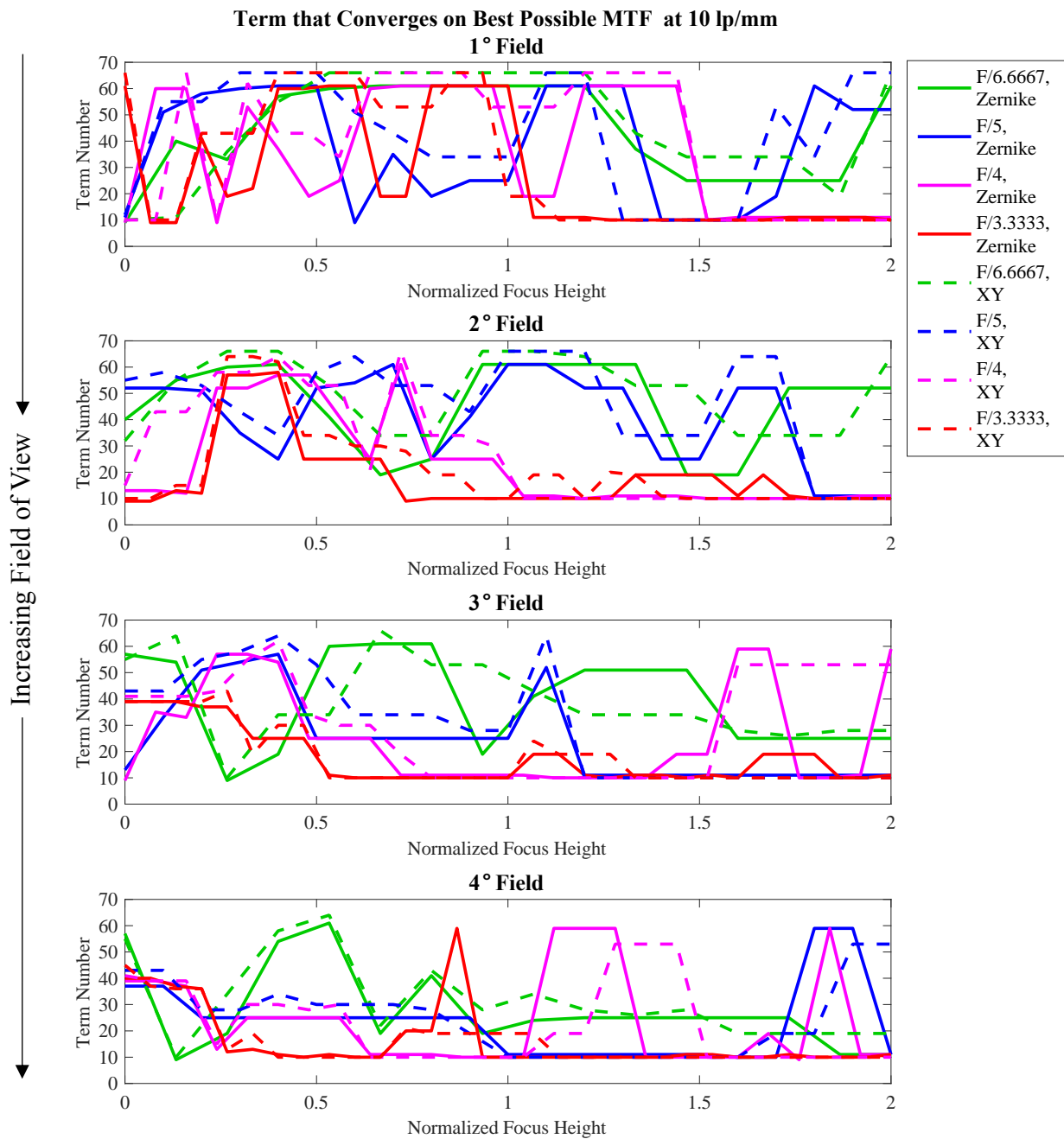


**Figure 5.1-2— Term that converges on maximum MTF amplitude at 10 line pairs per mm, for the system with a field of view and arranged vertically by increasing FOV**

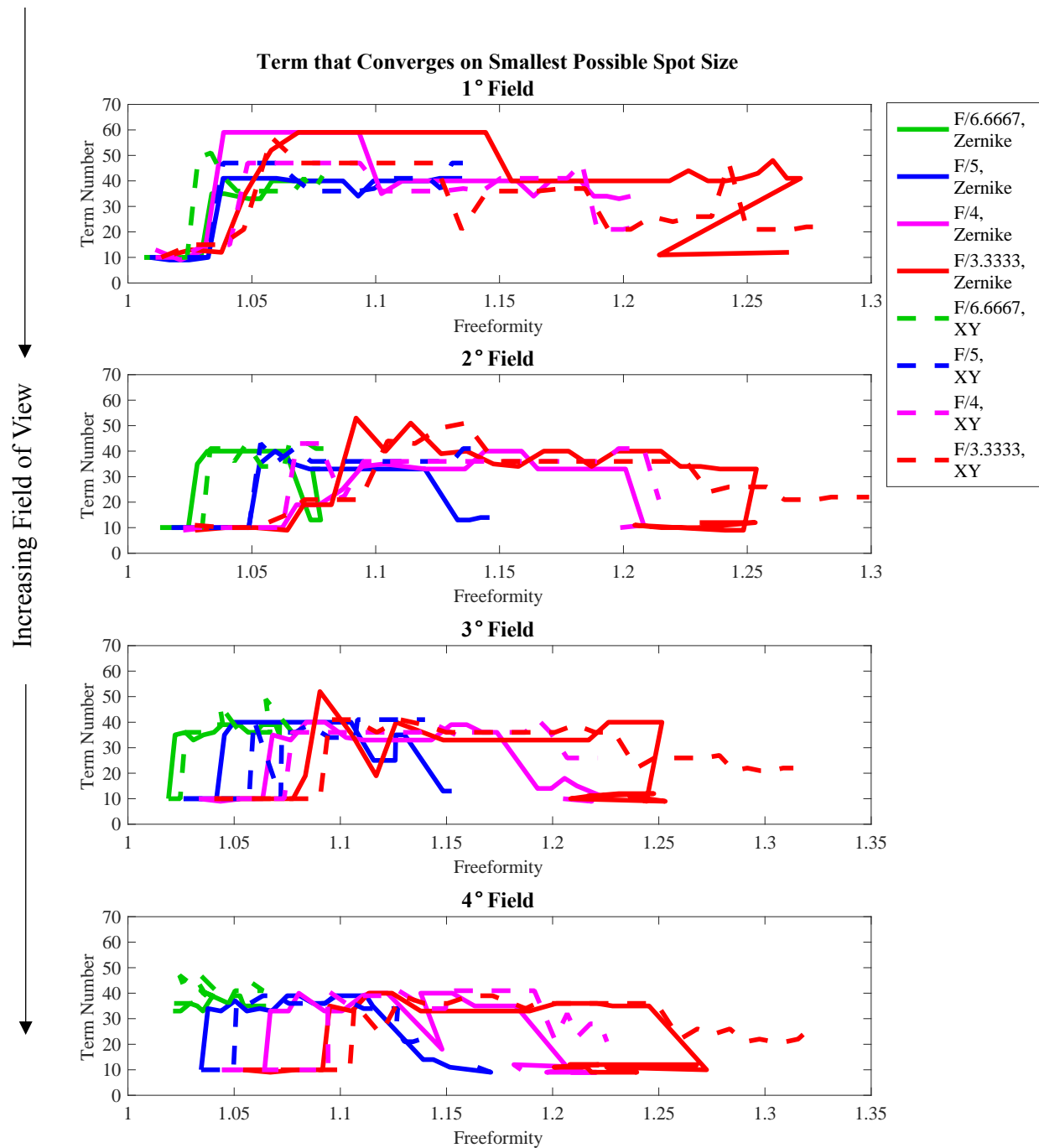


**Figure 5.1-3— Term that converges on minimum image size as a function of freeformity, for the system with a field of view and arranged vertically by increasing FOV**

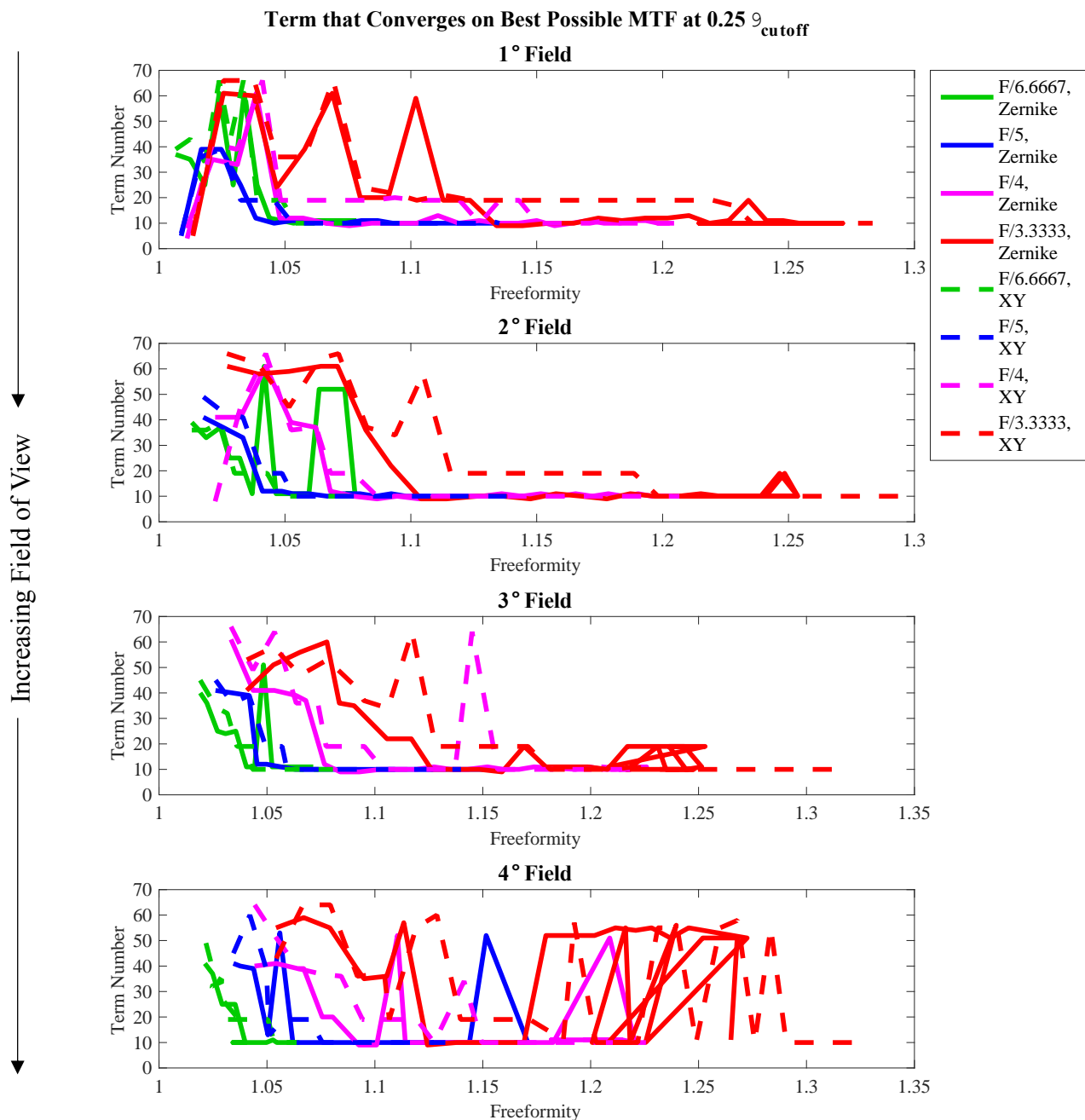


**Figure 5.1-4—Term that converges on maximum MTF amplitude for 0.25 of the spatial cutoff frequency as a function of freeformity, for the system with a field of view and arranged vertically by increasing FOV**

When the freeformity increased, the best convergence only required up to the 10th term, as seen in the above Figure 5.1-4.

## 5.2. Refractive Illumination

### 5.2.1.1. Ray-Trace Results

Figure 5.2-1 demonstrates that illumination characteristics on the target map for the refractive illumination results.

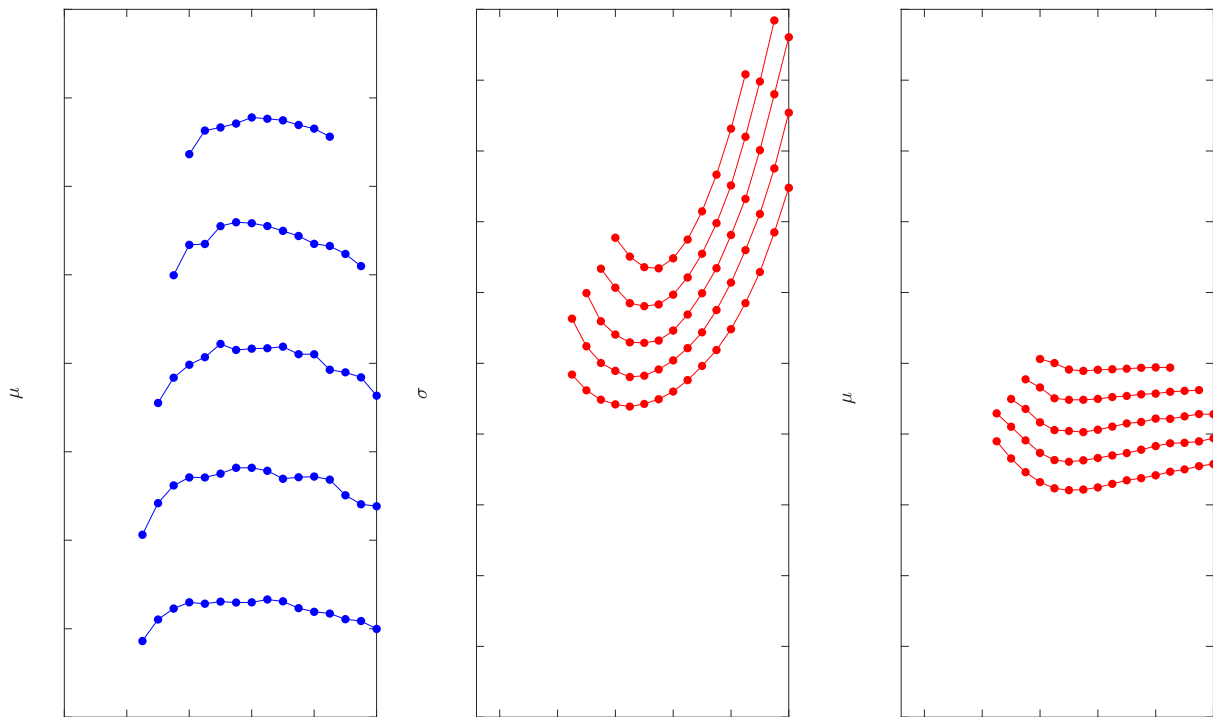


**Figure 5.2-1—Illumination characteristics for the refractive freeform optics**

The average target illuminance is defined by the average of the illuminance contained within the dimensions defined by the Rothko target. The standard deviation is calculated with the same.

The target exterior is defined by the target distribution that resides outside of the dimensional confines of the Rothko painting.

Equation (5-1) defines a metric, the effective illuminance, that defines how effective the distribution on the target is for the source pointing angle. It encompasses the average illuminance, standard deviation, and the amount of light incident on the outside of the painting.

$$E_{eff} = \mu_T - \sigma_T - \mu_{ext} \quad (5-1)$$

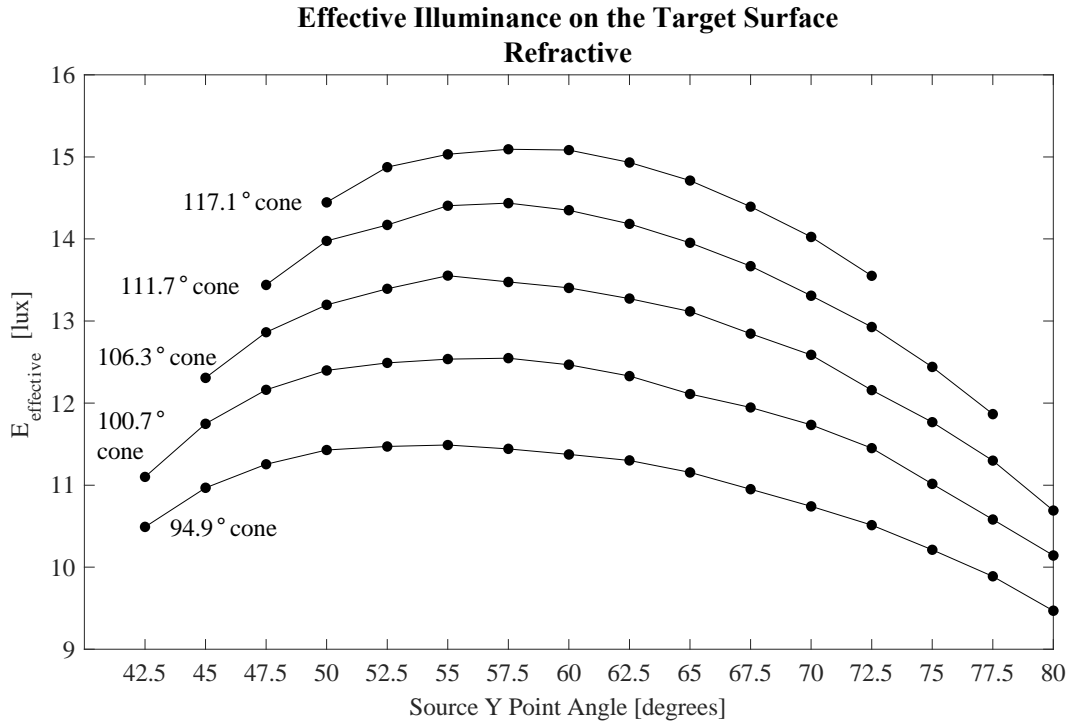


**Figure 5.2-2—Effective illumination levels of the target for the refractive freeform optics**

Now, this does not take into account that the 94.9° cone may be more effective at distributing light because it has a smaller average illuminance due to it distributing less light. Therefore, Equation (5-2) is used in its place to single out the illumination efficiency of each freeform. See the results using this equation in Figure 5.2-3.

$$\eta_E = \frac{E_{eff}}{E_{T,max}} = \frac{\mu_T - \sigma_T - \mu_{ext}}{E_{T,max}} \quad (5-2)$$

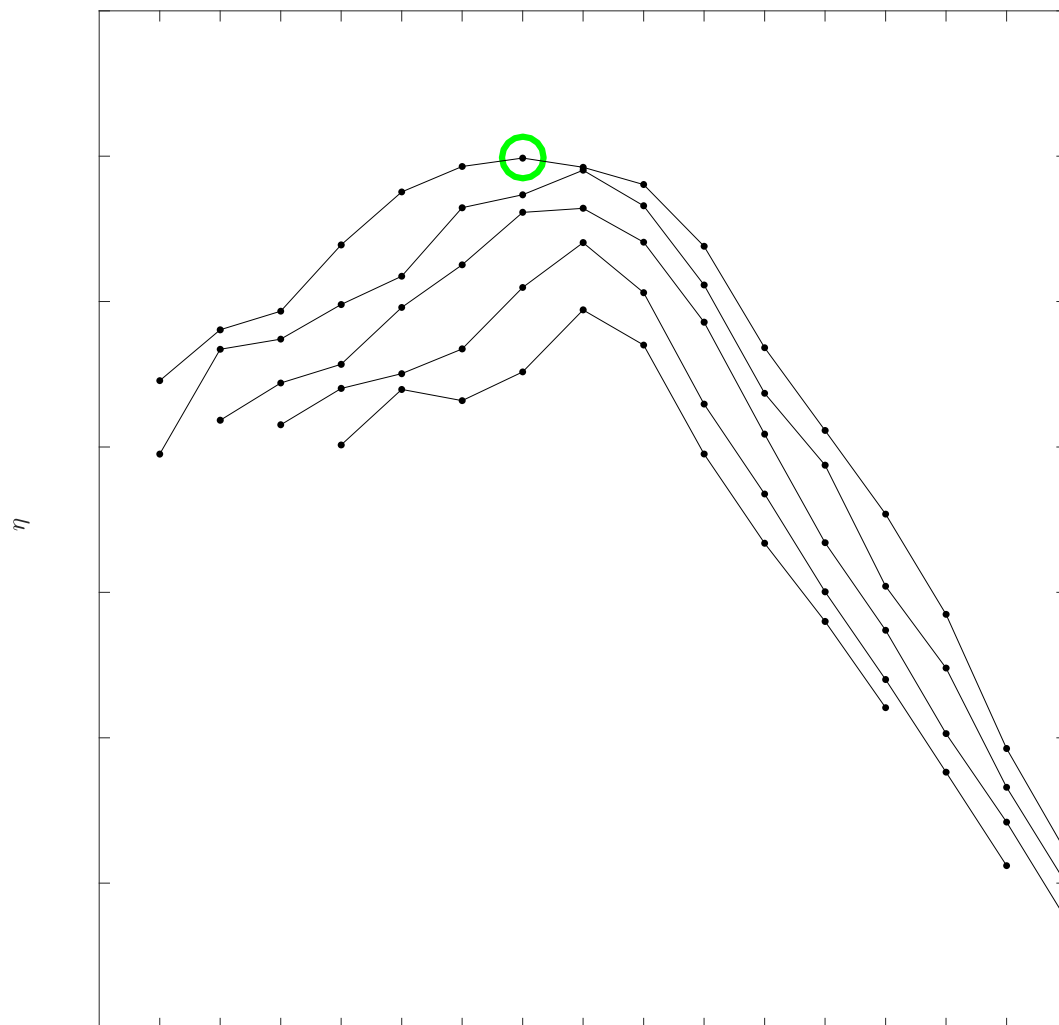


**Figure 5.2-3—Normalized illumination efficiency for the refractive freeform optics**

## 5.3. Reflective Illumination, Reverse-Oriented Source

### 5.3.1. Ray-Trace Results

Following the same discussion as Section 5.2.1.1, the following figures represent the illumination efficiency of this design scenario.

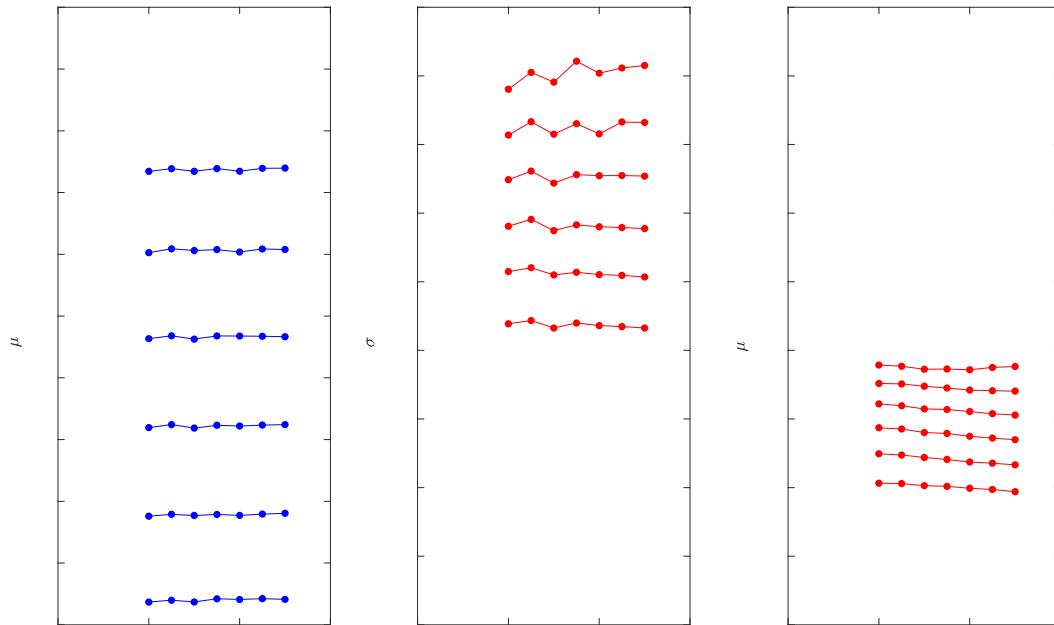


Figure 5.3-1—Illumination characteristics, reflective freeform, reverse-oriented source

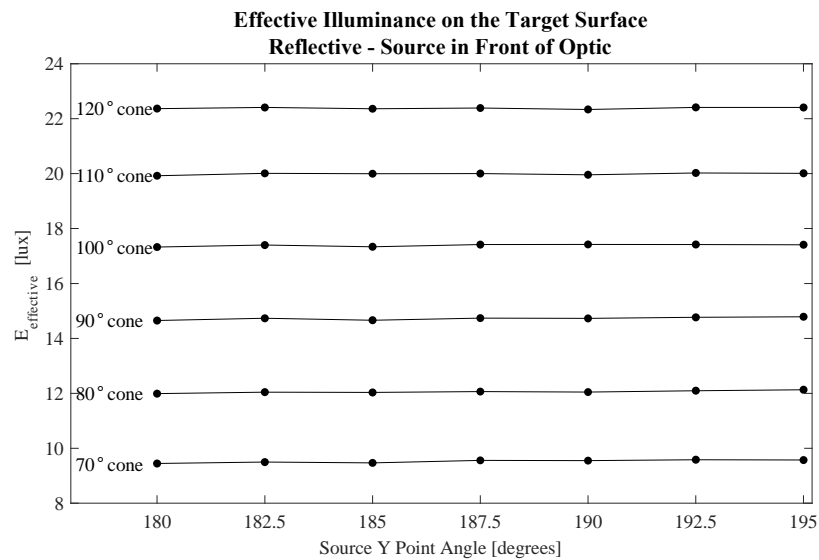
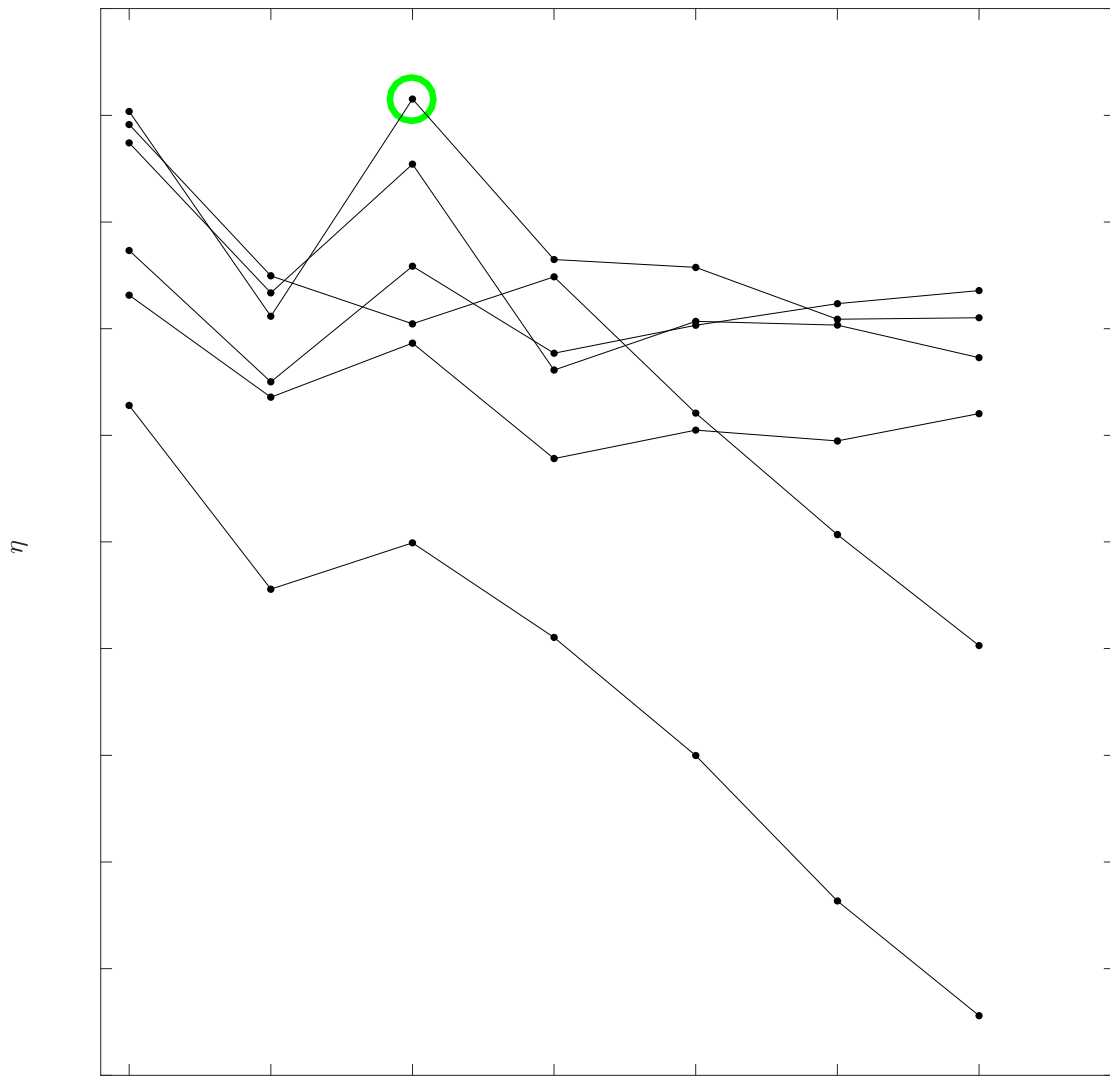
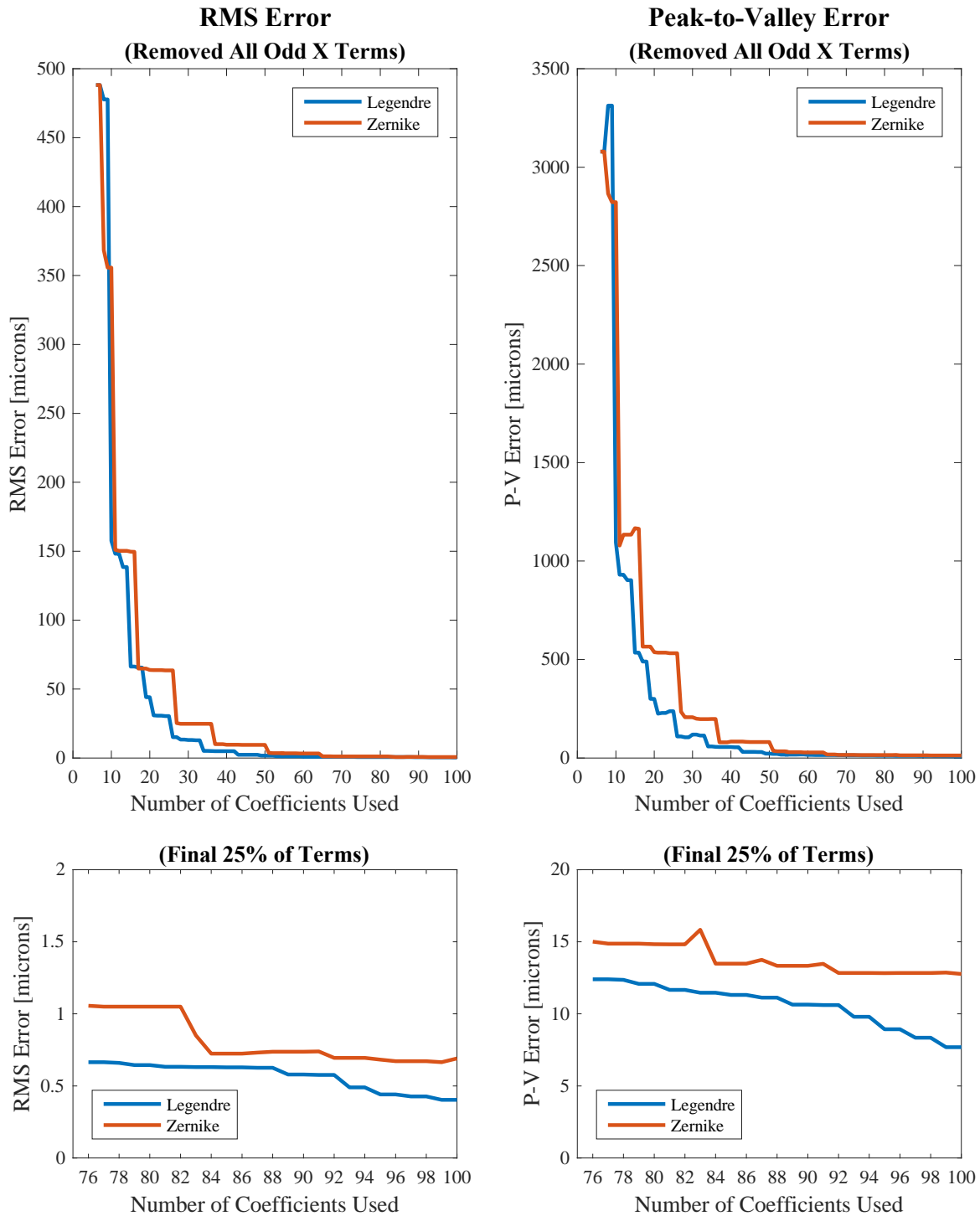


Figure 5.3-2—Effective target illuminance, reflective freeform, reverse-oriented source



**Figure 5.3-3—Normalized illumination efficiency for the reflective freeform with the reverse-oriented source**

### 5.3.2. Functional Fitting Results



**Figure 5.3-4—Fit behavior of the 185° (reverse-oriented) source Y-tilt, 100° emission cone**

## 5.4. Reflective Illumination, Forward-Oriented Source

### 5.4.1. Ray-Trace Results

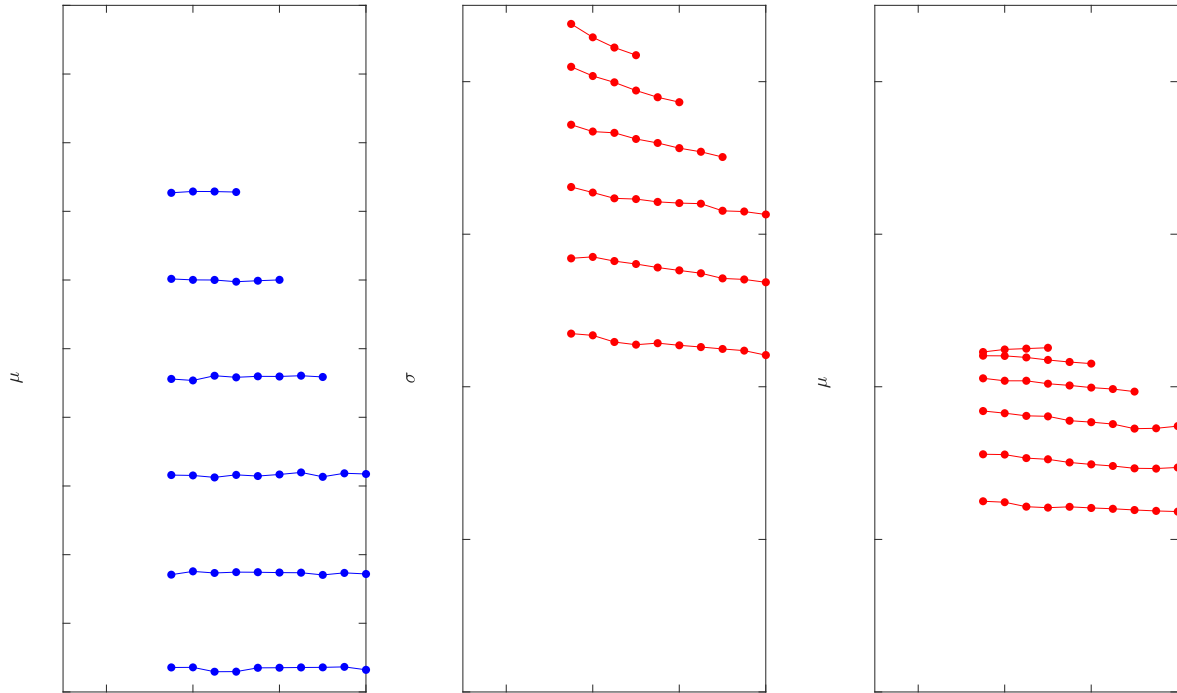


Figure 5.4-1—Illumination characteristics, reflective freeform, forward-oriented source

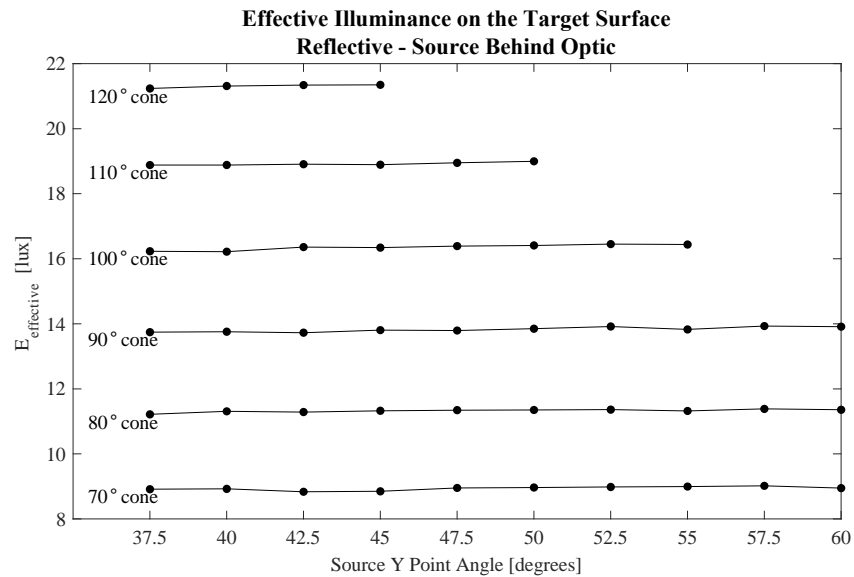
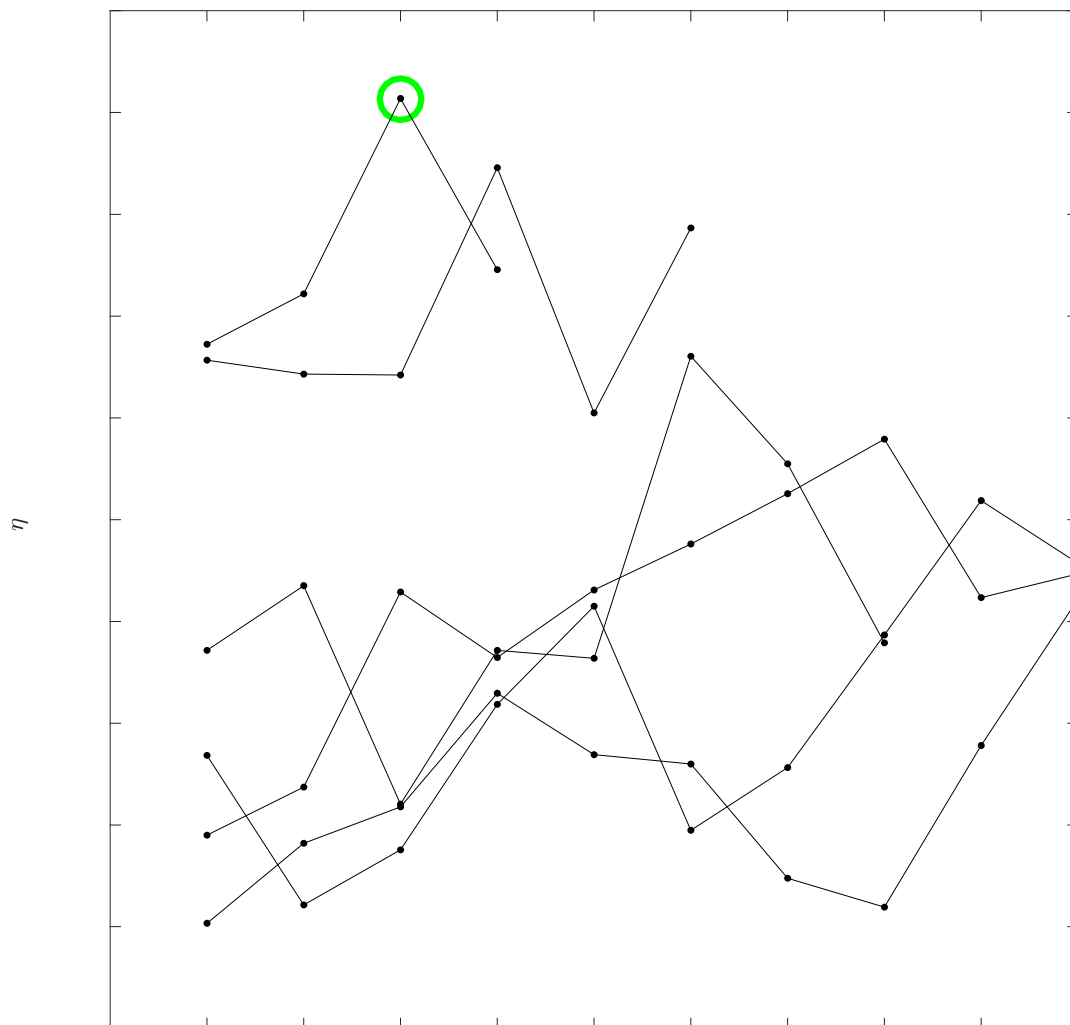


Figure 5.4-2—Effective target illuminance, reflective freeform, forward-oriented source



**Figure 5.4-3—Normalized illumination efficiency for the reflective freeform with the forward-oriented source**

## 5.4.2. Functional Fitting Results

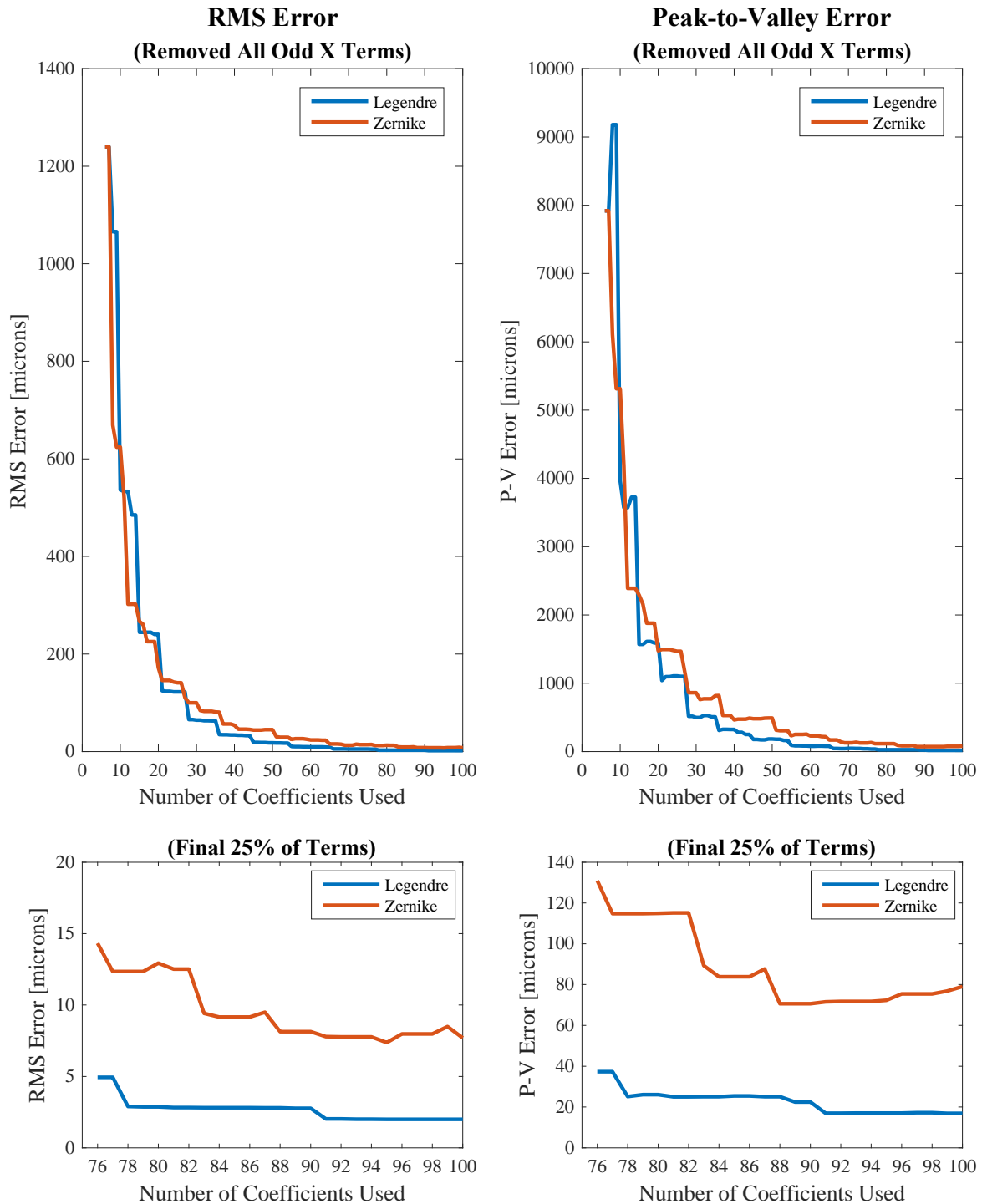
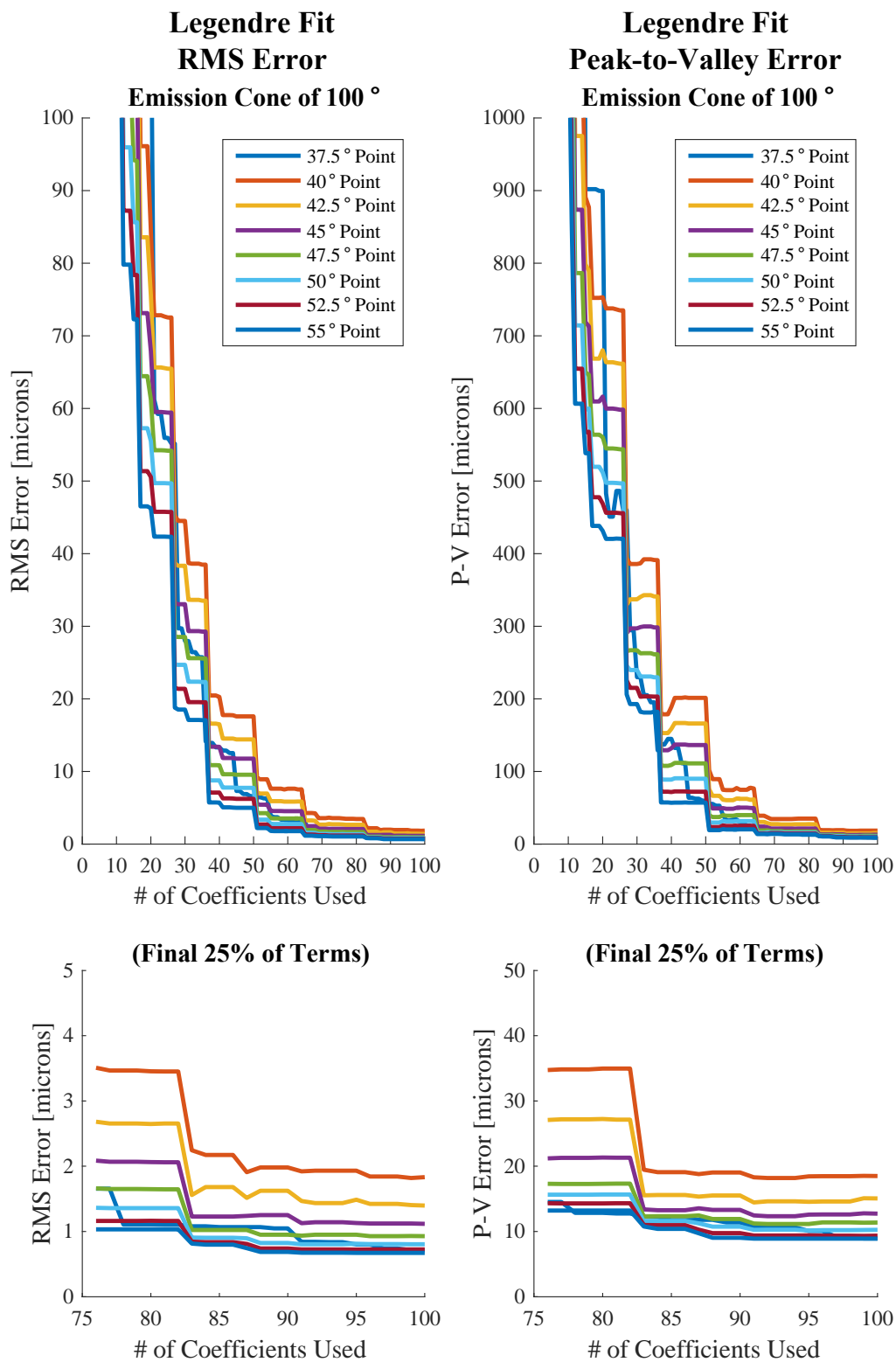
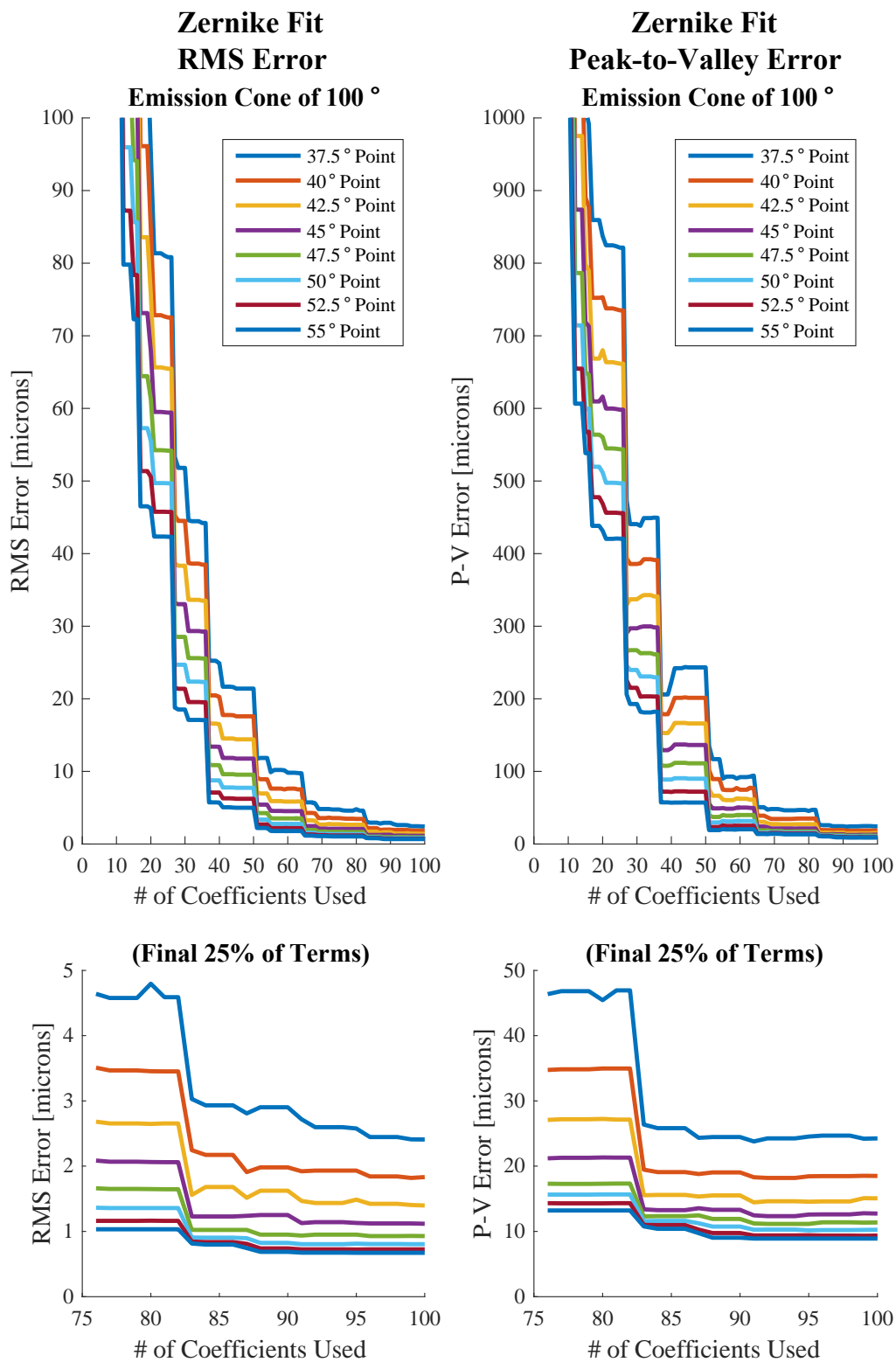


Figure 5.4-4—Fit behavior of the 42.5° (forward-oriented) source Y-tilt, 120° emission cone



**Figure 5.4-5—Legendre fit trends for varying point angle**



**Figure 5.4-6—Zernike fit trends for varying point angle**